CIRCUMFERENTIAL STRESS ANALYSIS IN STEAM HEADER

by

Sam Jotham Sutharson

A thesis submitted to the faculty of
The University of North Carolina at Charlotte
in partial fulfillment of the requirements
for the degree of Master of Science in
Mechanical Engineering

Charlotte

2019

Approved by:

_____
Dr. Alireza Tabarraei

_____
Dr. Qiuming Wei

_____
Dr. Russell Keanini

ABSTRACT

SAM JOTHAM SUTHARSON. Circumferential stress analysis in steam header
(Under the direction of DR. ALIREZA TABARRAEI)

Thick walled cylindrical steam headers are subject to varying amounts of circumferential stresses in their normal operating cycles... Analyzing the variations in the amount and the location of hoop stresses on different samples with varying material parameters would be an expensive option if done experimentally, but a computational analysis results yields a more economical analysis of the problem presented, provided the boundary conditions prescribed immaculately replicate the operational conditions of the header computationally.

This thesis deals with the computational finite element simulation of steam header sections with varying physical parameters and their effect on the circumferential stresses developed within the header when simulated with a nominal operating cycle using ABAQUS. The material chosen for the header is grade 91 steel and its physical properties were used for the simulation. Thirty steam header models of varying side tube penetration angles and varying cylinder wall thickness were used for the simulation to bring about a relationship between these variations and the circumferential stresses developed within the header. An additional three models were simulated to confirm the validity of the results.

A careful observation from the results led to the identification of the primary physical factors that had the most significant effect on the circumferential stresses developed and this method is prescribed for similar design problems.

ACKNOWLEDGEMENTS

I would like to thank my advisor Dr. Alireza Tabarraei, for his guidance and motivation, without which this thesis would not have materialized.

I would also like to thank my committee members Dr. Qiuming Wei and Dr. Russell Keanini for spending their valuable time to evaluate and asses my work.

DEDICATION

I dedicate this work to my parents, Mr. Sutharson and Dr. Sheela Mallika Rani and also my sister, Sharon and my brother in law Anand. None of this would have materialized without their unconditional love and support.

TABLE OF CONTENTS

LIST OF TABLES vii

LIST OF FIGURES viii

CHAPTER 1: Introduction 1

CHAPTER 2: Modelling 4

2.1 Nomenclature 8

CHAPTER 3: Setting up the simulation 10

3.1 Material Properties and Operating Cycle 10

3.2 Set Creation and Boundary Conditions 14

3.3 Partitioning 19

3.4 Meshing 20

3.5 Mesh Verification 21

3.6 Element Type 21

3.7 Step 23

CHAPTER 4: Verification 25

4.1 Axial Stress 25

4.2 Circumferential Stress 26

4.3 Radial Stress 26

4.4 Verification 26

CHAPTER 5: Theory 30

5.1 ABAQUS 30

5.1.1 Exact Implementation 30

5.1.2 Approximate Implementation 31

5.1.3 Steady State 32

5.1.4 Transient Analysis 32

5.1.5 Spurious Oscillations 32

5.2 Temperature effect and stress 33

5.2.1 Stress concentration factor 36

5.2.2 Coefficient of thermal expansion 36

5.2.3 Side tube angle 37

5.2.4 Temperature difference 37

5.2.5 Modulus of elasticity 38

CHAPTER 6: Results 40

6.1 Prediction of results 69

CHAPTER 7: Inference and Conclusion 87

REFERENCES 89

APPENDIX: PYHTON SCRIPT USED FOR SIMULATION 91

LIST OF TABLES

TABLE 1.1:	Chemical composition of grade 91 steel - SA335-P91 (%)	1
TABLE 3.1:	Material Properties of grade 91 steel	10
TABLE 3.2:	Operating cycle used for the simulation	11
TABLE 6.1:	Stress and temperature difference for m model 10-6-θ	62
TABLE 6.2:	Stress and temperature difference for m model 9-5-θ	62
TABLE 6.3:	Stress and temperature difference for m model 10-8-θ	62
TABLE 6.4:	Stress and temperature difference for m model 9-7-θ	63
TABLE 6.5:	Stress and temperature difference for m model 8-6-θ	63
TABLE 6.6:	Stress and temperature difference for m model 10-7-θ	63
TABLE 6.7:	P91 Yield strength at elevated temperatures.	86

LIST OF FIGURES

FIGURE 1.1: Hoop stress failure 3

FIGURE 2.1: The complete section of the header 4

FIGURE 2.2: The cutaway section of the header 5

FIGURE 2.3: Radial dimensions of the model 6

FIGURE 2.4: Angular dimensions of the side tube 6

FIGURE 2.5: Length of the header segment 7

FIGURE 2.6: General specifications of the model 7

FIGURE 2.7: Models with varying side tube angles. (a) side tube angle 20 degrees, (b) side tube angle 22.5 degrees, (c) side tube angle 25 degrees. 9

FIGURE 2.8: Models with varying side tube angles. (a) side tube angle 27.5 degrees, (b) side tube angle 30 degrees. 9

FIGURE 3.1: Operating cycle vs time period 12

FIGURE 3.2: Set creation for symmetry along Z-axis boundary condition 13

FIGURE 3.3: Set creation for symmetry along X-axis boundary 13

FIGURE 3.4: Set creation for symmetry of side tube along local Y-axis boundary condition 15

FIGURE 3.5: Constraint nodes set creation for constraint by equation boundary condition 15

FIGURE 3.6: Reference node set creation for constraint by equation boundary condition 16

FIGURE 3.7: Set creation for predefined field to apply the ambient room temperature 16

FIGURE 3.8: End load set creation for end load application 17

FIGURE 3.9: Surface load set creation for internal pressure and thermal load 17

FIGURE 3.10: Final model with all loads and constraints 18

FIGURE 3.11: Partitioning of the material for a denser mesh 19

FIGURE 3.12: Fine and coarse meshes due to partitioning 20

FIGURE 3.13: 20 node element 22

FIGURE 4.1: Verification stresses from the simulation 27

FIGURE 4.2: Maximum axial stress from simulation 27

FIGURE 4.3: Maximum circumferential stress from the simulation 28

FIGURE 4.4: Maximum radial stress from the equation 28

FIGURE 4.5: Location of the node chosen for verification 29

FIGURE 5.1: Wire segment 33

FIGURE 5.2: Wire segment bound on both sides 34

FIGURE 5.3: Setup to measure temperature effect of stress 34

FIGURE 5.4: Location of nodes 39

FIGURE 6.1: Prescribed cylindrical co-ordinate system 40

FIGURE 6.2: Location of the node exhibiting maximum hoop stress 41

FIGURE 6.3: Stress (MPa) vs Time (seconds) for θ = 20 for all models 42

FIGURE 6.4: Temperature difference (°C) vs Time (seconds) for θ = 20 for all models 43

FIGURE 6.5: Stress (MPa) / Temperature Difference (°C) vs Time (seconds) for θ = 20, E.D = 10 inches, ID = 6 inches 44

FIGURE 6.6: Stress (MPa) / Temperature Difference (°C) vs Time (seconds) for θ = 20, E.D = 10 inches, ID = 8 inches 45

FIGURE 6.7: Circumferential stress directions of model 10-6-20 at increment number 105, when the temperature difference is close to minimum. 46

FIGURE 6.8: Circumferential stress directions in a cut of the model 10-6-20 at increment number 47, the frame of maximum tension. 47

FIGURE 6.9: Circumferential stress directions in a cut of the model 10_8_20 at increment number 100, the increment at which maximum hoop stress occurs in this model.9 47

FIGURE 6.10: Stress (MPa) vs Time (seconds) for all models with θ = 20 for the time 0 to 4000 seconds. 48

FIGURE 6.11: Stress (MPa) vs Time (seconds) for all models with θ = 20 for the time 4000 to 10000 seconds. 49

FIGURE 6.12: Stress (MPa) vs Time (seconds) for all models with θ = 20 for the time 10000 to 30000 seconds. 50

FIGURE 6.13: Stress (MPa) vs Time (seconds) for all models with θ = 22.5 for the time 0 to 30000 seconds 51

FIGURE 6.14: Stress (MPa) vs Time (seconds) for all models with θ = 25 for the time period 0 to 30000 seconds. 52

FIGURE 6.15: Stress (MPa) vs Time (seconds) for all models with θ = 27.5 for the time period 0 to 30000 seconds. 52

FIGURE 6.16: Stress (MPa) vs Time (seconds) for all models with θ = 30 for the time period 0 to 30000 seconds. 53

FIGURE 6.17: Stress (MPa) vs Time (seconds) for all models with θ =30 for the time period 0 to 4000 seconds 53

FIGURE 6.18: Stress (MPa) vs Time (seconds) for all models with θ = 30 for the time period 4000 to 10000 seconds. 54

FIGURE 6.19: Stress (MPa) vs Time (seconds) for all models with O.D = 10 inches, I.D = 6 inches through all values of θ for the time period 4000 to 10000 seconds. 55

FIGURE 6.20: Stress (MPa) vs Time (seconds) for all models with O.D = 10 inches, I.D = 6 inches through all values of θ for the time period 4000 to 10000 seconds 56

FIGURE 6.21: Stress (MPa) vs Time (seconds) for all models with O.D = 10 inches, I.D = 8 inches through all values of θ for the time period 0 to 4000 seconds 57

FIGURE 6.22: Temperature difference (°C) vs Time (seconds) for all models with O.D = 10 inches, I.D = 8 inches through all values of θ for the time period 0 to 4000 seconds. 57

FIGURE 6.23: Temperature difference (°C) vs Time (seconds) for all models with O.D = 10 inches, I.D = 6 inches through all values of θ for the time period 0 to 4000 seconds 58

FIGURE 6.24: Temperature difference (°C) vs Time (seconds) for θ = 20 through all models for the time period 0 to 4000 seconds. 58

FIGURE 6.25: Temperature difference (°C) vs Time (seconds) for θ = 20 through all models for the time period 0 to 4000 seconds 59

FIGURE 6.26: Stress (MPa) vs Temperature difference (°C) for the whole cycle for the model with O.D = 10 inches, I.D = 6 inches for all values of θ. 60

FIGURE 6.27: Stress (MPa) vs Temperature difference (°C) for the whole cycle for the model with O.D = 8 inches, I.D = 6 inches for all values of θ. 61

FIGURE 6.28: Maximum hoop stress vs side tube angle θ for models with cylinder wall thickness t = 2 inches. 64

FIGURE 6.29: Maximum hoop stress vs side tube angle θ for models with cylinder wall thickness t = 1 inch. 64

FIGURE 6.30: Temperature difference vs side tube angle θ for models with cylinder wall thickness t = 1 inch. 65

FIGURE 6.31: Temperature difference vs side tube angle θ for models with cylinder wall thickness t = 2 inches 66

FIGURE 6.32: Temperature result validation plot 66

FIGURE 6.33: Model with θ =30 67

FIGURE 6.34: Model with θ = 45 67

FIGURE 6.35: Model with θ = 60 68

FIGURE 6.36: Stress (MPa) vs Temperature difference for the model with O.D = 10 inches, I.D = 7 inches for all values of θ 68

FIGURE 6.37: Stress (MPa) vs time (seconds) for the model with θ = 20 and O.D = 10 inches with wall thickness t = 1 inch, 2 inches and 1.5 inches. 69

FIGURE 6.38: Stress (MPa) vs Temperature difference for θ = 20 and 70

O.D = 10 inches with wall thickness t = 1 inch, 2 inches and 1.5 inches.

FIGURE 6.39: Hoop stress vs Temperature difference comparison between equation results and ABAQUS results for 10_8_35 73

FIGURE 6.40: Combined hoop stress and the hoop stress due to temperature difference alone against time for model with OD = 10 inches and ID = 6 inches and tube angle 20º 75

FIGURE 6.41: Combined hoop stress and the hoop stress due to temperature difference alone against time for model with OD = 10 inches and ID = 6 inches and tube angle 30º 75

FIGURE 6.42: Combined radial stress and the radial stress due to temperature difference alone against time for model with OD = 10 inches and ID = 6 inches and tube angle 20º 76

FIGURE 6.43: Combined radial stress and the radial stress due to temperature difference alone against time for model with OD = 10 inches and ID = 6 inches and tube angle 30º 76

FIGURE 6.44: Combined hoop stress and the radial stress due to temperature difference alone against time for model with OD = 10 inches and ID = 8 inches and tube angle 30º 77

FIGURE 6.45: Combined radial stress and the radial stress due to temperature difference alone against time for model with OD = 10 inches and ID = 8 inches and tube angle 30º 77

FIGURE 6.46: Model with middle tube angle 20 degrees and last tube angle 40 degrees 79

FIGURE 6.47: Model with middle tube angle 20 degrees and last tube angle 40 degrees 79

FIGURE 6.48: Model with middle tube angle 20 degrees and last tube angle 40 degrees 80

FIGURE 6.49: Model with middle tube angle 20 degrees and last tube angle 40 degrees 80

FIGURE 6.50: Nodes for result processing and plots 81

FIGURE 6.51: Hoop stress vs time period of the first tube for all three side tube stub models 82

FIGURE 6.52: Temperature difference vs time period of the middle tube for all three side tube stub models 82

FIGURE 6.53: Hoop stress vs time period of the last tube for all three side tube stub models 83

FIGURE 6.54: Temperature Difference vs time period 83

FIGURE 6.55: Hoop stress vs time period of the first ligament for all three side tube stub models 85

FIGURE 6.56: Hoop stress vs time period of the first ligament for all three side tube stub models 85

CHAPTER 1: INTRODUCTION

Almost 75% of the world's electricity is still being generated by steam turbines moving rotary generators. Any system involving steam as a prime mover makes use of a steam distribution header to ensure proper distribution of steam from boiler to the generator. With such a large scale of application, steam header design is a vital part of any steam distribution system. Improper designs can lead to catastrophic failures and the high pressures and temperature at which steam is used in these plants have resulted in loss of life and property. Due to these factors, it is of great importance to understand the behavior of steam headers and the various stresses developed within them during a normal operating cycle.

Steam headers are universally cylindrical and are subject to cylinder stress when operated under normal operating conditions. The study of the cylinder stress is crucial during the design of such vessels as they can lead to part failure by rupture if left unchecked. The pressure difference experienced during the operation results in circumferential stresses or hoop stresses in addition to axial and radial stresses. The material chosen was the analysis is grade 91 steel (SA335-P91).

Table 1.1:Chemical composition of grade 91 steel - SA335-P91 (%) [17]

C	Mn	P	S	Si	Cr	Mo	V	N	Ni	Al	Nb
0.08-0.12	0.3-0.6	.02	.01	0.2-0.5	8.0-9.5	0.85-1.05	0.18-0.25	0.03-0.07	0.4	0.04	0.06-0.10

P 91 steel can maintain its physical strength even at the higher end of the operating temperature range and also increased oxidation resistance. The percentage of chromium present in P 91 is close to 9 % of the composition. This enables the alloy to maintain its strength at higher temperatures and gives it its high temperature oxidation resistance properties. The manufacturing process of this particular alloy also plays a vital role in producing the microstructures responsible for high creep strength properties. The alloy is formed by normalizing at 1050 DEG C followed by air-cooling down to 200 DEG c. This is then tempered by heating to 760 DEG C. The alloy's microstructure formation depends primarily upon the heating and cooling rates maintained during formation. Failing to adhere to the recommended rates may result in poor mechanical properties and is a common cause of failure. Due to this reason, it is important that the alloy be formed under strict supervision with emphasis on the heating and cooling rates that enable the formation of the required microstructure [1]. Since the welding process can negatively impact the microstructure, it is required that the alloy be heat treated to reverse the thermal effects of welding on the material so that the microstructure returns to its required state after the weld is done. This step is crucial in maintaining the strength and integrity of P 91 steel. This makes it an ideal candidate for high temperature application, especially in the power generation industry where it is been in extensive use for the last decade.

Steam distribution header are subject to temperatures in the range of 20-600 degree Celsius and internal pressure of around 30 MPa during normal operations. The material they are made out of needs to be able to withstand such high temperatures, pressures and must not fail from the extreme fluctuations in these operating conditions. Grade 91 steel is commonly used as a steam distribution header material due to its robust nature and its

ability to withstand cyclic loading involving such high temperature and pressure ranges over a period of time [1]. Fatigue and creep properties play a major role in determining the materials of steam header.

Figure 1.1: Hoop stress failure [2]

CHAPTER 2: MODELLING

One quadrant of a section of the steam header arrangement with a single side tube penetration was modelled and simulated in ABAQUS. Thirty models of the same quadrant with varying side tube angles and varying wall thickness were modelled in ABAQUS. The quadrants were modelled and then the respective symmetry boundary conditions were applied to simulate the entire structure. The models were created and executed using python scripts. The fig 2.1 and 2.2 represent the full header section and a cutaway.

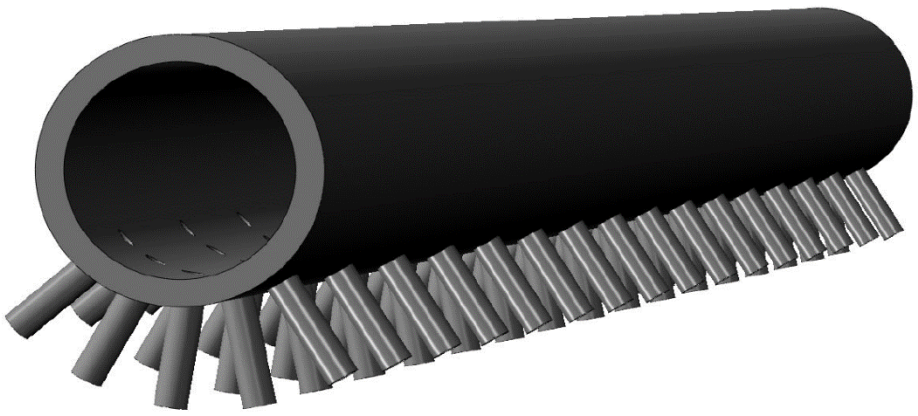

Figure 2.1: The complete section of the header

Python scripting facilitated the creation and simulation of a large number of models within a short time frame as the models simulated similar in general profile. The variations in the side tube angles and the wall thickness were scripted into the base python script and submitted for analysis. The entire model was created and treated as a single section and the

material properties of AS335 P91 Steel was prescribed. The material properties were prescribed as temperature dependent variables.

Figure 2.2: Steam header model cut-away

The side tube penetration angle is the angle between the vertical YZ plane of symmetry of the model and the side tube penetration. Side tube penetration angles from the steam header were varied from 20 degrees to the vertical right up to 30 degrees through increments of 2.5 degrees. The other variable physical parameter was the inner and outer diameter of the main header section. The outer diameter was varied from 8 inches to 10 inches through 1-inch increments and the inner diameter was varied from 5 inches to 8 inches through 1-inch increments. The main section that was modelled has one side tube penetration with and one quadrant of the entire section was designed and analyzed.

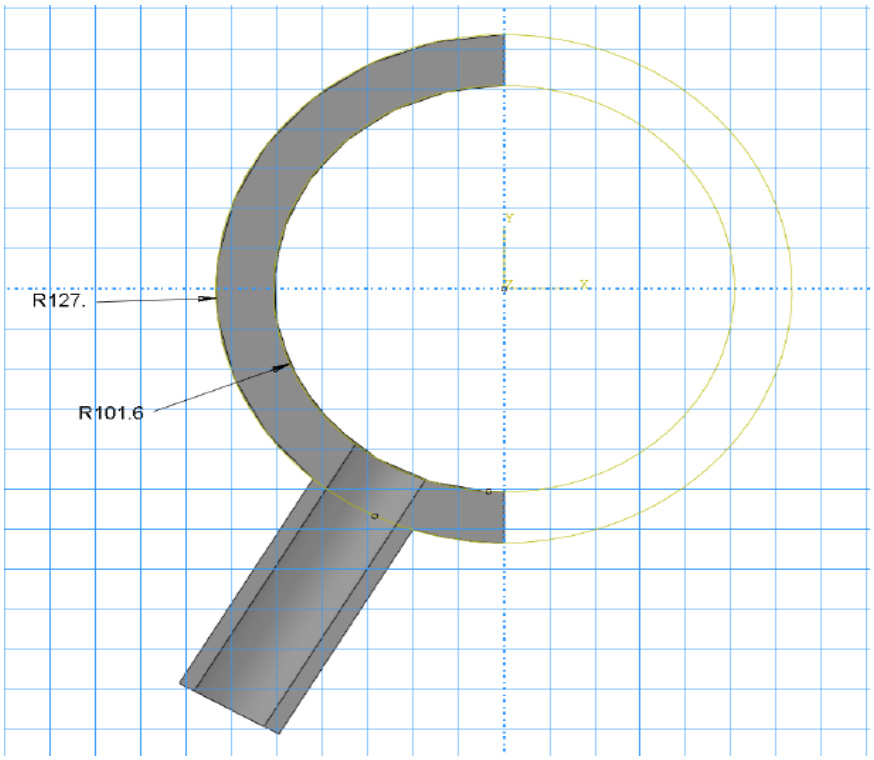

Figure 2.3: Radial dimensions of the model

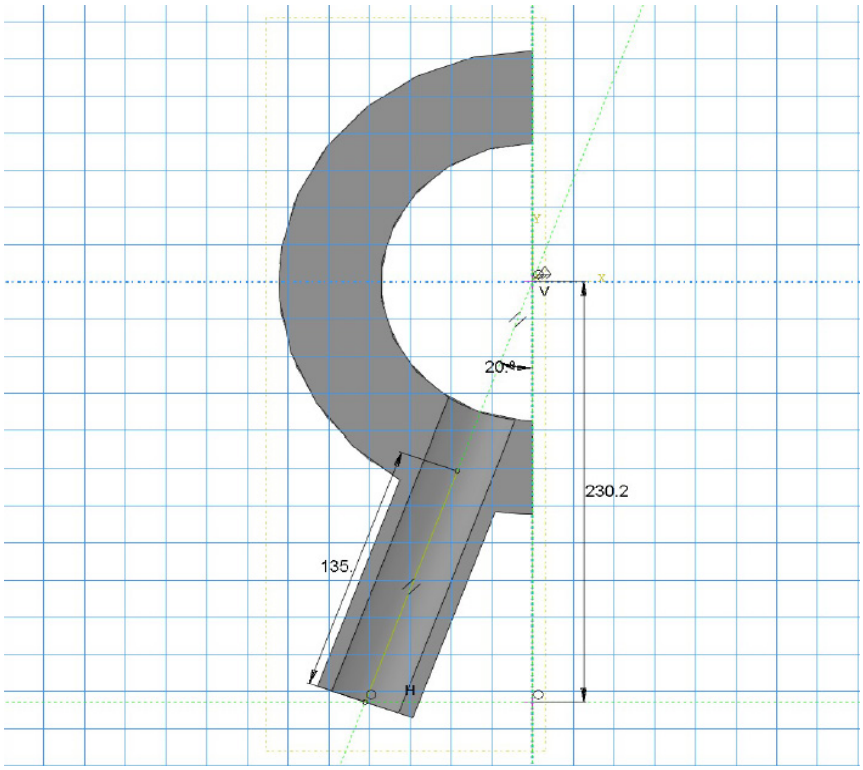

Figure 2.4: Angular dimensions of the side tube

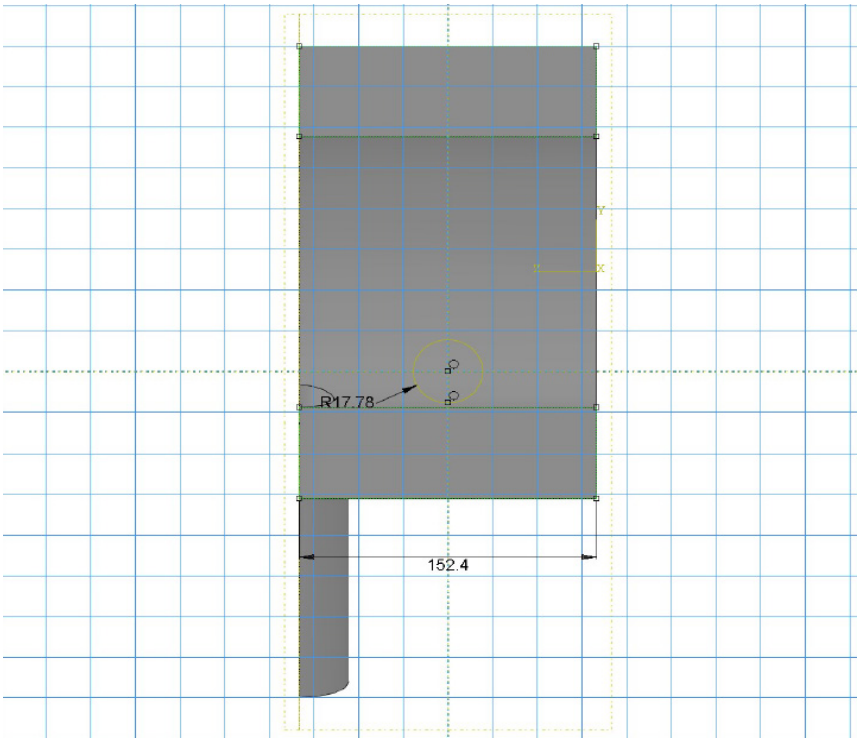

Figure 2.5: Length of the header segment

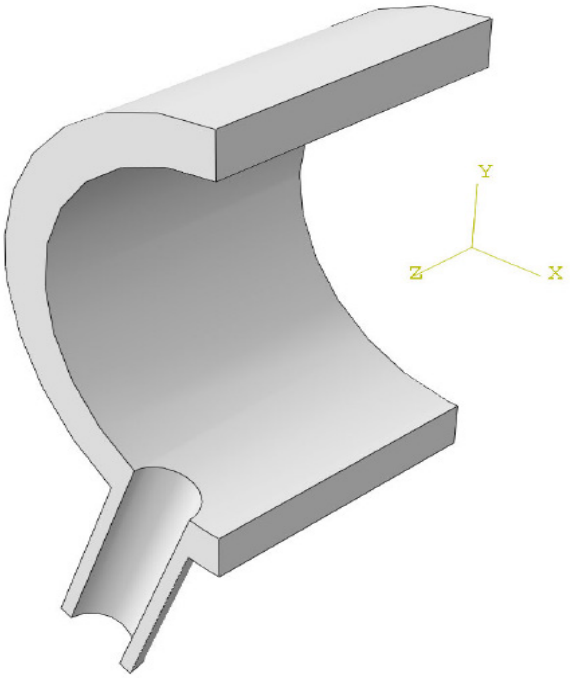

Figure 2.6: General specifications of the model

The fig 2.3 shows the basic dimensions used to model the quadrant that was used for analysis. The second fig 2.4 shows the side tube angle. This was the primary variable that was changed and the stress behavior was analyzed accordingly.

Modelling and analyzing the entire model over 30 times would be extremely expensive in terms of computational resources and so the symmetry boundary condition available in ABAQUS was used to cut down the size of the analysis domain by a factor of two. The boundary conditions used were verified by running the simulations of the models with only the internal pressure loads. These results were then compared with the cylinder stresses obtained in a thick walled vessel using the cylinder stress equations. The results from the simulation differ from the results from the equation by a margin of 1 to 2 percent. This margin of error can be attributed to the presence of the side tube penetrations, which deviate the results from the ones obtained from the equation as the equation is meant for a perfectly closed thick walled cylindrical pressure vessel.

2.1 Nomenclature

Throughout the length of this thesis, due to the results of 30 models being discussed in detail, the model names follow the nomenclature pattern of A_B_C where A is the outer diameter in inches, B is the inner diameter in inches and C is the angle of the side tube penetration of the model. For example, a model with the title 10_8_20, refers to a model with an outer diameter of 10 inches, inner diameter of 8 inches and the side tube penetration angle of 20 degrees. Fig. 2.7 and Fig 2.8 show the variation of the side tube angle.

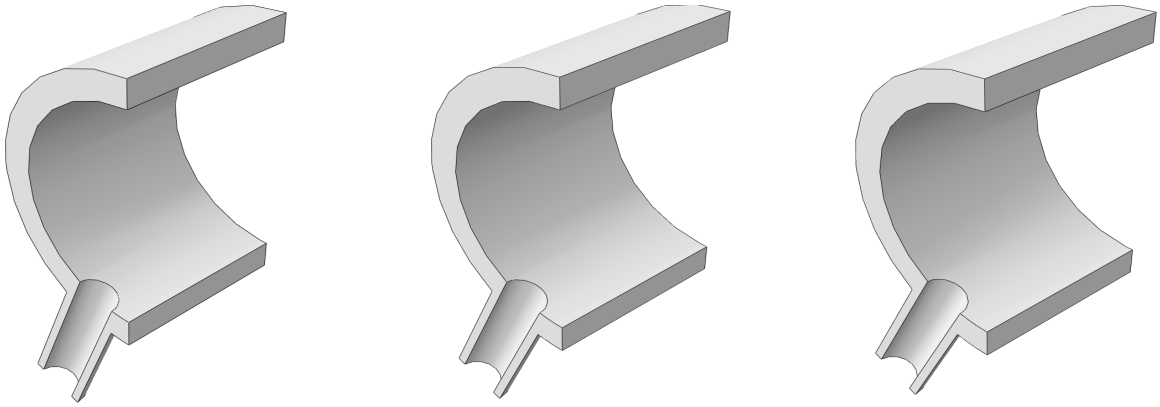

a) b) c)

Figure 2.7: Models with varying side tube angles. (a) side tube angle 20 degrees, (b) side tube angle 22.5 degrees, (c) side tube angle 25 degrees.

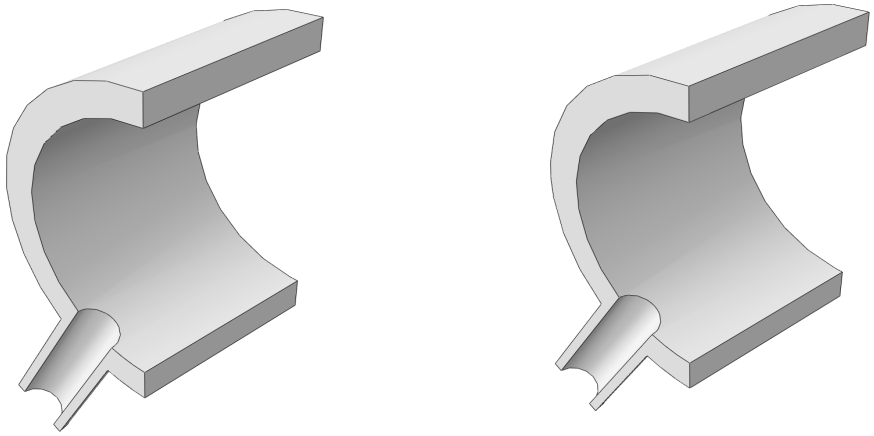

a) b)

Figure 2.8: Models with varying side tube angles. (a) side tube angle 27.5 degrees, (b) side tube angle 30 degrees.

CHAPTER 3: SETTING UP THE SIMULATION

3.1 Material Properties and Operating Cycle

The material properties of grade 91 steel were used for the analysis. ABAQUS by default does not have any units and lets the user define the consistency if units when modelling. These units were used for the material model. All the material properties used were specified as time dependent material properties. These properties were converted into consistent units so that the ABAQUS results would be coherent.

Table 3.1: Material Properties of grade 91 steel [18]

Temperature, $[C]$	Coefficient of Thermal Expansion $[/C]$	Thermal Conductivity, $[W/m\ /C]$	Thermal Diffusivity, $[m^2/s]$	Elasticity Modulus, $[MPa]$
20		22.3	6.61×10^{-6}	213000
100	1.09×10^{-5}	24.4	6.74×10^{-6}	208000
200	1.13×10^{-5}	26.3	6.71×10^{-6}	205000
300	1.17×10^{-5}	27.4	6.39×10^{-6}	195000
400	1.20×10^{-5}	27.9	5.87×10^{-6}	187000
500	1.23×10^{-5}	27.9	5.22×10^{-6}	179000
550	1.25×10^{-5}	27.8	4.85×10^{-6}	174000
600	1.27×10^{-5}	27.6	4.42×10^{-6}	168000

The operating cycle used must be as close as possible to the normal operating cycle of a steam header. One cycle of the operating load is prescribed in ABAQUS. The primary load is the internal pressure load and the end load due to the internal pressure acting on the end caps of the closed steam header. The temperature condition was prescribed through the surface film coefficient property in ABAQUS. The surface film coefficient was prescribed as a time dependent amplitude with the sink temperature applied as the temperature load. A predefined field of 20 degree Celsius was applied throughout the system as the operating cycle used is taken as the first cycle.

Table 3.2: Operating cycle used for the simulation [18]

Time, $[min]$	Pressure $[Mpa]$	Temperature, $[C]$	Film Coefficient, $[W/m^2/C]$
0	0	20	0
10	7.5	400	500
30	7.5	500	500
40	14	600	1000
90	14	600	1000
95	7.5	500	500
417	0	20	500
500	0	20	0

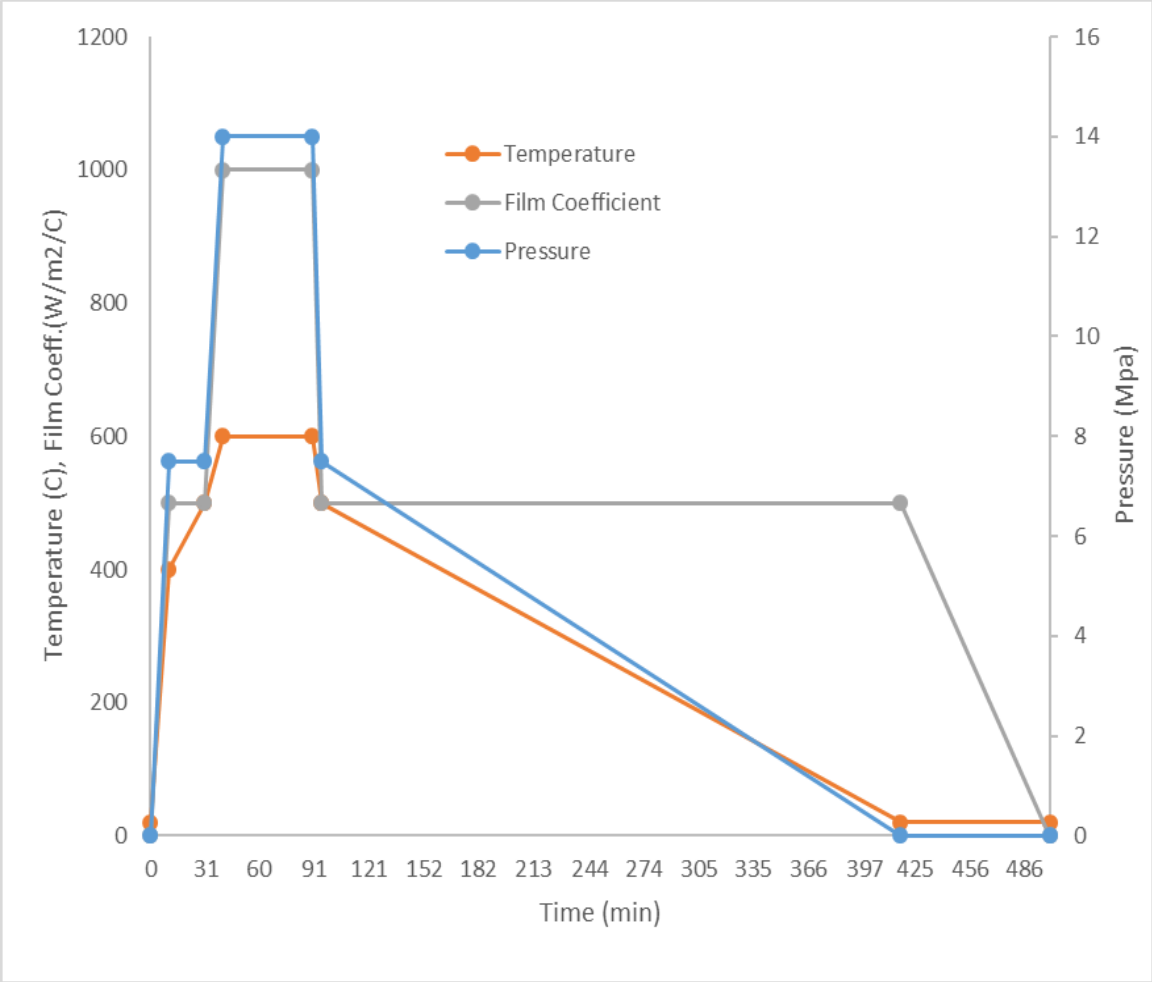

Figure 3.1: Operating cycle vs time period [18]

The three primary loads were input as amplitude loads as they were time dependent. The internal pressure load was input as a direct amplitude load whereas the temperature load was implemented as the sink temperature for the film coefficient condition. The end load factor was calculated and was entered as a direct load. The end load factor was multiplied with the internal pressure load amplitude and then applied.

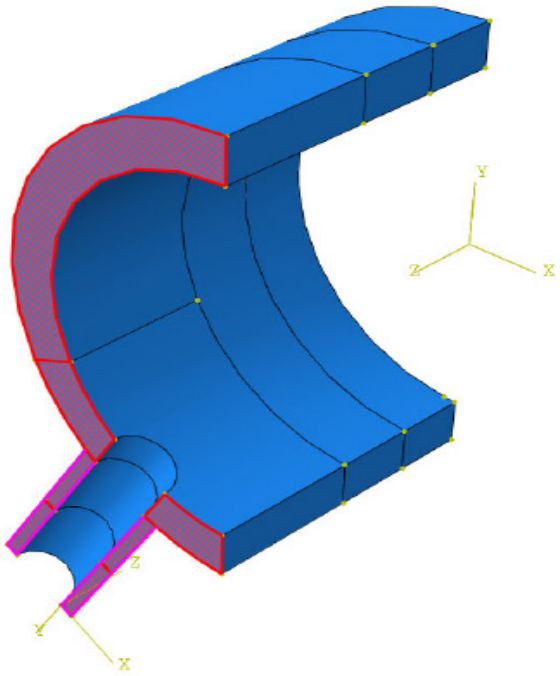

Figure 3.2: Set creation and boundary condition

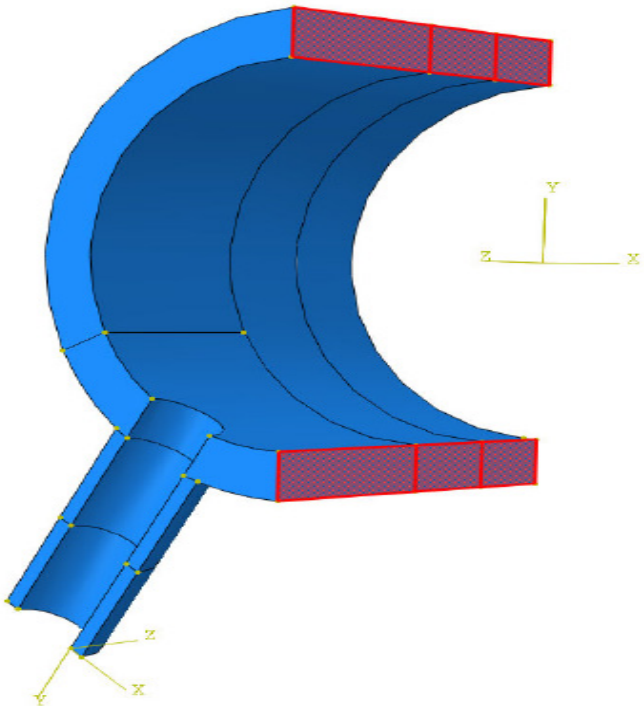

Figure 3.3: Set creation for symmetry along X-axis boundary condition

3.2 Set Creation and Boundary Conditions

The fig 3.2 to fig 3.8 show the sets corresponding to the boundary condition used. These sets are used for easy application of the loads and the boundary conditions. To simulate the model as accurate as possible, the necessary boundary conditions needed to perfectly recreate the working conditions of the header. The boundary conditions were verified using pressure loads and compared to the results obtained using the same pressure values used in this operating cycle. This is discussed in CHAPTER The model to be simulated was just a section of the complete model and hence proper boundary conditions had to be prescribed to simulate the symmetry and movements of the model. Symmetry can be prescribed in ABAQUS using the necessary boundary conditions. The main header section's symmetry along the Z axis is modeled by applying a boundary condition on the face containing the side tube penetration cross section and parallel to the XY plane. This boundary condition constraints the movement along the Z axis whereas it is free to do so in the other two axes. Similarly the symmetry along the X axis is modeled by applying a boundary condition on the cross sectional face lying on the YZ plane. The boundary condition is set to constraint of movement along X axis with free movement along the other two axes. A separate co-ordinate system is prescribed for the side tube to apply symmetry condition of the side tube. The bottom edge is used to prescribe the local coordinate system with two points on the bottom edge of the tube selected as lying along the local X axis. With this as the reference, the coordinate system is constructed and the side tube end is constrained along the local Y axis and free to move along the other two axis to model symmetry of the side tube. The symmetry of the other half of the header section is prescribed by an equation constraint. The constraint is applied to the set of nodes with a

single node taken as their reference. The side tube also subject to a boundary condition where it is in symmetry condition. A local coordinate system is drawn for the side tube so that its boundary conditions are prescribed.

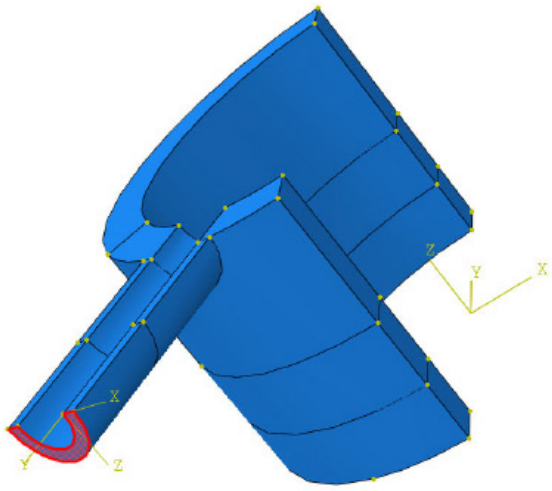

Figure 3.4: Set creation for symmetry of side tube along local Y-axis boundary condition

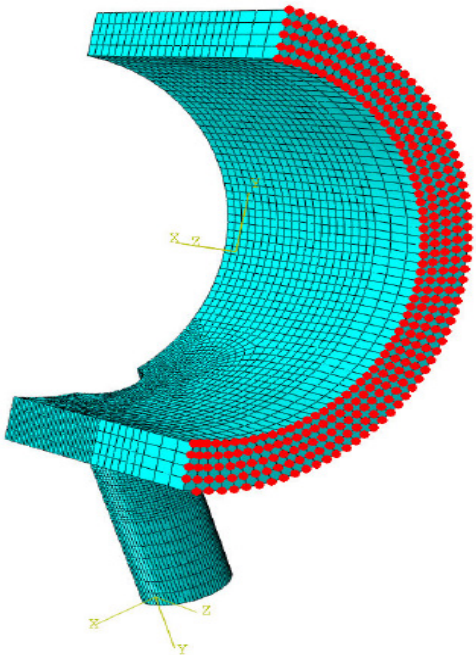

Figure 3.5: Constraint nodes set creation for constraint by equation boundary condition

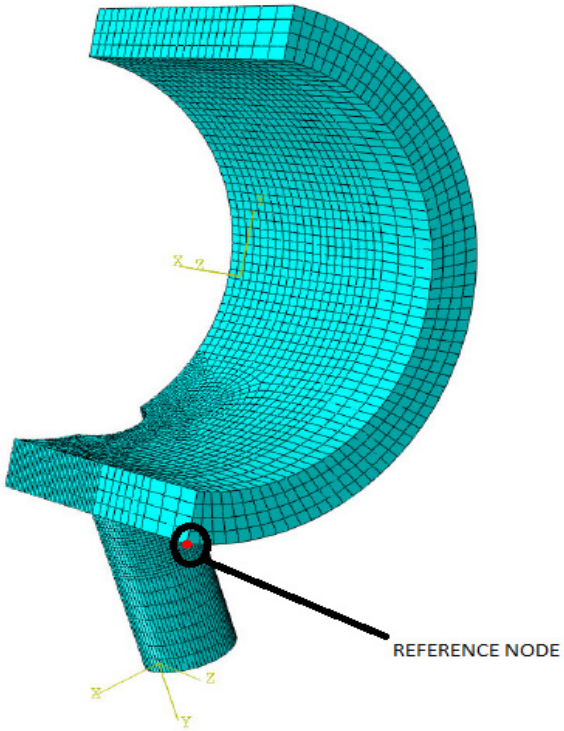

Figure 3.6: Reference node set creation for constraint by equation boundary condition

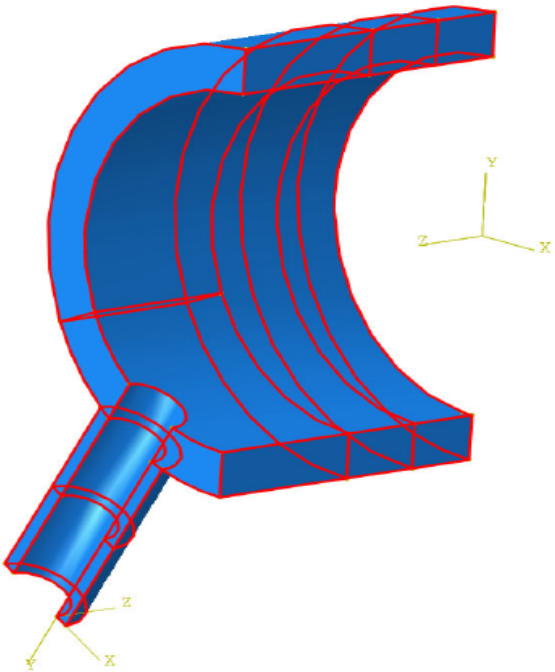

Figure 3.7: Set creation for predefined field to apply the ambient room temperature

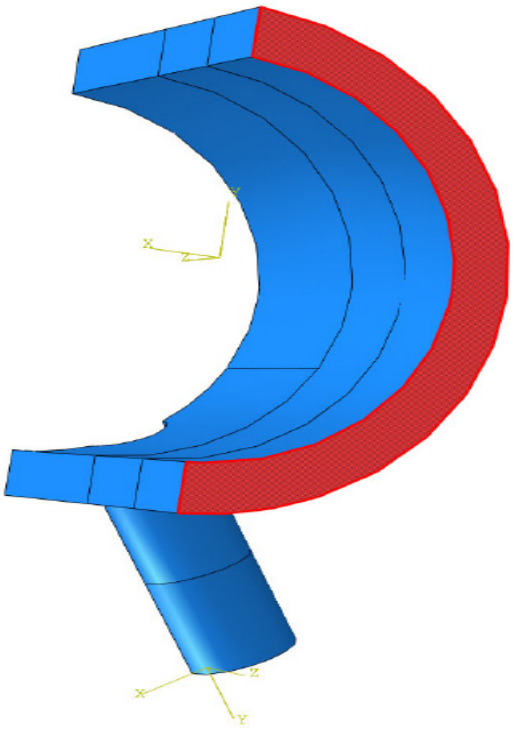

Figure 3.8: End load set creation for end load application

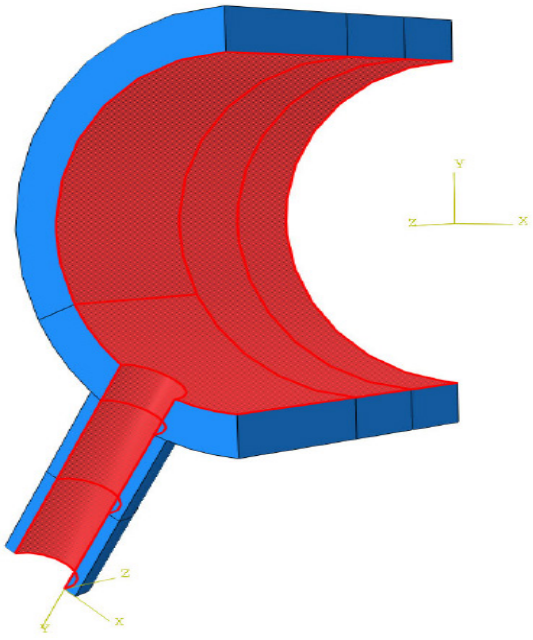

Figure 3.9: Surface load set creation for internal pressure and thermal load

Two surface sets are created for the application of the main load and the end load. The fig 3.8 and fig 3.9 show the surface sets used for the main load and end load. The main load was the internal pressure load acting from within the header tube and since the header is closed on both ends, an end load is applied to the cylinder wall. These two loads are the primary loads and are entered as a time dependent amplitude. The temperature load is also prescribed as a time varying amplitude, but it is specified as the sink temperature for the film coefficient condition. The time dependent film coefficient is also input as an amplitude, with the acting surface being the main surface set.

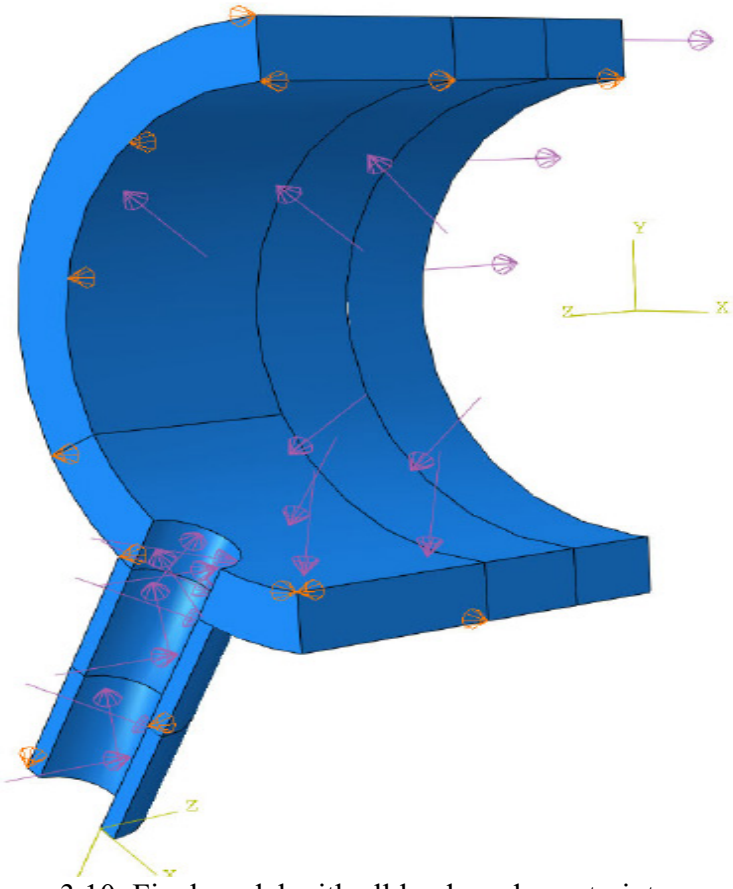

Figure 3.10: Final model with all loads and constraints

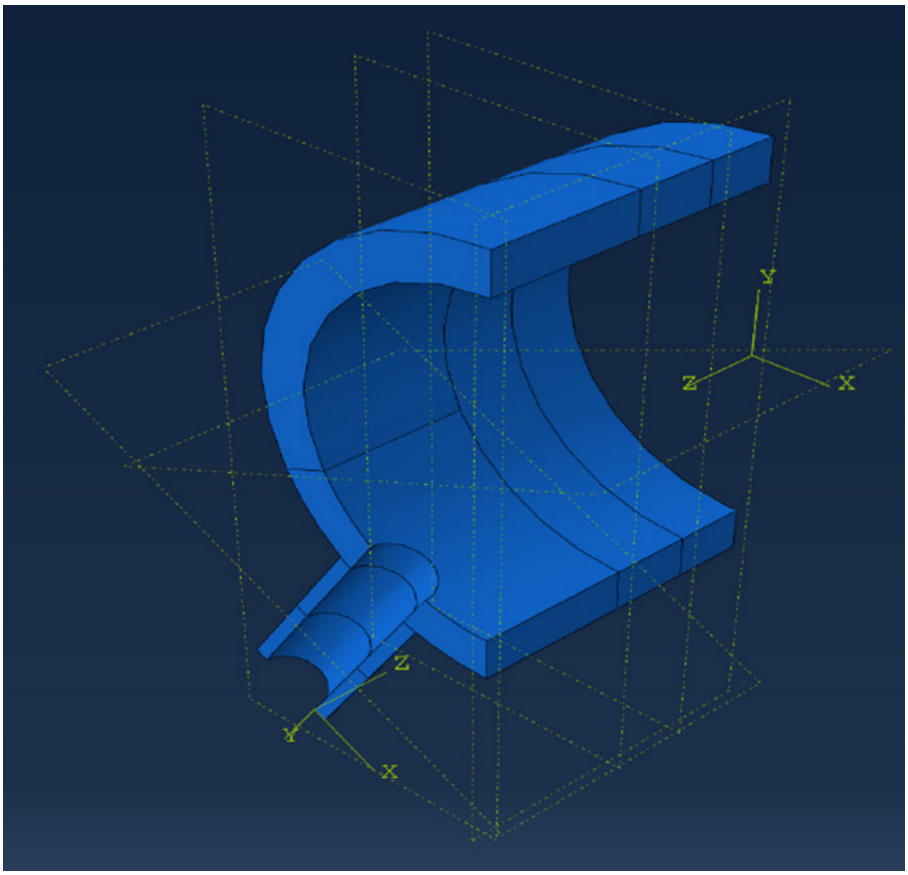

Figure 3.11 Partitioning of the material for a denser mesh

3.3 Partitioning

The initial model consisted of some complex geometrical features that could not be meshed using the default ABAQUS meshing techniques. Implementing a bottom up mesh was also not a viable solution since all 30 models had different profiles, bottom up meshing using python scripting would be considered time consuming and would defeat the purpose of scripting in the first place. To overcome this problem, partitioning was considered as a suitable alternative. The entire model was partitioned into smaller regions using datum planes at different angles. The angles were prescribed based on the side tube penetration angles. This was achieved by altering the scripts to include datum planes based on the side

tube angles. This method was much less time consuming and when it came to meshing it was much less complex than the bottom up method.

3.4 Meshing

Meshing was the most important part of the model prior to simulation. It was expected that the junction on the header segment where the side tube branched out would be the location of maximum hoop stresses by observing simulations of similar sections. This meant that the region surrounding the junction required denser meshing with a higher node count to produce results that were as accurate as possible [9]. The entire model could not be meshed with the same density as that would result in a computationally expensive model and that does not fall in line with the goal of this thesis. This was overcome by

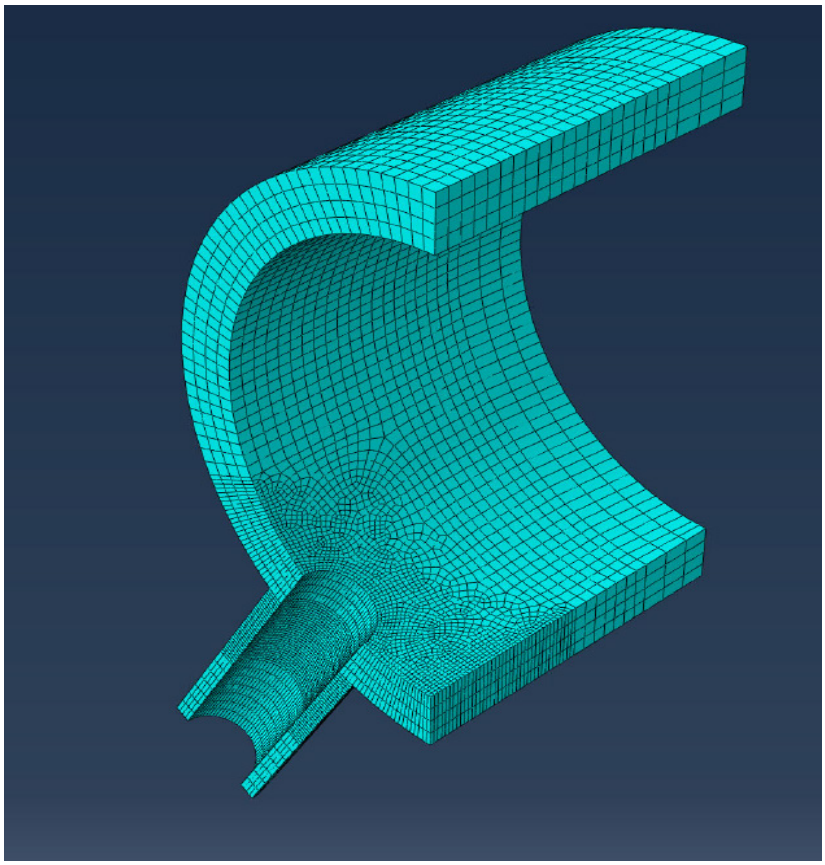

Figure 3.11: Fine and coarse meshes due to partitioning

making use of the partitions created earlier. The script was modified to create an additional partition near the junction area so that it could be meshed at a higher density compared to other areas of the segment. All the 30 models were meshed using the same technique by making appropriate changes to the scripts. On average, all models have an element count of around 15,000 to 16,000 elements in total with the junction of the side tube and main header bearing the highest density of elements.

3.5 Mesh Verification

The mesh verification tool is used to verify the quality of the mesh. Since the model used was meshed using the default options in ABAQUS, verifying the integrity and accuracy of the mesh is very important as a poor quality mesh can result in inaccurate results. The model used in this thesis contains some complex geometries which may result in poor quality meshes when meshed using the default ABAQUS meshing techniques. The shortcomings of this method was offset by partitioning the model. The different regions of partitions were assigned meshes of different sizes to accurately capture the stress evolution in areas where high stresses are expected. All the above mentioned actions raise the probability of errors being present in the meshed model, thus it is crucial that the mesh verification tool is used to identify the quality of the mesh.

From the mesh verification tool results, it is clear that the meshed models fall well within the tolerance limit specified and will produce results that are accurate in capturing the stress and temperature evolution.

3.6 Element Type

A general purpose 20 noded triquadratic displacement, trilinear temperature reduced integration element was used for this analysis namely C3D20RT. This particular

element was chosen for the coupled analysis. It is a general purpose element with 20 nodes that effectively captures the stress distribution in a coupled temperature-displacement analysis. Due to the presence of the integration points at about one quarter of the typical element size away from the element boundary, the integration point values are extrapolated trilinearly and thus the mesh needs to be much finer where the high stress concentrations are expected. This is one among the primary reasons why the modeled was partitioned earlier in such a way that the high stress concentration areas have a finer mesh compared to the other areas. Even though it is a reduced integration element with lesser integration points, this element does not exhibit the hour-glassing behavior. The analysis is entirely elastic and thus this particular element type captures the stress values to a higher degree of accuracy compared to other elements.

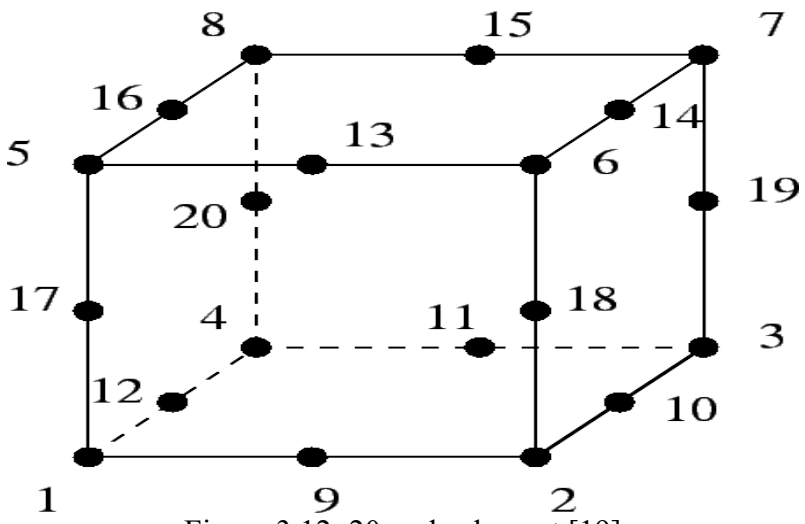

Figure 3.12: 20 node element [19]

ABAQUS recommended this element as a default for the model that was used for this simulation. This element is not recommended for plastic problems where the value of poisons ratio is significantly higher.

3.7 Step

This analysis is a coupled temperature-displacement analysis. It is a highly nonlinear analysis where both the thermal and mechanical conditions are solved simultaneously. The nature of the operating cycle of a steam distribution header warrants this procedure type. This analysis includes the mechanical effects of the temperature conditions and also the temperature effects of the mechanical conditions and simultaneously solves for the result. The nominal cycle that was used in the models consist of the steam temperature cycle which acts as the temperature load and the internal pressure acting on the system due to the high pressure steam as the mechanical load, both of which need to be solved simultaneously to arrive at the required result. The time period of the cycle prescribed is 500 minutes. ABAQUS by default does not have any units and relies upon the user to prescribe the units for the analysis. For this simulation, the unit chosen for time is seconds. All the material properties were converted to suit this unit. The loads that were applied as amplitudes were also converted for seconds and the appropriate values for the appropriate time in seconds was used in the amplitude curve. The step duration was chosen as 30000 seconds for the entire cycle of 500 minutes. The response parameter is set as transient in the step creation module as the entire cycle and the analysis is primarily time dependent we need the stress distribution and temperature difference results that vary over time.

The time increment was set at a maximum of 2000 increments with the maximum increment size set at 1000. The minimum increment was capped at 1E-005 with the initial increment of 1. These particular numbers were chosen to reduce the size of the finals result file and also by some trial and error to find the sweet spot at which the solver converges,

resulting in a results of higher degree of accuracy while keeping computational time, costs and space at a minimum. This was a critical step in the analysis as 30 models needed to simulated and all their results needed to be processed. The load variation with time option was set at instantaneous to simulate the operating cycle with a higher degree of accuracy. The frequency of output to be recorded was set to be at every 20 increment to further save storage space and reduce processing times. It was important that this analysis was done in the most efficient way in terms of computational cost and time as the number of simulations involved meant that it would be counterproductive if the outputs were recorded for every iteration and provided the same degree of accuracy offered by recording the output for every 20 iterations.

CHAPTER 4: VERIFICATION

The prescribed boundary conditions need to be verified before the model is submitted for final simulation. The verification can be done by simulating the models by applying only the internal pressure load and verifying the results with the results obtained using the equations for hoop, axial and longitudinal stresses in thick walled cylinders. The results of the comparison yielded almost similar results with negligible error margins. It is suspected that the margin of error is primarily due to the presence of the side tube penetrations as the equations used do not account for them. To further mitigate the effect of the side tubes, the location chosen for the values to be observed was at farthest possible from the side tube junction. This verification concludes that the initial boundary conditions applied successfully replicate the symmetry of the model. This procedure reduced the computational power required to run the simulation by a factor of 4 as only a single quadrant of the model is used. This is one of the key advantages of Computational FEA.

4.1 Axial Stress

The stress in axial direction at a point in the tube or cylinder wall can be expressed by the following equation

$$\sigma_a = \frac{(p_i r_i^2 - p_o r_o^2)}{(r_o^2 - r_i^2)} \tag{4.1}$$

Where σ_a= stress in axial direction (MPa, psi), p_i= internal pressure in the tube or cylinder (MPa, psi), p_o = external pressure in the tube or cylinder (MPa, psi), r_i = internal radius of tube or cylinder (mm, in) and r_o = external radius of tube or cylinder (mm, in)

4.2 Circumferential Stress

The stress in circumferential direction - hoop stress - at a point in the tube or cylinder wall is given by the following equation

$$\sigma_c = \left[\frac{(p_i r_i^2 - p_o r_o^2)}{(r_o^2 - r_i^2)}\right] - \left[\frac{r_o^2 r_i^2 (p_o - p_i)}{(r^2 (r_o^2 - r_i^2))}\right] \quad (4.2)$$

Where σ_c = stress in circumferential direction (MPa, psi), r = radius to point in tube or cylinder wall (mm, in) *($r_i < r < r_o$)* and maximum stress when $r = r_i$ (inside pipe or cylinder)

4.3 Radial Stress

The stress in radial direction at a point in the tube or cylinder wall is given by the following equation

$$\sigma_r = \left[\frac{(p_i r_i^2 - p_o r_o^2)}{(r_o^2 - r_i^2)}\right] + \left[\frac{r_o^2 r_i^2 (p_o - p_i)}{(r^2 (r_o^2 - r_i^2))}\right] \quad (4.3)$$

Where maximum stress when $r = r_o$ (outside pipe or cylinder)

4.4 Verification

Using the above equations, the following stresses were calculated for one model with the following dimensions p_i = 14 MPa, r_i = 101.6 mm (4 in), r_o = 127 mm (5 in), r = 101.6 mm (On the inner wall of the header).

The corresponding stresses were calculated and their values are,

σ_a = 24.9 MPa

σ_c = 63.8 MPa

σ_r = -14 MPa

To verify this, a sample simulation is run on the same model with the internal pressure load set as the only load acting on the model. The results of that simulation are represented in the following figures.

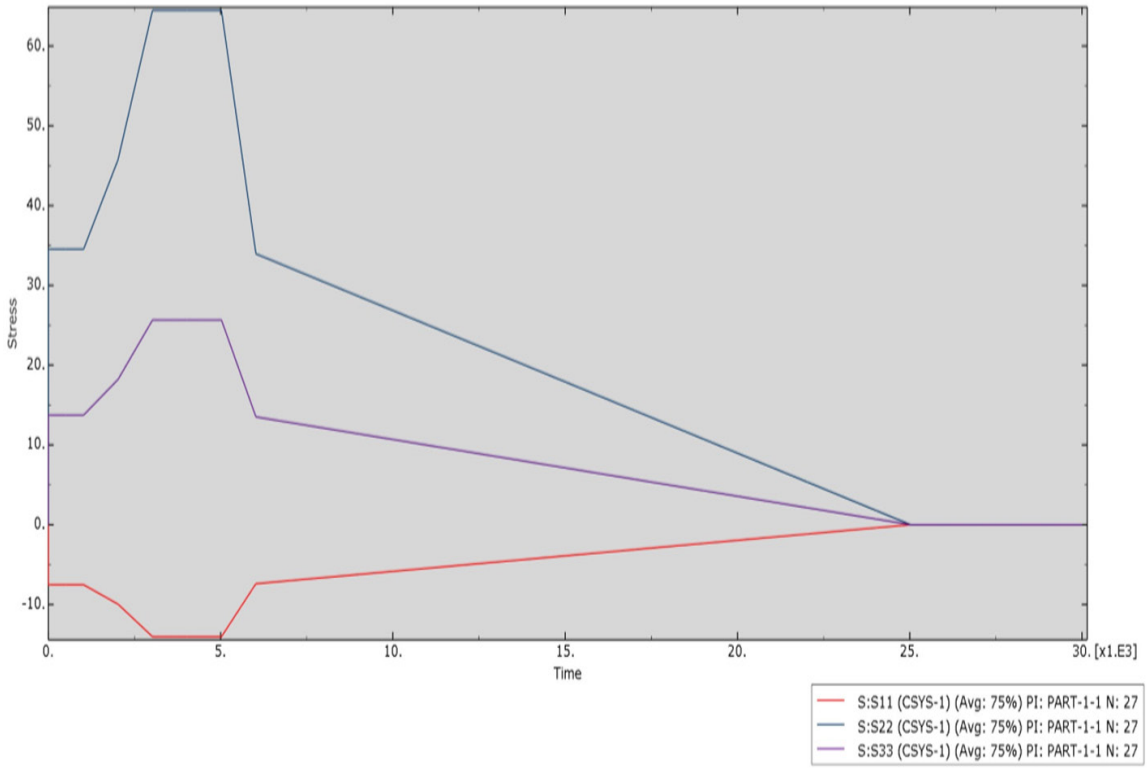

.Figure 4.1 : Verification stresses from the simulation

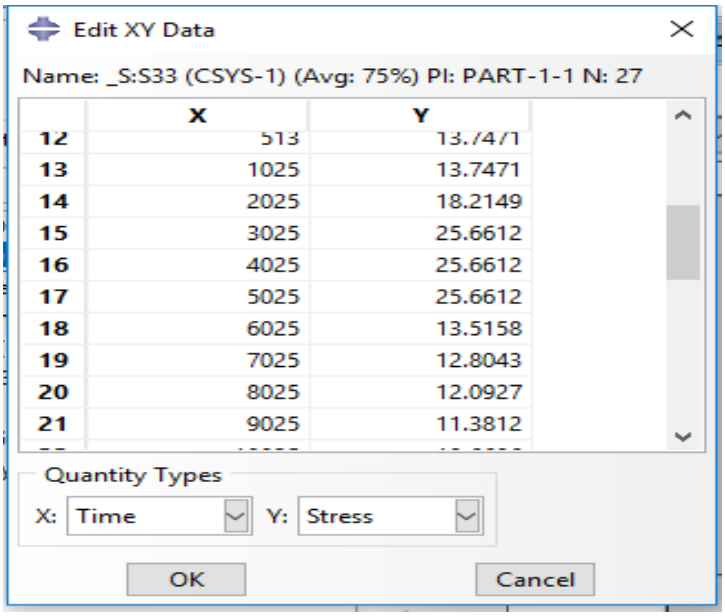

Figure 4.2: Maximum axial stress from simulation

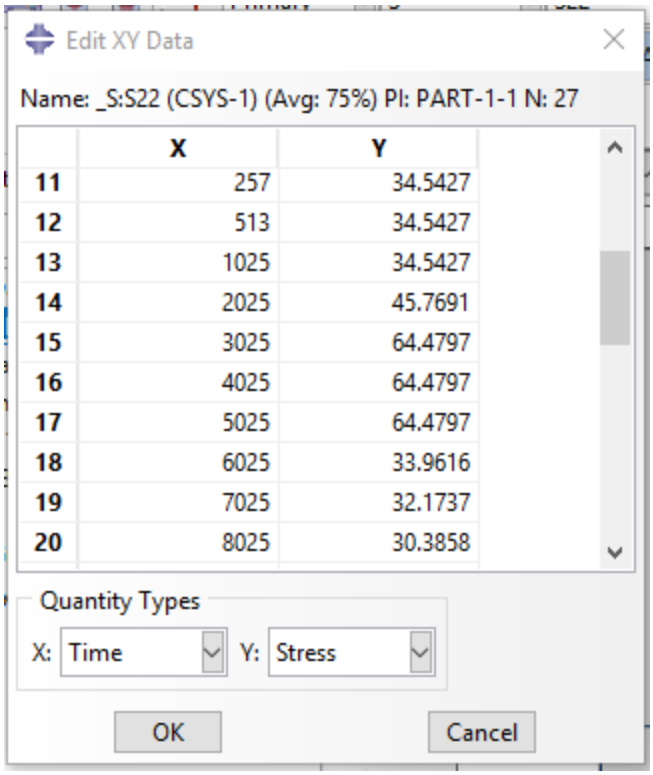

Figure 4.3: Maximum circumferential stress from the simulation

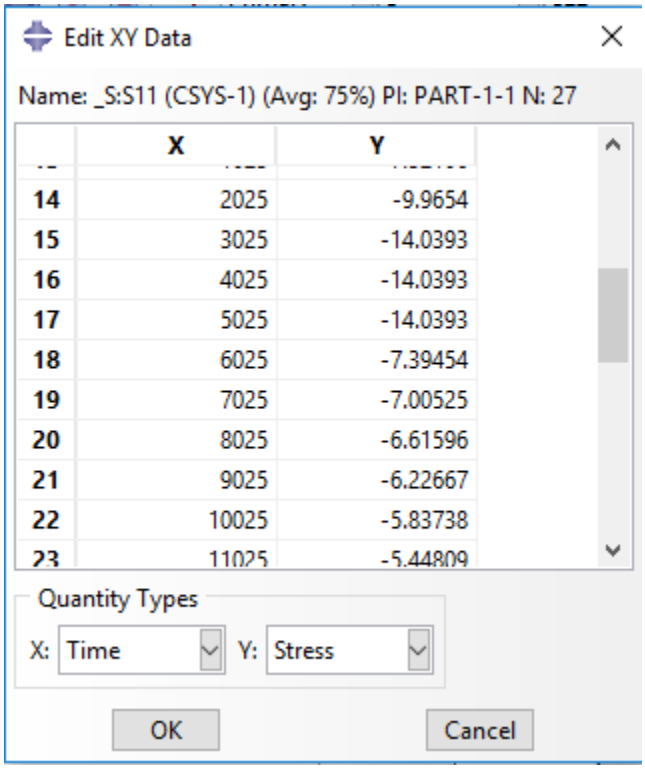

Figure 4.4: Maximum radial stress from the equation

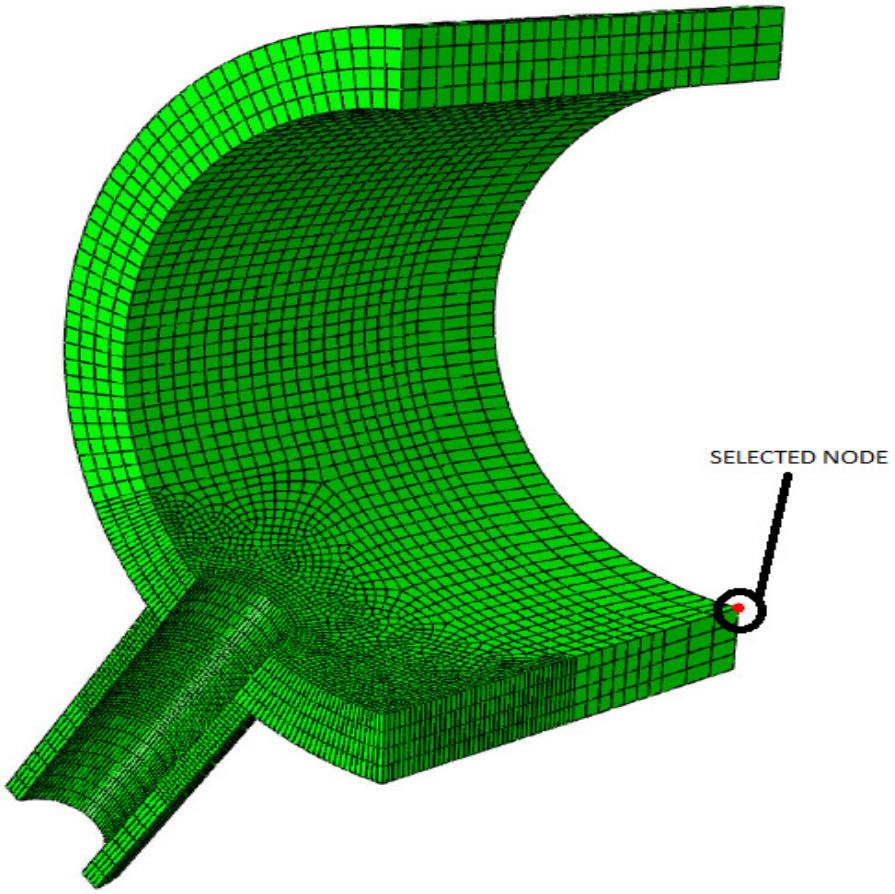

Figure 4.5: Location of the node chosen for verification

The node chosen as shown in fig 4.5 was selected as it was the node farthest from the side tube. The presence of the side tube would produce some distortion in the results as the verification equations are for a closed thick walled cylinder. The minor deviations from the value calculated using the equations could also be attributed to this.

The same verification process was done for each model from the set of six model groups to make sure that all the boundary conditions prescribed to the models were in line with the operating conditions. All the models displayed similar levels of accuracy, thereby verifying that the boundary conditions used are the required boundary conditions.

CHAPTER 5: THEORY

The fully coupled thermal displacement analysis is chosen for simulations in which the temperature affects the stress concentration and the stress concentration in turn affects the temperature field. To effectively model this simulation, ABAQUS makes use of elements with both temperature and displacement degrees of freedom. This type of analysis is usually chosen for metalworking where the inelastic deformation creates a significant temperature field and the created temperature field in turn affects the inelastic behavior. In these cases the results of both temperature and stress must be calculated simultaneously and ABAQUS accomplishes this by using the coupled temperature displacement elements. In this simulation ABAQUS standard solver was used and with a transient thermal response.

5.1 ABAQUS

A backward-difference scheme is used to integrate the temperatures and for nonlinear coupled system, Newton's method is used. Both exact and an approximate implementation of Newton's method is used.

5.1.1 Exact Implementation

It is done by using a nonsymmetrical Jacobian matrix as show in the following matrix equations representing coupled equations [10].

$$\begin{bmatrix} K_{uu} & K_{u\theta} \\ K_{\theta u} & K_{\theta\theta} \end{bmatrix} \begin{Bmatrix} \Delta u \\ \Delta\theta \end{Bmatrix} = \begin{Bmatrix} R_u \\ R_\theta \end{Bmatrix} \tag{5.1}$$

Where Δu and $\Delta\theta$ are corrections to the incremental displacement and temperature respectively, K_{ij} are the submatrices of the fully coupled Jacobian matrix and the mechanical and the thermal residual vectors are R_u and R_θ respectively. The mechanical

and thermal equations are solved simultaneously. This system of equation is solved with the use of unsymmetrical matrix storage and solution scheme. Quadratic convergence is achieved when the solution estimate is within the radius if convergence of the algorithm. The default mode makes use of this exact implementation.

5.1.2 Approximate Implementation

Some type of problems require a weak coupling between the thermal and mechanical solutions that are evolving simultaneously. This equates to the off diagonal submatrices $K_{u\theta}, K_{\theta u}$ being small compared to the components of the diagonal submatrices$K_{uu}, K_{\theta\theta}$. For these problems. Setting the off diagonal term to zero is a solution that can be less expensive computationally so that we obtain an approximate set of equations.

$$\begin{bmatrix} K_{uu} & 0 \\ 0 & K_{\theta\theta} \end{bmatrix} \begin{Bmatrix} \Delta u \\ \Delta\theta \end{Bmatrix} = \begin{Bmatrix} R_u \\ R_\theta \end{Bmatrix} \tag{5.2}$$

Using this technique, both thermal and mechanical equations can be solved separately as there are fewer equation in each sub problem. This results in a reduction in the solver time by iteration by a factor of two with similar and significant savings in solver storage of factored stiffness matrix. In most situations, the sub problems are either fully symmetric or approximated as symmetric so that the symmetric storage and solution scheme can be used and it is less costly. This saves solver time by another additional factor of two. In the modified form of Newton's method, the fully coupled effect is considered through the residual vector R_j at each increment of time and hence does not affect the solution accuracy. This makes the rate of convergence switch from quadratic and depends on the magnitude of the coupling effect. And more iterations are needed to attain equilibrium compared to the exact implementation. Thus a significant coupling results in a

very slow convergence rate that may prohibit obtaining the solution and in places like these an exact Newton implementation is needed. Even in places where the approximation implementation is used, the convergence strongly depends on the first guesses' quality and is controlled by selecting the method of the extrapolation step.

5.1.3 Steady State

An arbitrary time scale is applied to the step and this can be performed in Abaqus/Standard. The time period and the time incrementation are specified by the user.

5.1.4 Transient Analysis

This is the other analysis that can be performed. The time incrementation can be controlled directly here, or the Abaqus'/Standard can be controlled automatically and the latter is preferred. These time increments can be selected based on the maximum allowable nodal temperature change in an increment, $\Delta\theta_{max}$. Abaqus makes sure that the time increments are adjusted accordingly so that this max allowable temperature change at the nodes in an increment does not change.

5.1.5 Spurious Oscillations

In transient analysis, the guidelines defining the relationship between the minimum usable time increment and the element size is given by

$$\Delta t > \frac{\rho c}{6k}\Delta l^2 \tag{5.3}$$

Where Δt is the time increment, ρ is the density, c is the specific heat, k is the thermal conductivity, and Δl is a typical element dimension, like the element's length on one side. If the time increments chosen are smaller than this are used in a second-order element mesh, then spurious oscillations can appear in the solution, most commonly in the vicinity of boundaries with rapid temperature changes. These cause problems if

temperature dependent material properties are prescribed and they are also nonphysical. Using first order elements these oscillations can be eliminated by lumping the heat capacity terms, but the solutions may be inaccurate for small time increments. This can be rectified by employing finer meshes at regions of rapid temperatures changes.

5.2 Temperature effects and stress

An equation relating the temperature difference and the maximum hoop stress induced is required to establish how the stresses evolve during the given cycle. Consider a wire of length *l* fixed at one end and free on the other end, is subjected to a temperature rise of ΔT. The wire will elongate by Δl as shown in fig 5.1.

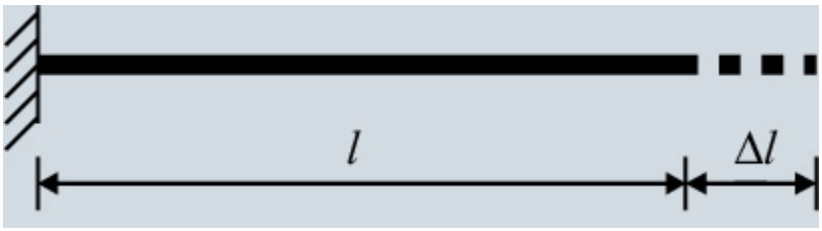

Figure 5.1.: Wire segment

The length of this extension is given by the formula

$$\Delta l = \alpha \Delta T l \tag{5.4}$$

Where α is the coefficient of thermal expansion of the material of the wire with the units $\frac{1}{°\mathrm{F}}$, *l* is the original length of the wire. The value of α depends upon the material of the wire. Now assume that this wire of length *l* is bound on both sides and subjected to a temperature change of ΔT. This change in temperature causes the wire to elongate but since it cannot elongate as it is bound on both ends, it buckles from the stress induced due to the temperature change as shown in fig5.2.

Figure 5.2: Wire segment bound on both sides

To measure this stress induced due to the temperature change, one end of the same wire is made free and is subjected to the same temperature change ΔT. This elongates the wire by a length of Δl. The wire is then pushed from the free side to till it is reduced to its original length l with the force P as shown in fig 5.3

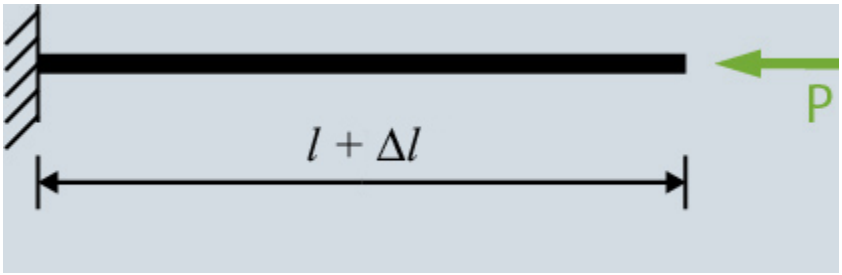

Figure 5.3: Setup to measure temperature effect of stress

Now the amount of stress, f, in the wire due to the force P is given by

$$f = \frac{P}{A} \tag{5.5}$$

Where A is the cross sectional area of the wire. We know that the modulus of elasticity E is given by the following equation

$$E = \frac{f}{\varepsilon} \tag{5.6}$$

Where is the strain in the wire which is given by the equation

$$\varepsilon = \frac{\Delta l}{l} \tag{5.7}$$

Substituting equation (5.7) in equation (5.6) :

$$E = \frac{f}{\varepsilon} = \frac{f}{\frac{\Delta l}{l}} = \frac{f.l}{\Delta l} \tag{5.8}$$

Substituting equation (5.8) in equation (5.4):

$$E = \frac{f.l}{\alpha.\Delta T.l} = \frac{f}{\alpha.\Delta T} \tag{5.9}$$

And we end up with the final equation

$$f = E\alpha\Delta T \tag{5.10}$$

This equation gives the stress in the wires due to the increase in temperature. This equation is the basis of the equation that was used in this thesis to establish the relationship between the temperature change and maximum hoop stress developed within the steam header section. The following equation was assumed to

$$\sigma_h = E\ K\ \alpha\ \left(1 - \frac{\theta}{180}\right)\ \Delta T_{md}\ z \tag{5.11}$$

Where σ_h is the maximum hoop stress developed in the header during the cycle, *K* stress concentration factor, *E* is the modulus of elasticity, α is the coefficient of thermal expansion, θ is the angle between the side tube penetration and the yz plane, ΔT_{md} is the maximum temperature difference in the steam header during the operating cycle and z is the multiplication factor that captures the evolution of both σ_h and ΔT_{md}. The relationship between both the maximum hoop stress and temperature difference and their evolution through increasing values of θ is studied by analyzing all the results from the 30 simulations.

5.2.1 Stress concentration factor

The stress concentration factor *K* is a dimensionless number that is the ration of the highest stress to the nominal stress in an object. For object with complex geometries, like a circular hole in an otherwise even straight and closed pipe, there exist regions of stresses in and around the complex geometry where the stresses are much higher than the average stress levels over the object in general. The steam header section that is analyzed in this thesis is also one such geometry where the stress levels found in and around the side tube penetration are much larger than the average stress levels produced in the header section in general. This is the primary reason why the meshes near the side tube penetrations were made finer to accurately capture the evolution of higher magnitude stresses. This has been verified many times by many experimental verifications involving circular pipes with holes.

The stress concentration factor is critical to this equation as it used to estimate the stress amplification in the vicinity of the complex geometry. It is experimentally verified that elliptical holes have lower stress concentration factors compared to circular ones [15], but since the side tube that are being dealt with in this simulations are circular, a stress concentration factor of $K = 3$ was chosen. This value was chosen as the average stress concentration factor of a circular hole on a pipe is 3 [3] and this has been verified experimentally.

5.2.2 Coefficient of thermal expansion

The coefficient of thermal expansion α was kept as a constant at $1.23 \times 10^{-5} {}^{\circ}\mathrm{C}^{-1}$ as all the models attained the maximum hoop stress and temperature difference values during the temperature range at which the coefficient of thermal expansion was $1.23 \times$

$10^{-5}°C^{-1}$. This value and the stress concentration factor were the only two factors that were kept constant through different models.

5.2.3 Side tube angle

The side tube angle is the angle between the centerline of the side tube and the YZ plane. The side tube angle ranges from 20 degrees to 30 degrees through 2.5 degree increments. The corresponding side tube angles are used in the equations representing the corresponding models.

5.2.4 Temperature difference

The maximum temperature difference ΔT_{md} is measured by finding out the maximum difference in temperatures between two nodes in the model that show the highest variation in temperature. From ABAQUS, the node with the maximum temperature throughout the cycle and the node with the minimum temperature throughout the cycle was identified. The temperature difference between these two nodes were tabulated and the maximum difference was chosen as ΔT_{md}. The temperature difference was chosen in this way because it was verified from the simulations that this value had a profound effect on how the hoop stresses evolved inside the model. This value was also unique to every model based on the varying parameters and these qualities were the main reason for this values to be chosen over the difference between the atmospheric temperature and the cycle temperature.

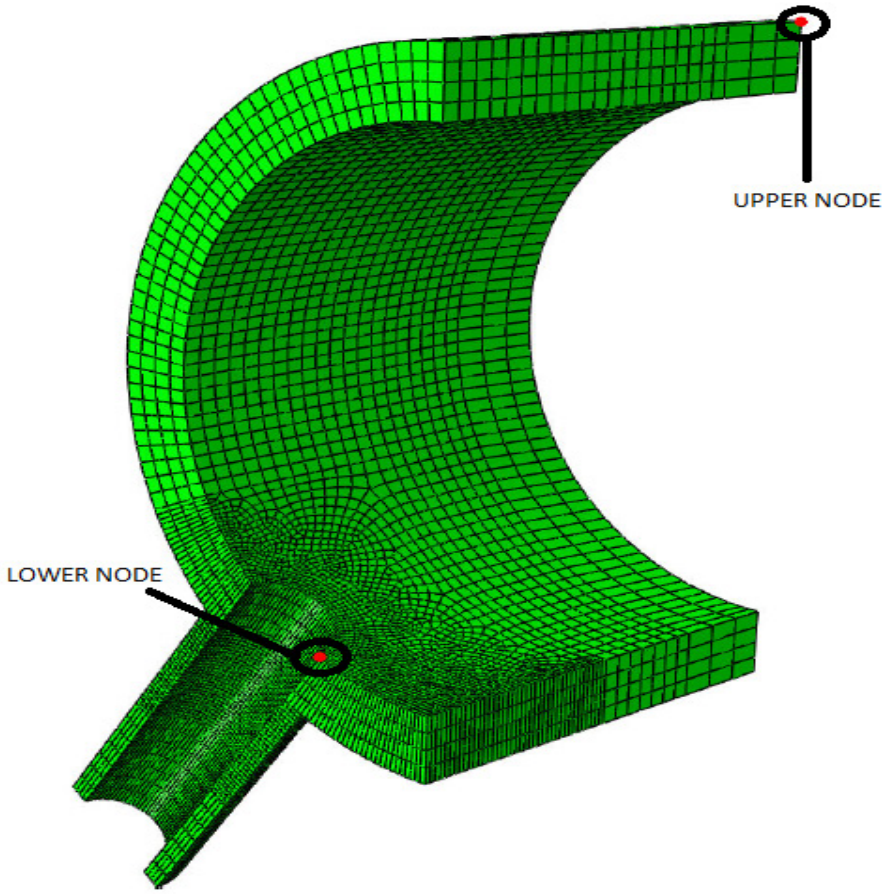

Figure 6.4: Location of nodes

The nodes shown in fig.6.4 are the location of the nodes at which the temperature difference was calculated. The temperature difference was obtained by subtracting the upper node temperature from the lower node temperature. For all the 30 models, the node location of highest temperature and lowest temperature remained the same.

5.2.5 Modulus of elasticity

The modulus of elasticity was also prescribed as a temperature dependent property. This meant that to verify the equation, the modulus of elasticity at the temperature during which the maximum hoop stress was attained needed to be used. All the models used

attained their maximum hoop stress at two different temperatures and hence the corresponding two values of modulus of elasticity were used. The elasticity modulus used in the equation

CHAPTER 6: RESULTS

The primary objective is to conduct a detailed hoop stress analysis of the models and finding out the best physical parameters that produce the least amount of circumferential stresses on the header segment. The hoop stresses were extracted from the model by prescribing a cylindrical coordinate system. In the result module, a cyndrical coordinate system was created. The coordinate system was created by identifying three reverence nodes on the arc of a circle along the circumference of the main header section. Setting this coordinate system as the main coordinate system for the results, the force along 2,2 direction represents the hoop stress. The cylindrical co-ordinate system used is displayed in fig. 6.1

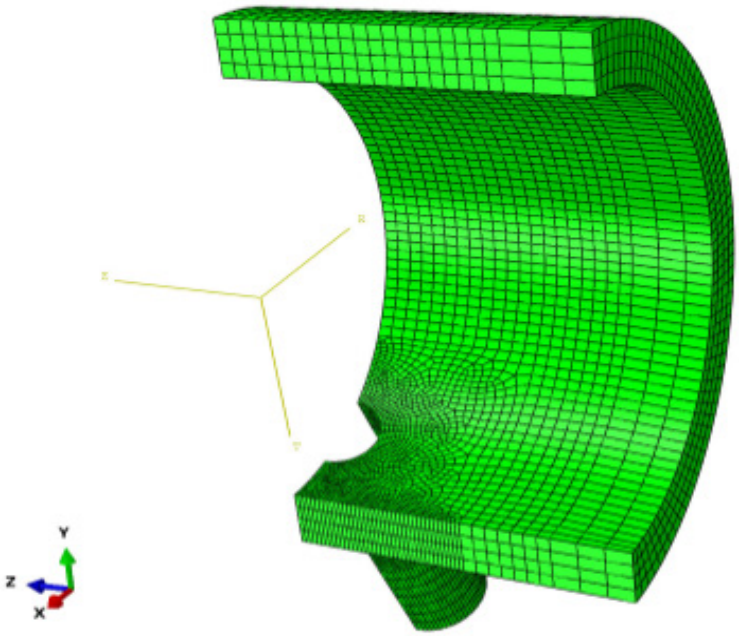

Figure 6.1: Prescribed cylindrical co-ordinate system

This data is then analyzed to find the location of the node at which the maximum hoop stress value occurs. The hoop stress history of this particular node is extracted and stored in the spreadsheet software for results processing. Microsoft Excel was used as the default software to process results and also to plot the various relationship curves.

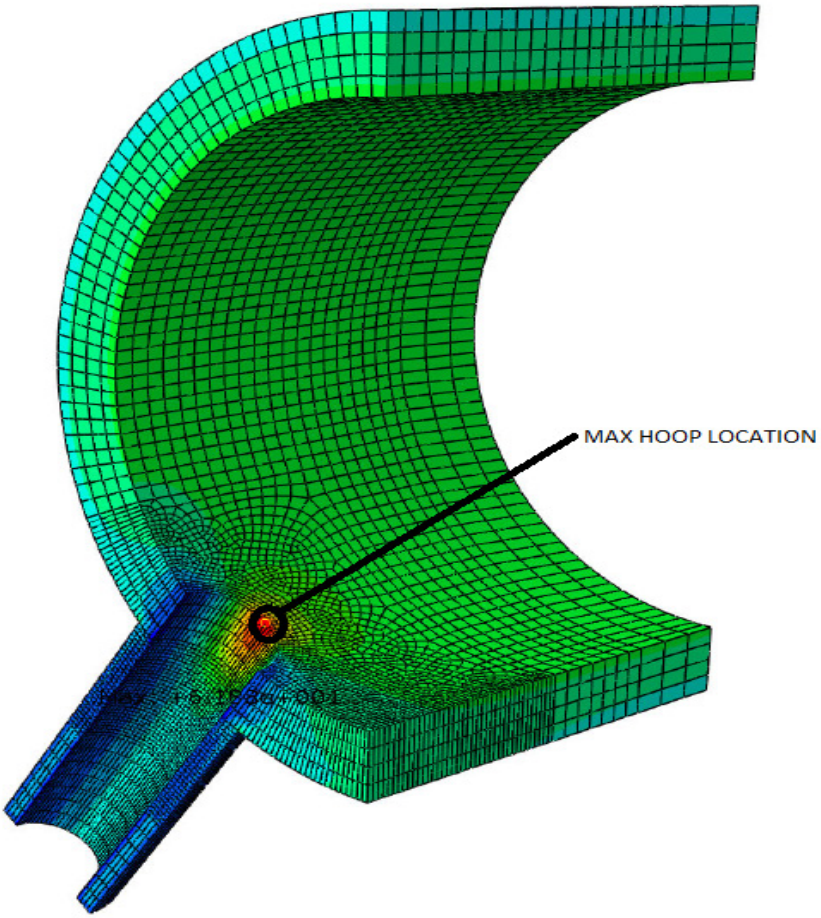

Figure 6.2: Location of the node exhibiting maximum hoop stress

The fig.6.2 shows the node at which the maximum hoop stress occurs. This node was chosen to analyze the hoop stress history through the entire time period. The temperature difference between the nodes shown in the last chapter was also extracted from ABAQUS. Almost all the results extracted from the .odb files were exported to excel to facilitate easy result processing. Throughout this thesis, all the plots were developed using MS Excel by tabulating the corresponding stress and temperature difference values.

6.1 Stress Results

The extracted circumferential stress values were tabulate against their respective time intervals. These stress values were then sorted using the two primary physical parameters which were of interest , the side tube angle θ and the internal and external diameters of the main header segment. The fig 6.3 is a plot of the circumferential stresses of all the models with θ = 20 degrees.

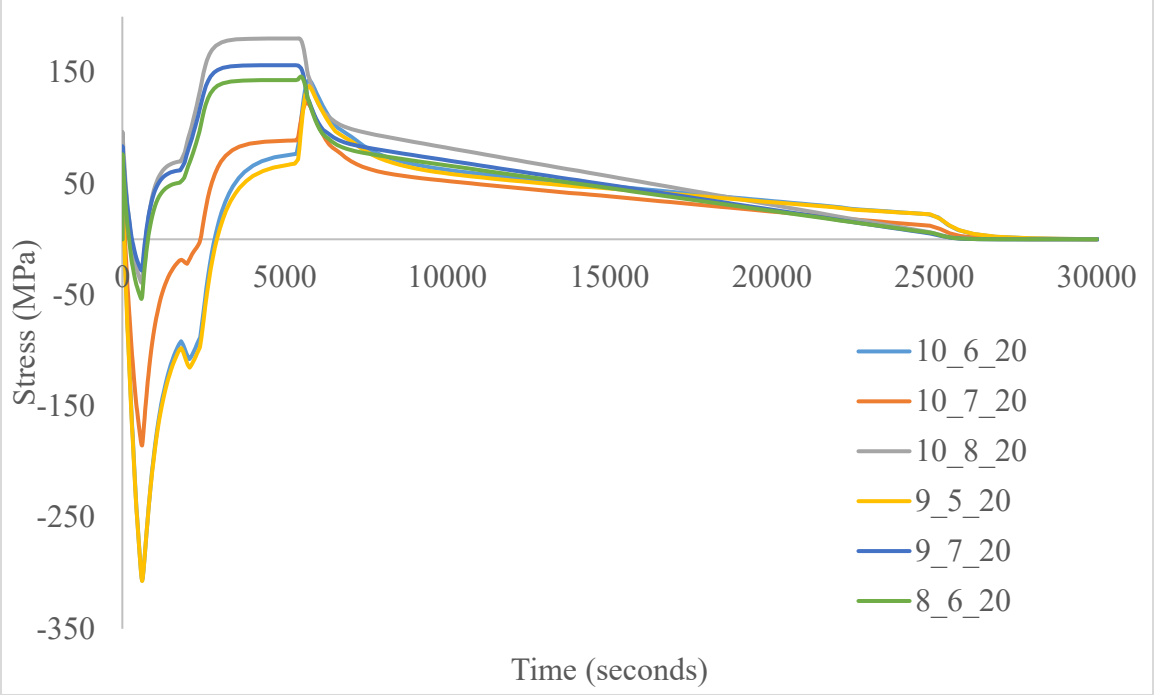

Figure 6.3: Stress (MPa) vs Time (seconds) for θ = 20 for all models.

The initial observation is that there are three distinct bands of similar that exhibit similar stress maps. It is not surprising that the models with same wall thickness exhibit similar properties as it was expected. The models with wall thickness of 2 inches have similar properties for similar angles. For example, the results of a model with external diameter 9 inches and internal diameter of 7 inches and side tube angle 25 degrees is similar to that of a model with external diameter 10 inches and internal diameter 8 inches and side

tube angle 25 degrees. The same phenomenon is observed in materials with models of 1 inch wall thickness and similar angles. From the result curves it is seen that the models with lesser wall thickness have their maximum hoop stresses in tension whereas the models with thickness of 1.5 inches and 2 inches both have their maximum hoop stresses in compression. This effect could be attributes to the extra material present in the thicker models. This presence of extra materials mean that the temperature difference between the outer wall and the inner wall is much greater than their thinner counterparts. The fig 6.4 is a plot of the temperature difference between the two nodes specified in the last chapter.

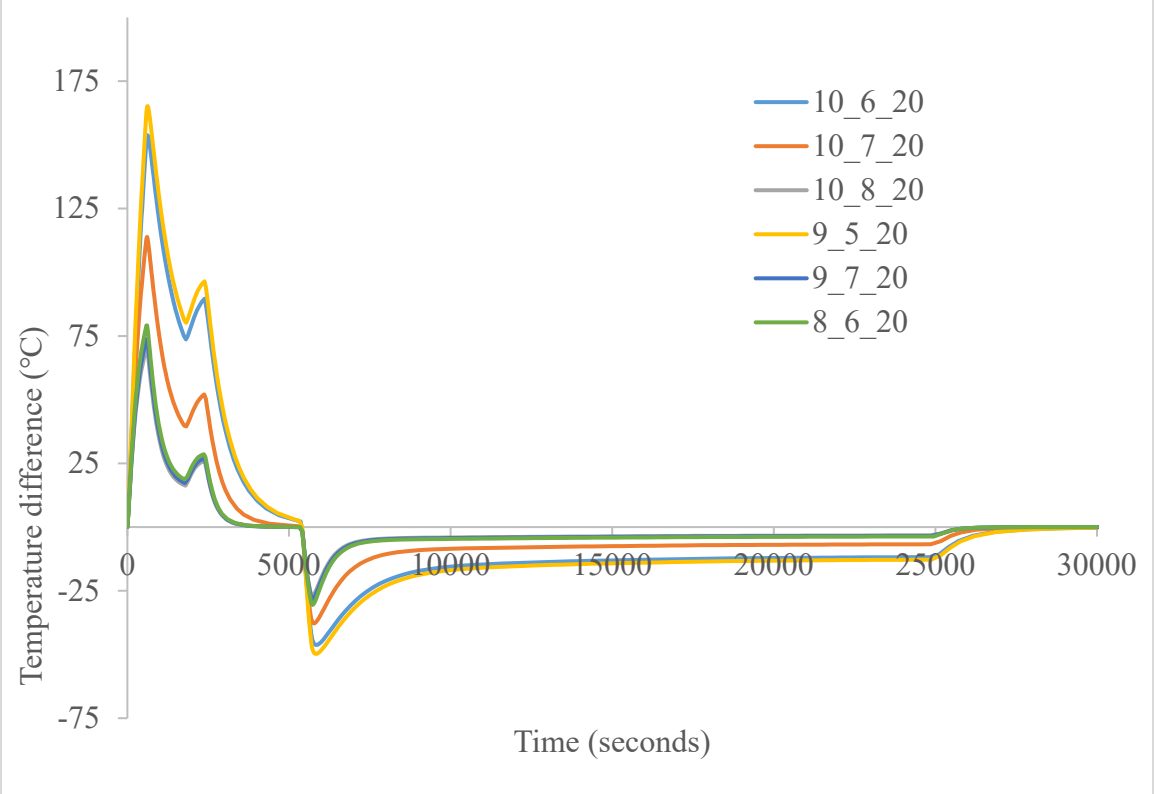

Figure 6.4: Temperature difference (°C) vs Time (seconds) for θ = 20 for all models.

The plots confirm that the header sections with a wall thickness 1.5 inches and above have a significantly higher temperature difference compared to that of the one's with

wall thickness of 1 inch. The maximum temperature difference value belongs to the mode 9_5_20 with a value of about 160 ℃ compared to the around 75℃ for 9_7_20 and 8_6_20.

It is observed that models with similar thickness and side tube angles have similar temperature difference profiles over the entire duration of the simulation.

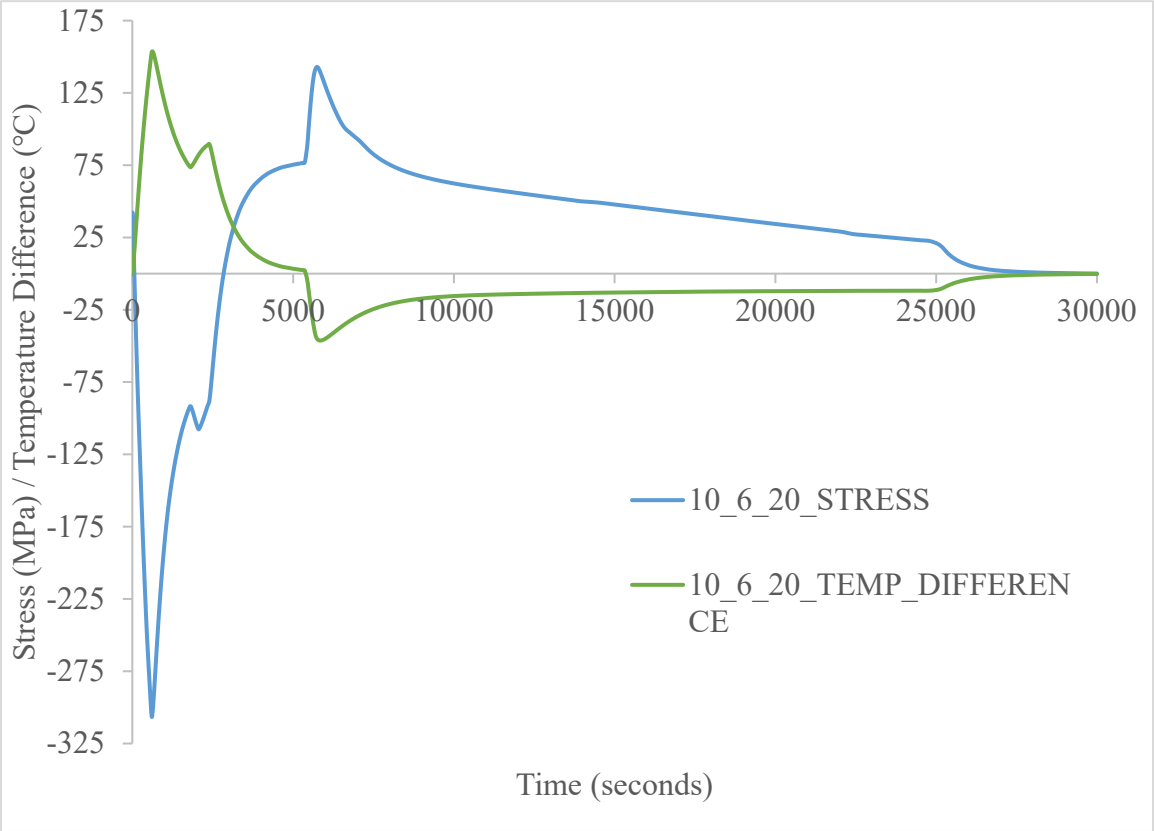

Figure 6.5: Stress (MPa) / Temperature Difference (℃) vs Time (seconds) for θ = 20, E.D = 10 inches, ID = 6 inches

The fig 6.5 is a plot of both temperature difference and the circumferential stress for the model 10_6_20. The model has an external diameter of 10 inches and internal diameter of 6 inches with a stub angle θ = 20 degrees. The wall thickness is 2 inches and as predicted earlier, the maximum circumferential stress occurs in compression when the value of the temperature difference is at the maximum value within the model. The stress values range at around 310 MPa when the temperature difference is around a max of 160

°C. The following fig 6.6 is a plot of one of the thinner header models, 10_8_20. Some crucial inferences can be observed by studying the difference between these two plots. Here the maximum circumferential stress occurs when the initial temperature difference spike slowly attains an equilibrium condition.

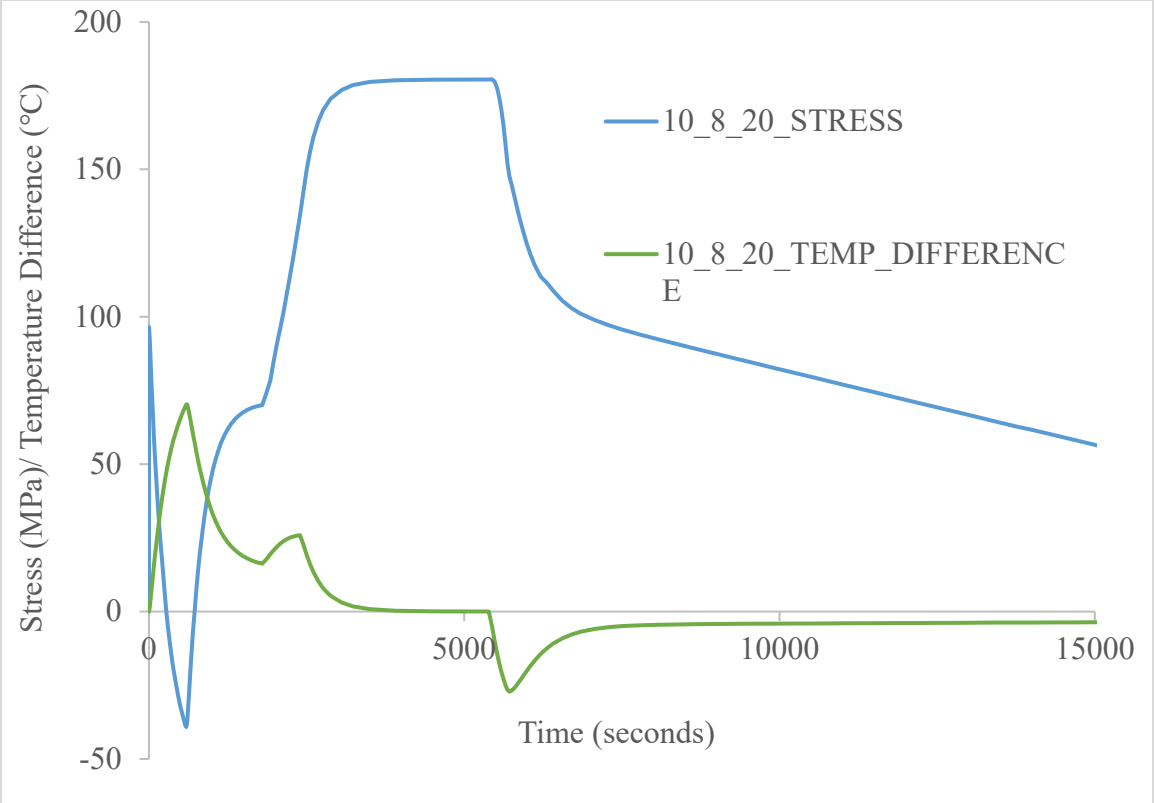

Figure 6.6: Stress (MPa) / Temperature Difference (°C) vs Time (seconds) for θ = 20, E.D = 10 inches, ID = 8 inches

On comparing both the temperature differences, it is observed that the thinner models attain initial thermal equilibrium around the 3000 seconds whereas the thicker models reach thermal equilibrium around the 5500 seconds. This delayed onset of thermal equilibrium can be directly attributed to the wall thickness material that needs to be heated before the temperature difference is resolved. The initial uneven temperature distribution in the thick headers results in the expansion of the inner surface material due to direct

surface contact with the heated steam. The layers below the inner surface initially resist the expansion by exerting an opposing force that shows up as the compressive circumferential forces in thicker models, but as time progresses and the inner layers are heated, they too expand with the inner layer and the resultant compression's magnitude goes down and switches to tension. Supporting this theory, the thin walled headers also show a small compressive circumferential stress during the initial heating but since the thermal equilibrium is attained much sooner, the maximum stress is in tension.

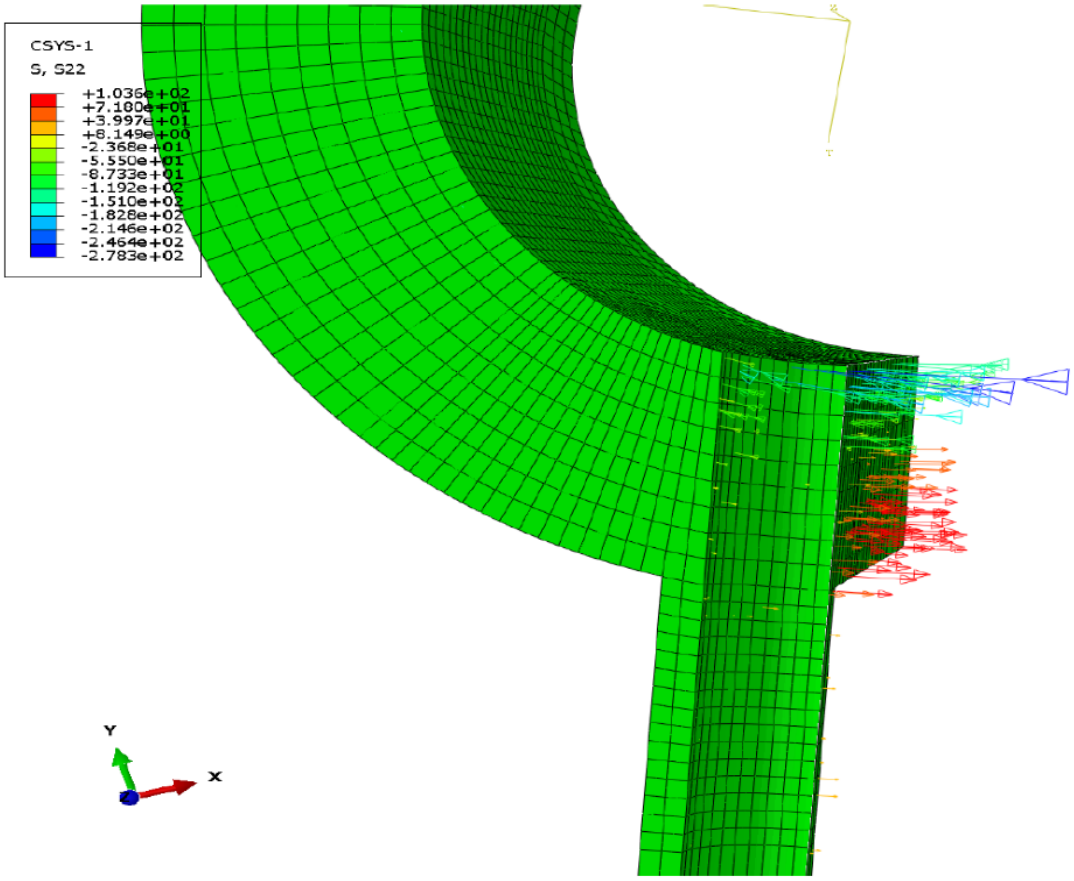

Figure 6.7: Circumferential stress directions of model 10_6_20 at increment number 105, when the temperature difference is close to minimum.

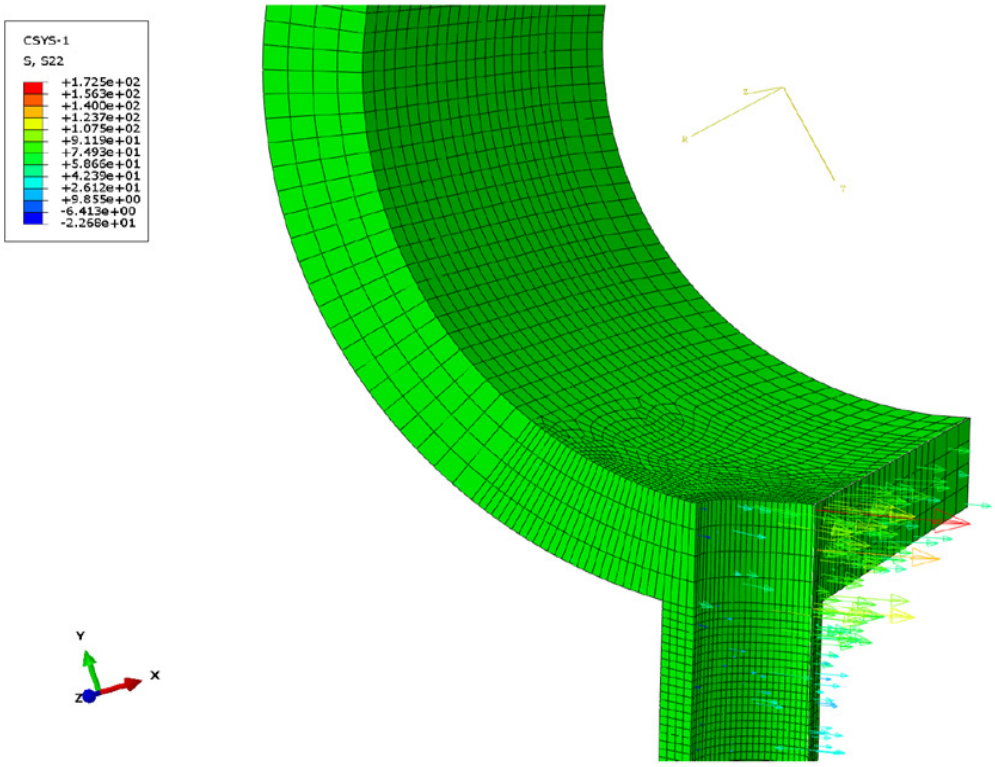

Figure 6.8: Circumferential stress directions in a cut of the model 10_6_20 at increment number 47, the frame of maximum tension.

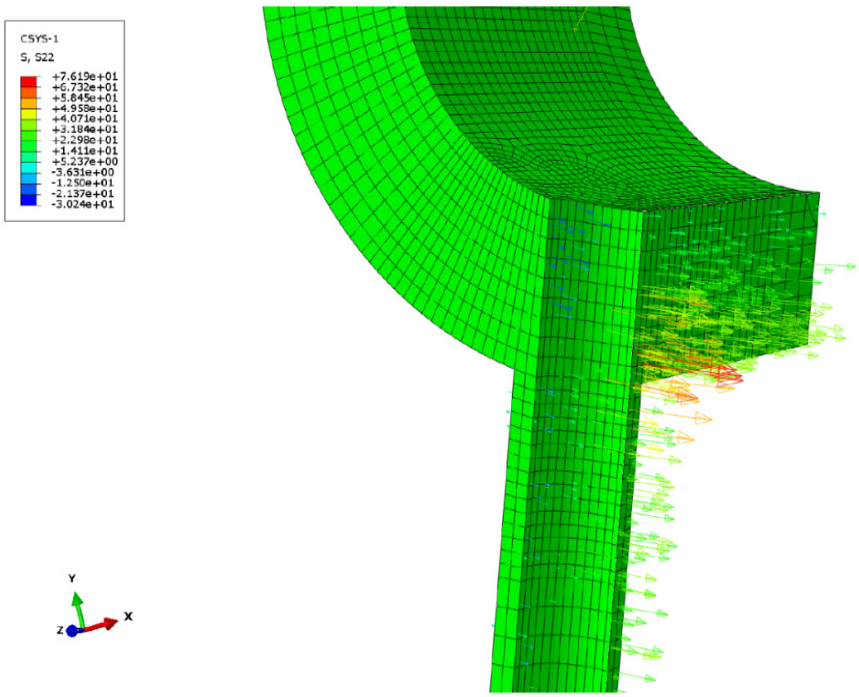

Figure 6.9: Circumferential stress directions in a cut of the model 10_8_20 at increment number 100, the increment at which maximum hoop stress occurs in this model.

The maximum circumferential stress in thinner models correspond to the maximum internal pressure of the steam and come down in magnitude only when the internal pressure goes down.

The models in fig 6.7 through fig 6.9 show the direction of the circumferential stresses confirming the theory about temperature and stress behavior of both the thick and thin models. These plots are important such that they show that the temperature prescribed in the operating cycle is more important in predicting the type and magnitude of the stress in the models during operation.

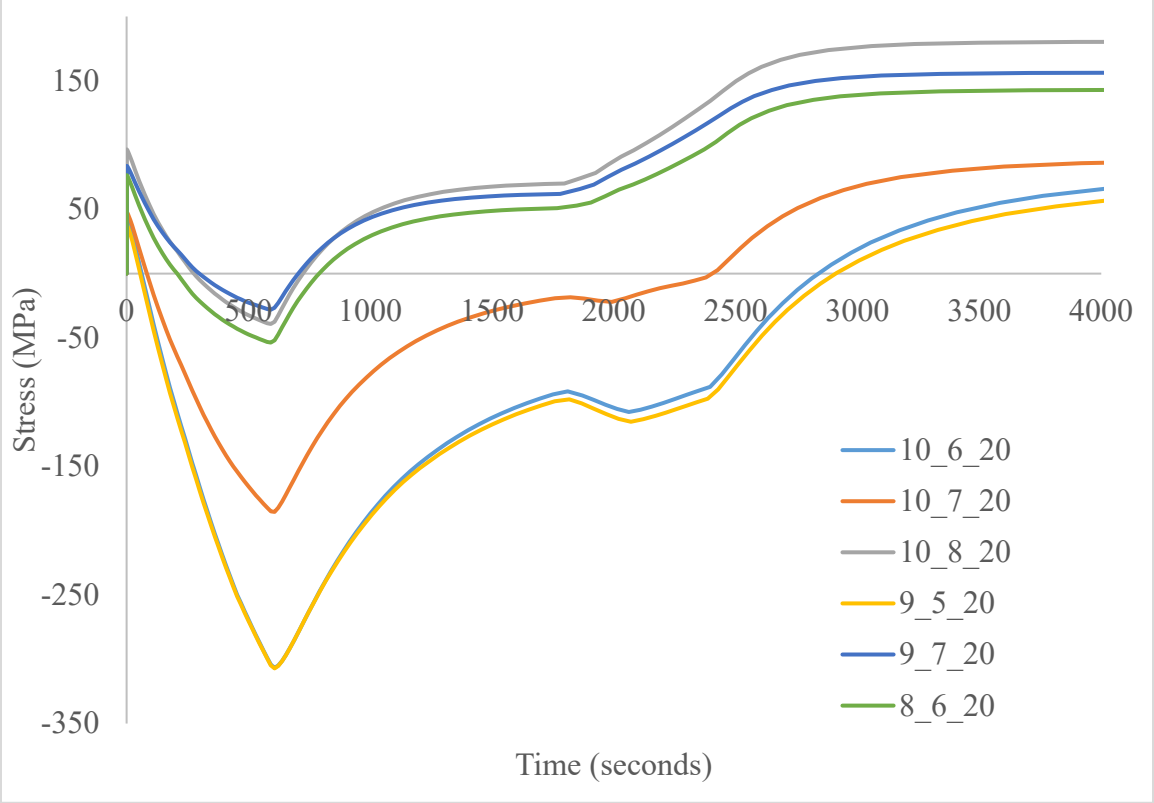

Figure 6.10: Stress (MPa) vs Time (seconds) for all models with θ = 20 for the time 0 to 4000 seconds.

Figure 6.10 is a magnification of the first 4000 seconds of the plot in fig 6.3. As explained already, the thicker models start off with a higher compressive circumferential stress and the thinner models with a lower value of the same. The models of similar thicknesses follow similar paths in the plot. There is a pronounced difference shown in the tensile circumferential stresses in the thinner models from 2000 seconds to 4000 seconds. The models with the larger surface area show a higher value of tensile stresses, unlike the models of thickness wall thickness 2 inches where the maximum compressive stress is almost identical and the difference is negligible. This would suggest the smaller models with the wall thickness of 1 inch have a lower value of maximum hoop stresses. The difference between them is of the order of around 40 MPa and this is a significant difference.

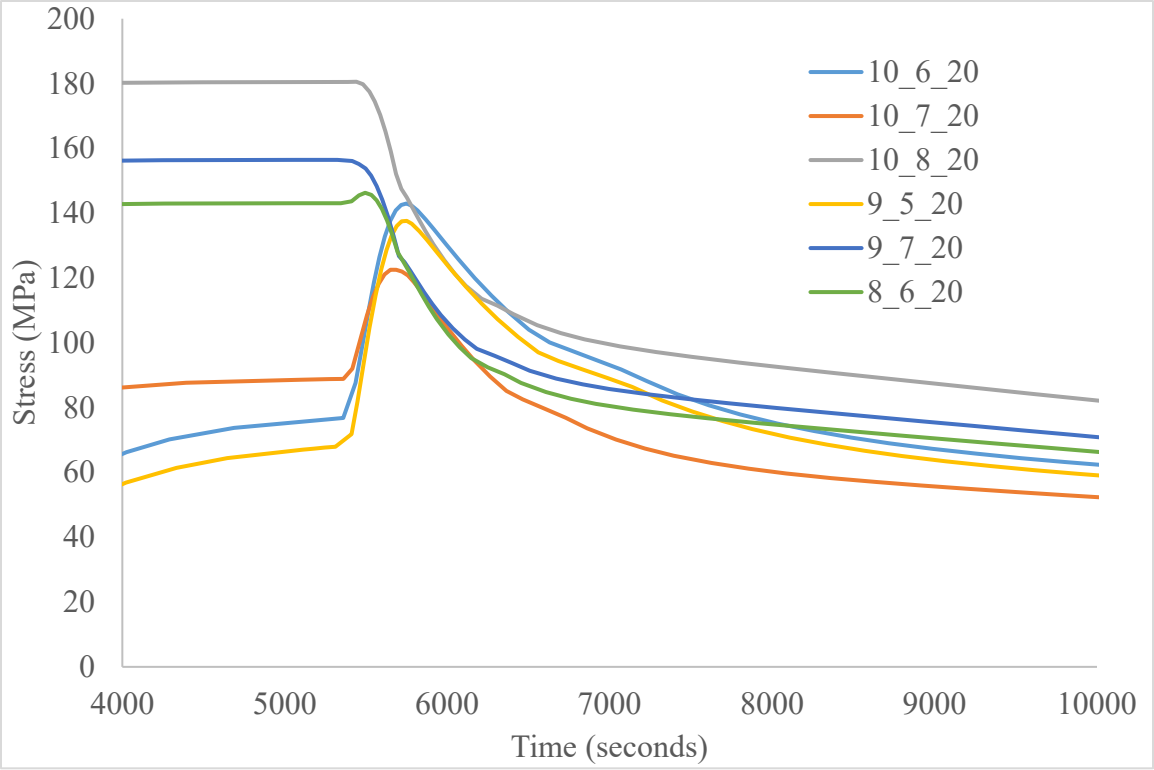

Figure 6.11: Stress (MPa) vs Time (seconds) for all models with θ = 20 for the time 4000 to 10000 seconds.

The fig 6.11 shows the same plot for a tie period for 4000 seconds to 10000 seconds. The small spikes in tensile stresses of the models with wall thickness above 1.5 inch represents the rapid rise as soon a thermal equilibrium is reached around the 5000 seconds mark with the internal pressure at the maximum value of 14 MPa. This does not last long due to the operation cycle prescribed. The internal pressure value drops, thereby reducing the tensile circumferential stresses in the models with thicker walls.

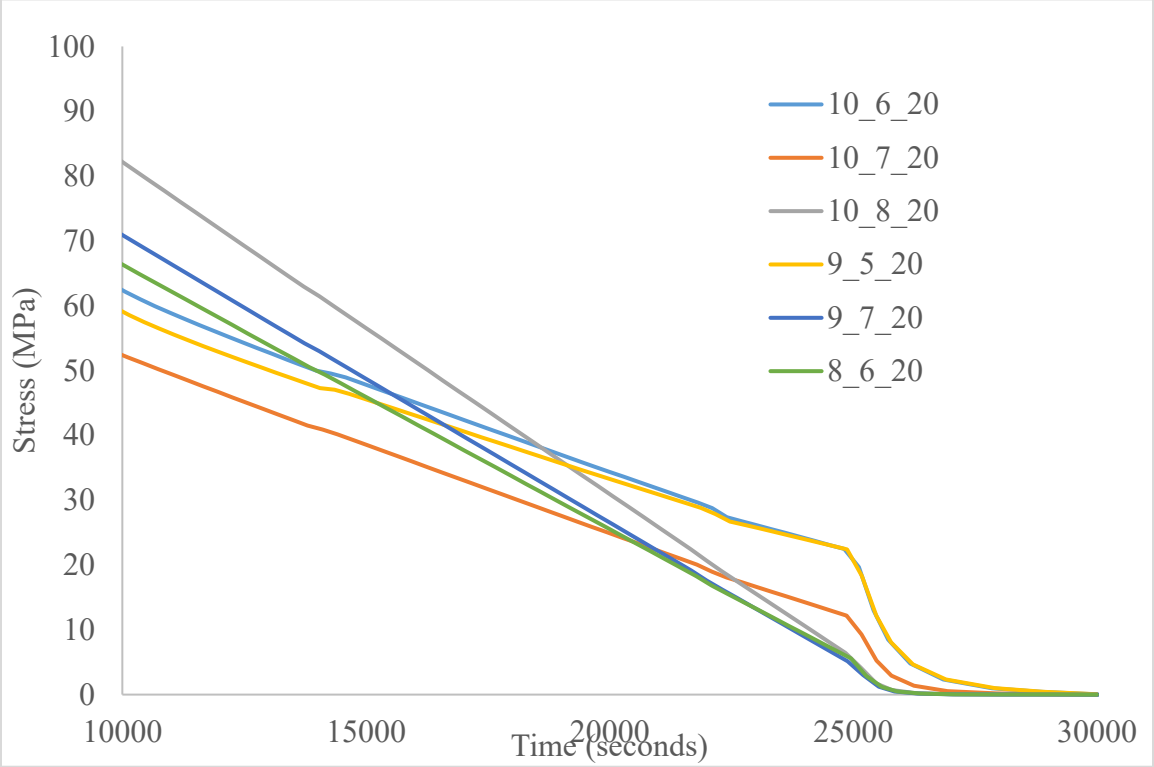

Figure 6.12: Stress (MPa) vs Time (seconds) for all models with θ = 20 for the time 10000 to 30000 seconds.

At the end of the cycle, the thinner models again show much desirable properties compared to the thicker models in attaining thermal equilibrium much sooner. This again can be attributed to the presence of all the extra material that needs to dissipate heat to the surroundings in the thicker models. The following plots of the models with increasing side tube angle θ.

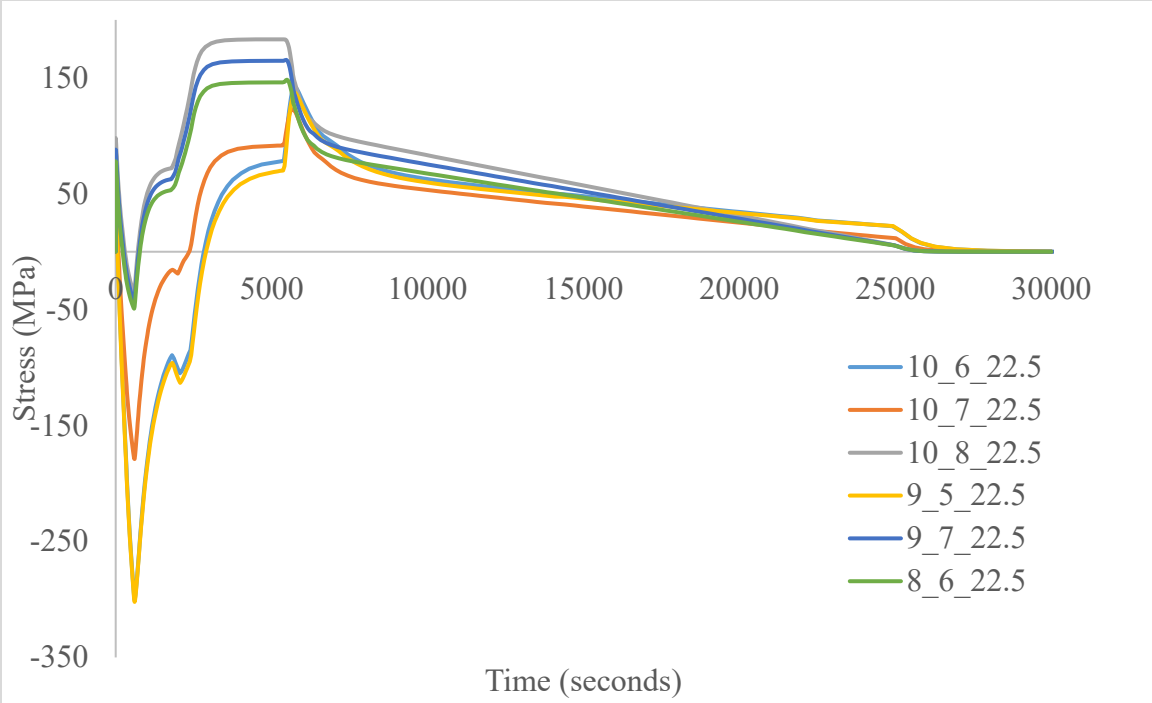

Figure 6.13: Stress (MPa) vs Time (seconds) for all models with θ = 22.5 for the cycle time 0 to 30000 seconds.

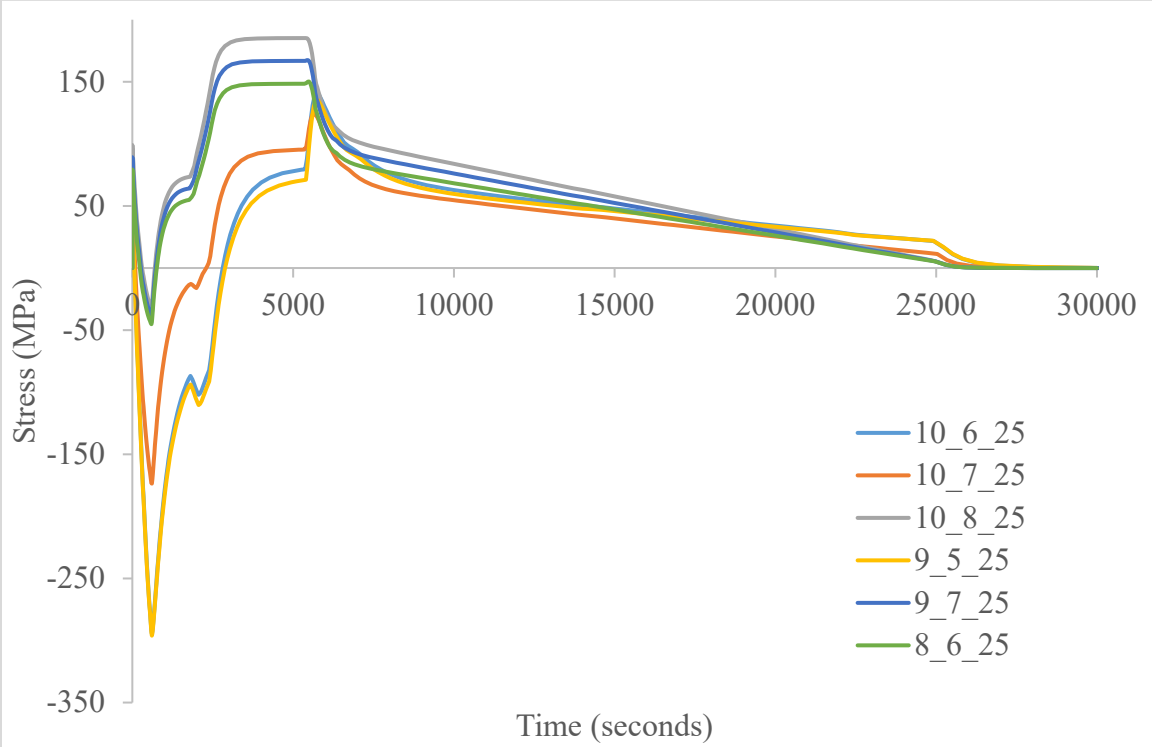

Figure 6.14: Stress (MPa) vs Time (seconds) for all models with θ = 25 for the cycle time 0 to 30000 seconds.

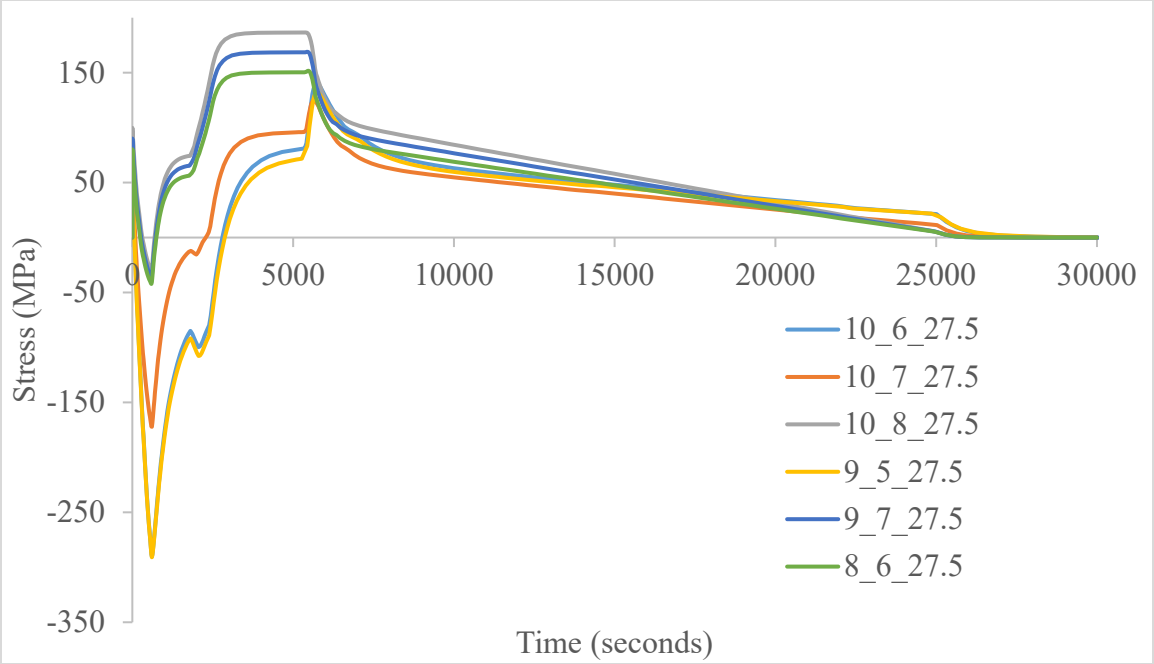

Figure 6.15: Stress (MPa) vs Time (seconds) for all models with θ = 27.5 for the time period 0 to 30000 seconds.

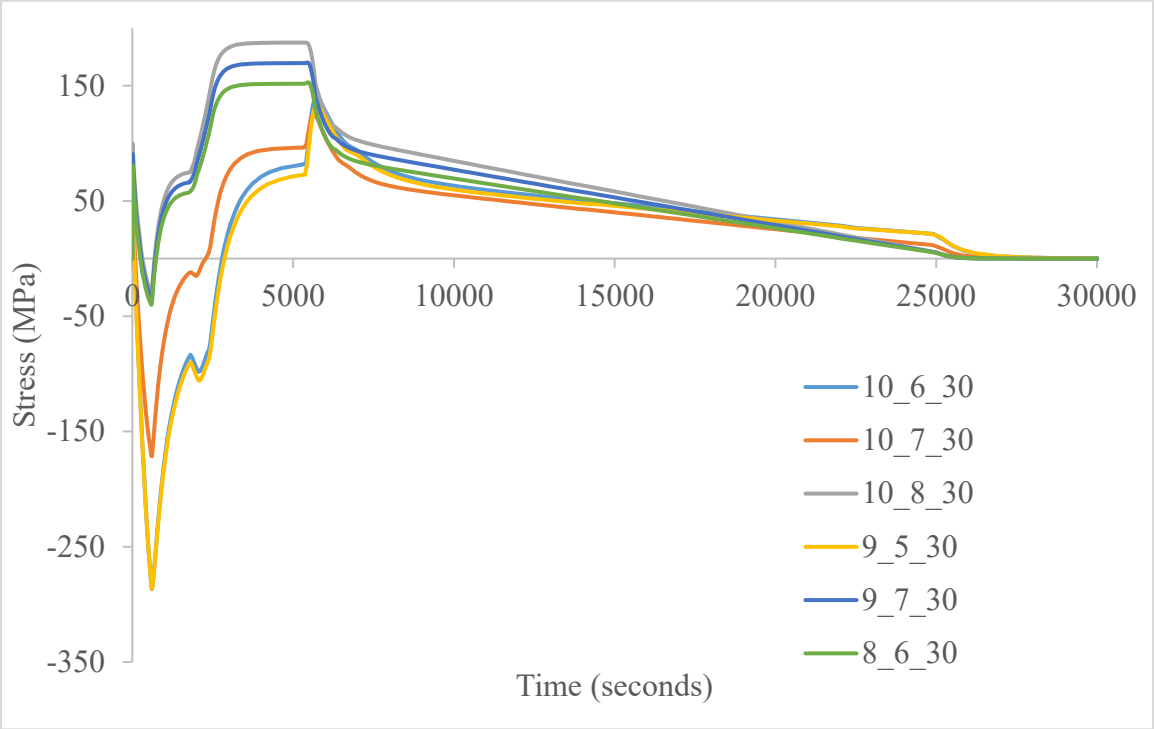

Figure 6.16: Stress (MPa) vs Time (seconds) for all models with θ = 30 for the time period 0 to 30000 seconds.

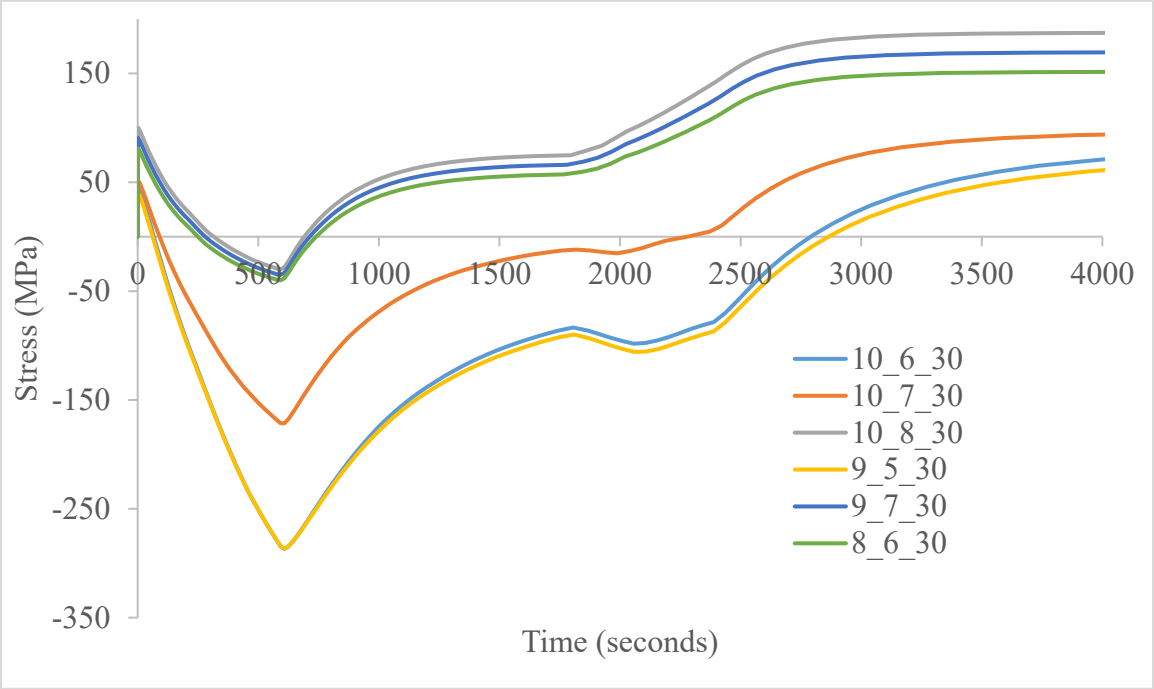

Figure 6.17: Stress (MPa) vs Time (seconds) for all models with θ =30 for the time period 0 to 4000 seconds

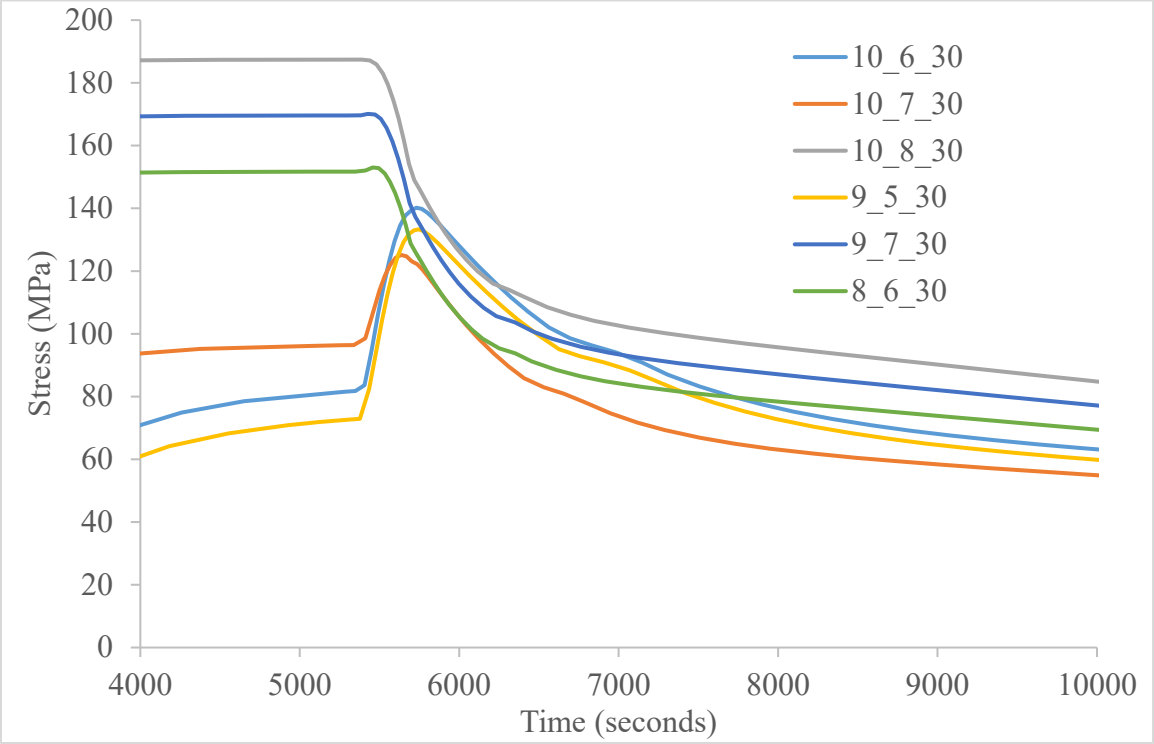

Figure 6.18: Stress (MPa) vs Time (seconds) for all models with θ = 30 for the time period 4000 to 10000 seconds.

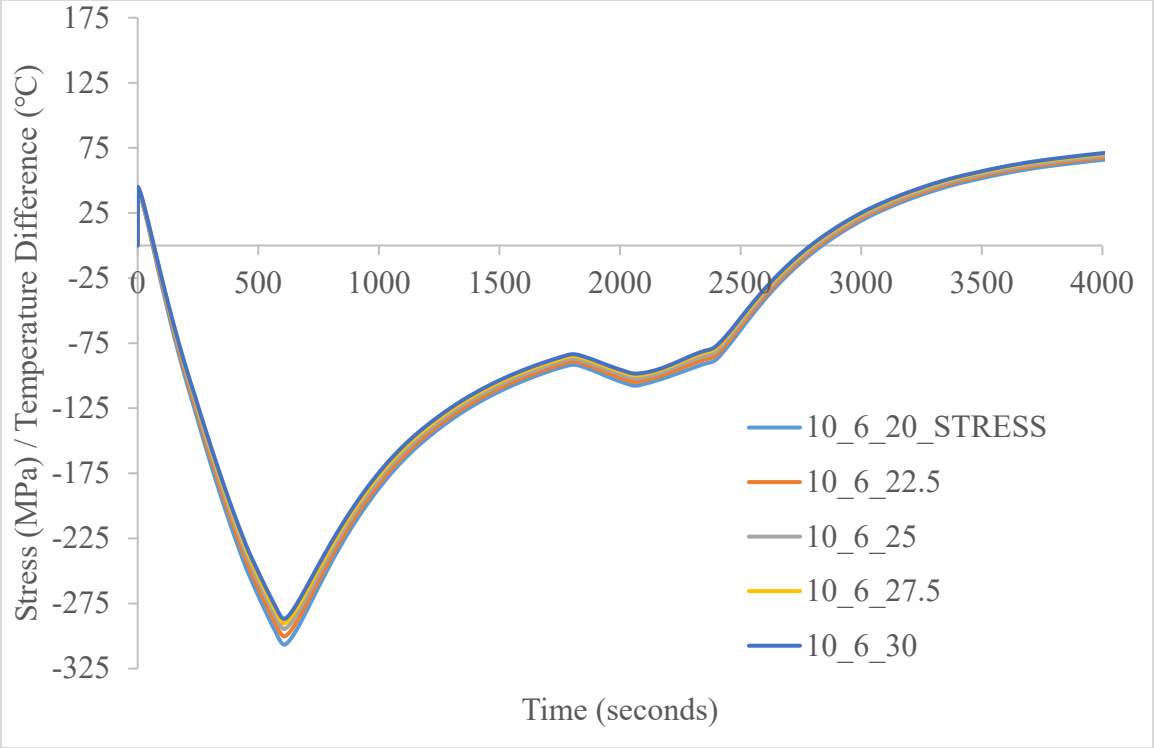

Figure 6.19: Stress (MPa) vs Time (seconds) for all models with O.D = 10 inches, I.D = 6 inches through all values of θ for the time period 4000 to 10000 seconds.

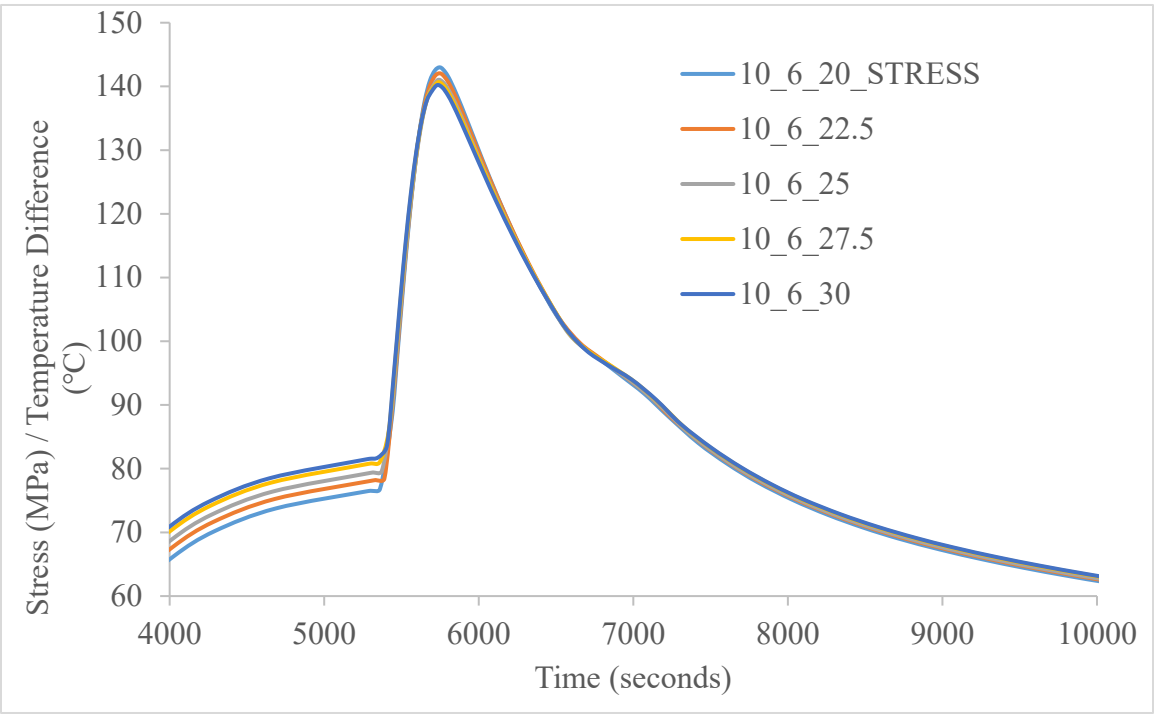

Figure 6.20: Stress (MPa) vs Time (seconds) for all models with O.D = 10 inches, I.D = 6 inches through all values of θ for the time period 4000 to 10000 seconds.

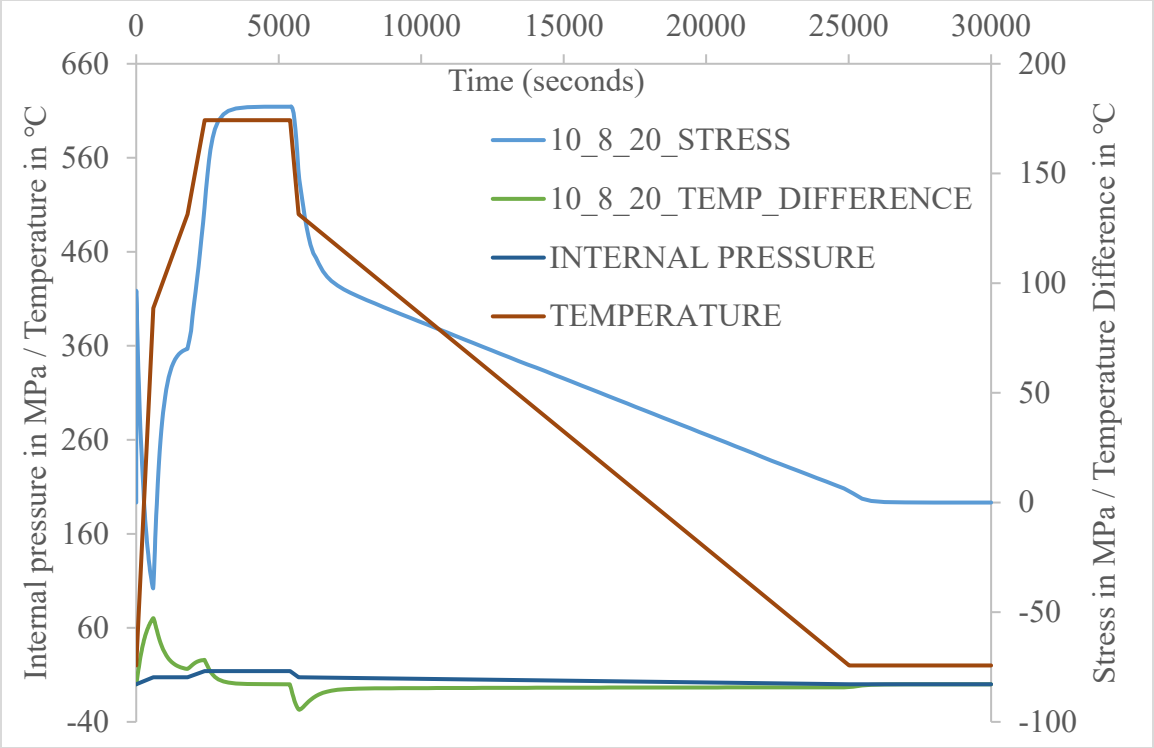

Fig 6.21: Operating cycle parameters against hoop stress and temperature difference

The plots in fig 6.13 through 6.16 are plots of all the models with θ = 22.5º, 25º, 27.5º and 30º respectively. These plots show the general stress behavior of the models of varying annulus cross section and wall thickness for the same θ. From these plots it is inferred that with increase in θ, there is an decrease in general stress levels in both compression and tension. Fig 6.17 and 6.18 show a closer look at the plots for θ=30 degrees and it is observed that the compressive stresses are generally lower than the model with side tube angle 20 degrees, but the tensile stress behavior is slightly higher than that of the same models. Another important result here from all the above figures showing variation of stress for a fixed value of θ and varying inner and outer dimensions is that the stress is higher for models with a larger annulus cross section, even if they have the same thickness. From the plot in fig 6.16 the model 10_8_30 is found to exhibit higher stress values in

comparison with 8_6_30 even when the wall thickness is a constant at t = 1 inch. It can be inferred that for a constant value of θ and wall thickness, the model with the smallest cross sectional area of the annulus of the cylindrical header section would have the most favorable circumferential stress levels.

The fig 6.19 and 6.20 show the plots for a model with wall thickness t = 2 inches and it shows that the models with lower values of θ have higher values of compressive stresses compared to tensile stresses in thinner models with t = 1 inch. The fig 6.22 shows that the stress in tension shows a similar behavior where lesser values of θ has marginally higher values of tension. The fig 6.22 is a plot of the stresses for model 10_8_θ. Here the model with θ = 20 degrees shows marginally higher compression whereas in tension, the model with θ = 30 degrees show higher stress values. However, it is to be noted that the temperature difference shown in fig 6.23 and fig 6.24 show that both thicker and thinner models with θ = 20 degrees show a higher temperature difference which decreases with θ.

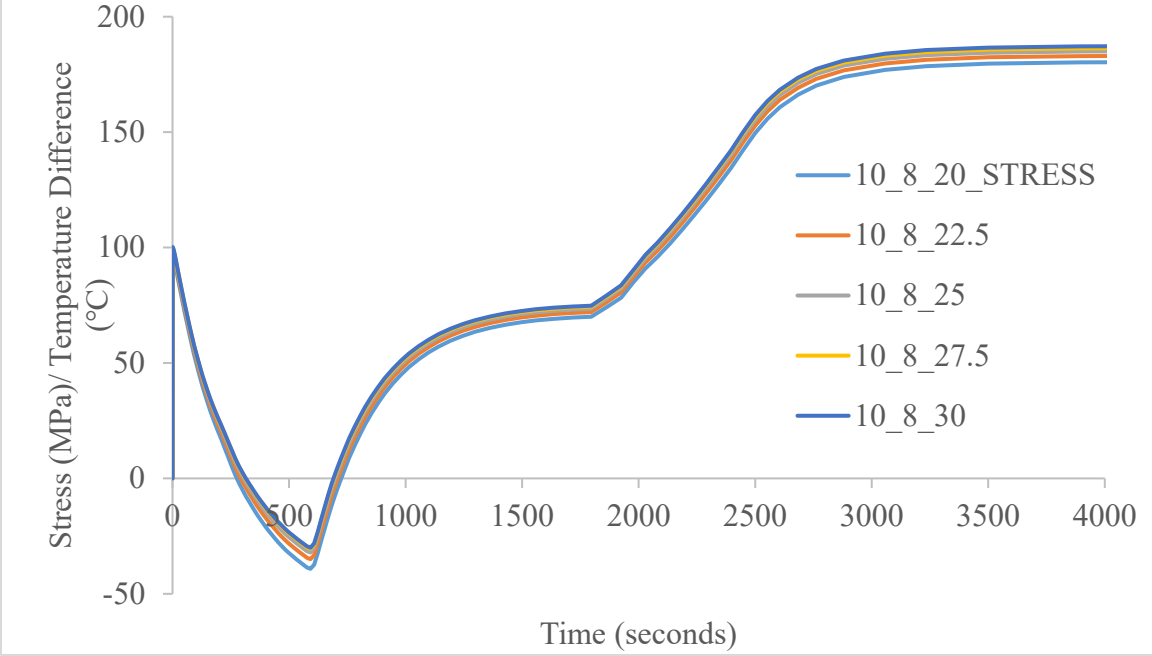

Figure 6.22: Stress (MPa) vs Time (seconds) for all models with O.D = 10 inches, I.D = 8 inches through all values of θ for the time period 0 to 4000 seconds.

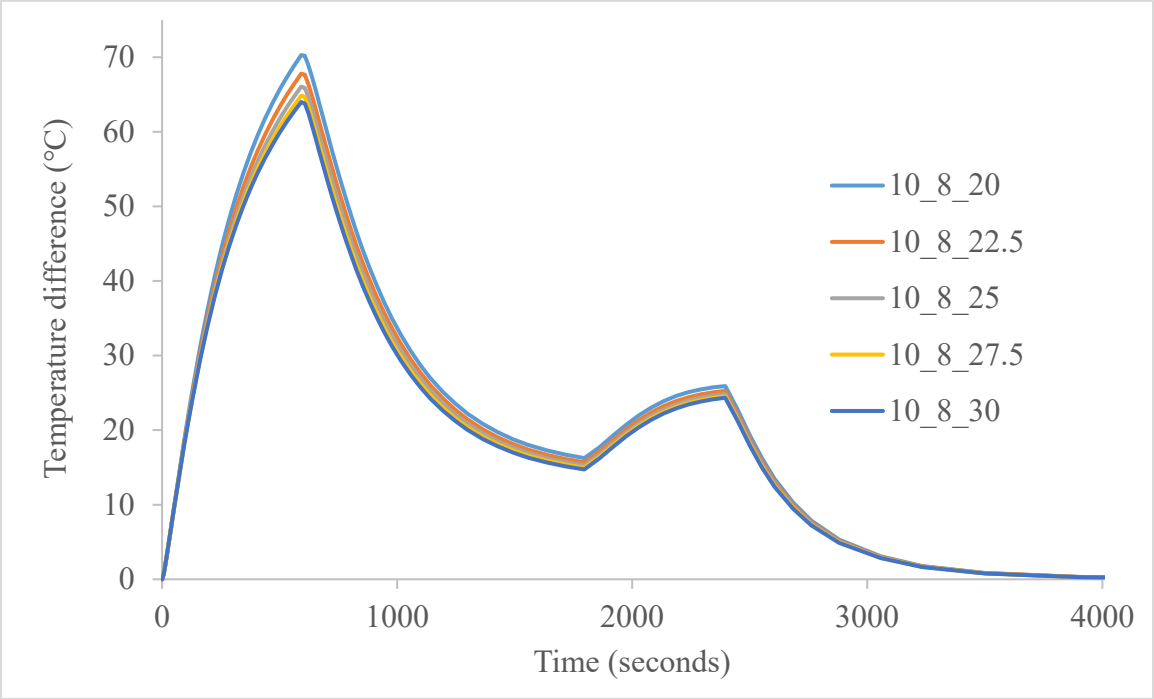

Figure 6.23: Temperature difference (°C) vs Time (seconds) for all models with O.D = 10 inches, I.D = 8 inches through all values of θ for the time period 0 to 4000 seconds.

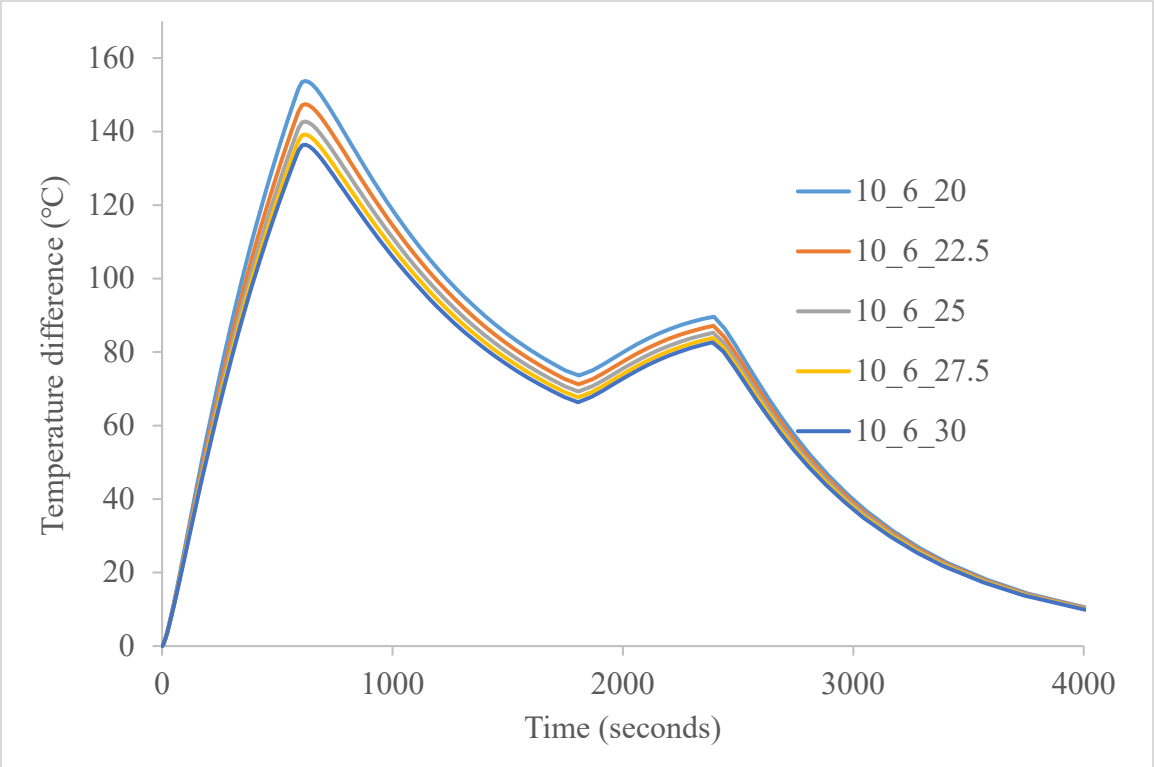

Figure 6.24: Temperature difference (°C) vs Time (seconds) for all models with O.D = 10 inches, I.D = 6 inches through all values of θ for the time period 0 to 4000 seconds.

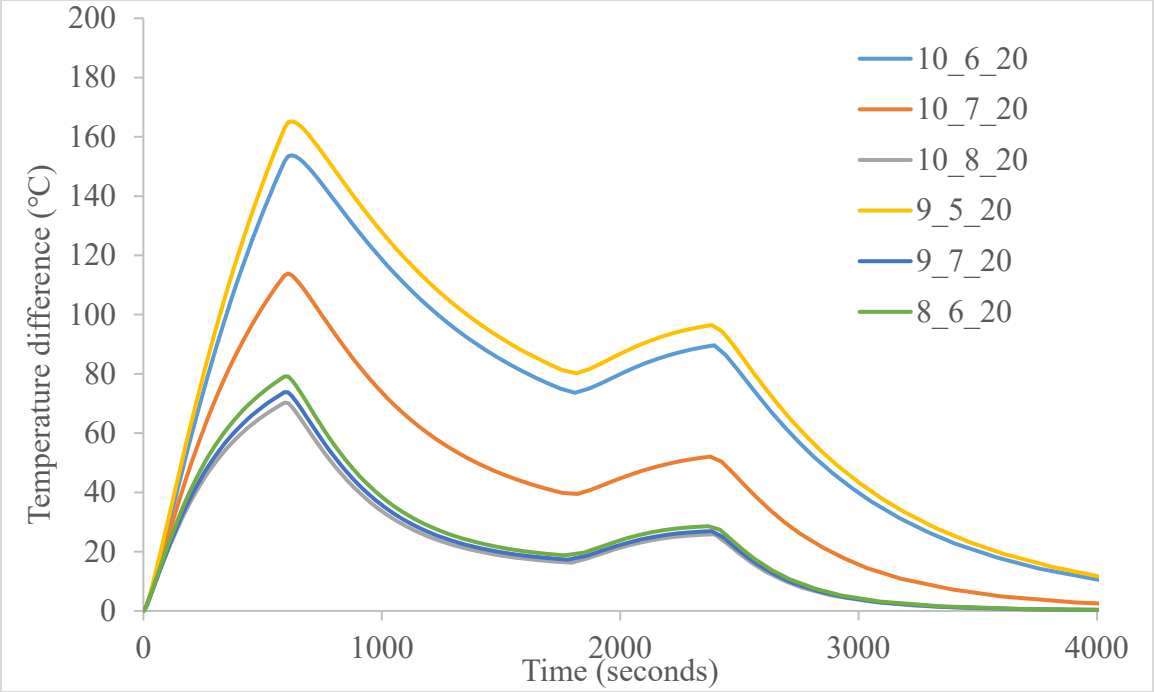

Figure 6.25: Temperature difference (°C) vs Time (seconds) for θ = 20 through all models for the time period 0 to 4000 seconds.

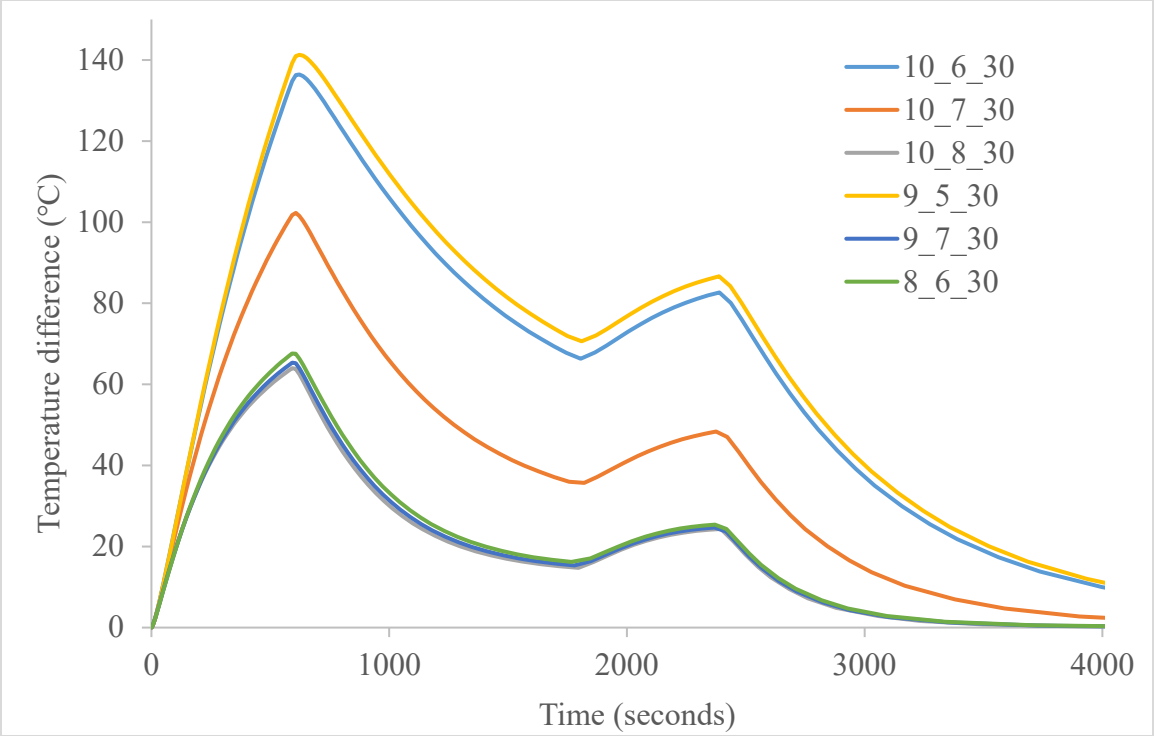

Figure 6.26: Temperature difference (°C) vs Time (seconds) for θ = 30 through all models for the time period 0 to 4000 seconds.

The following two fig 6.25 and fig 6.26 are the plots of temperature difference against time for a fixed value of θ and varying cross section areas. It is observed that the models with larger cross section area of the annulus for the same wall thickness has a lower temperature difference value.

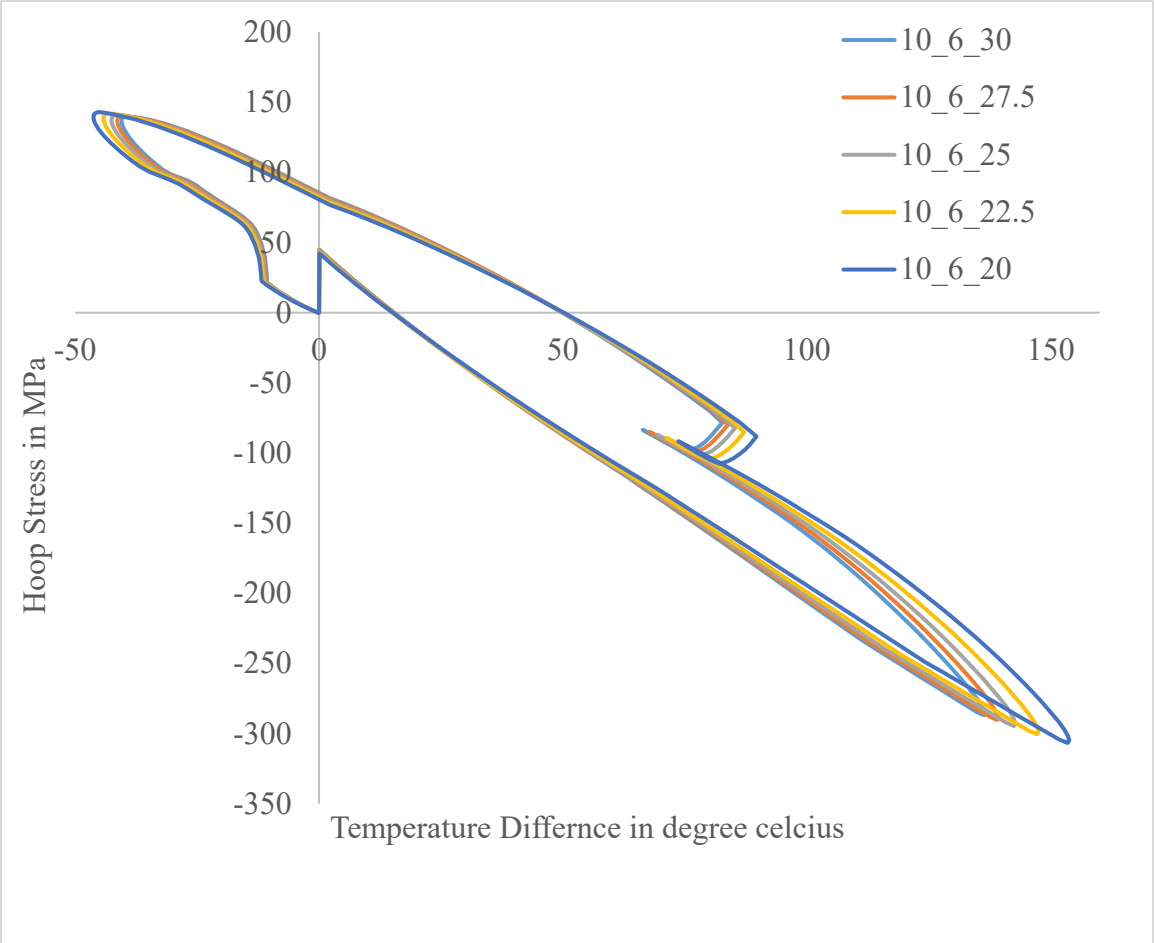

Figure 6.27: Stress (MPa) vs Temperature difference (°C) for the whole cycle for the model with O.D = 10 inches, I.D = 6 inches for all values of θ.

From fig 6.10 through 6.25, it is well established that the temperature difference of the thickest model with the least value of θ has the highest value whereas the model with the thinnest wall and highest θ value with the least area of cross section of the annulus has the lowest values for temperature difference. We have also established that with increasing

angles of θ, there is an decrease in the stress in both compression and tension for model with thickness 1.5 inches and above, and in compression for t = 1 inch. The unique behavior for tension in thinner header segments where stress increases with increase in θ can be attributed to them models with higher values of θ attaining thermal equilibrium much sooner than models with lower θ values. The following fig 6.28 and fig 6.29 are plots of the circumferential stresses of models with t = 2 inches and 1 inch respectively. Models of all θ values were plotted. In fig 6.26, the model 10_6_30 has the lowest values of compressive stresses at around 300 MPa and also the lowest values of temperature difference compared to 10_6_20, which has the maximum values for both. From this, it can be concluded that the model with the least plot area in this plot would be the best for overall performance and reduced thermal fatigue.

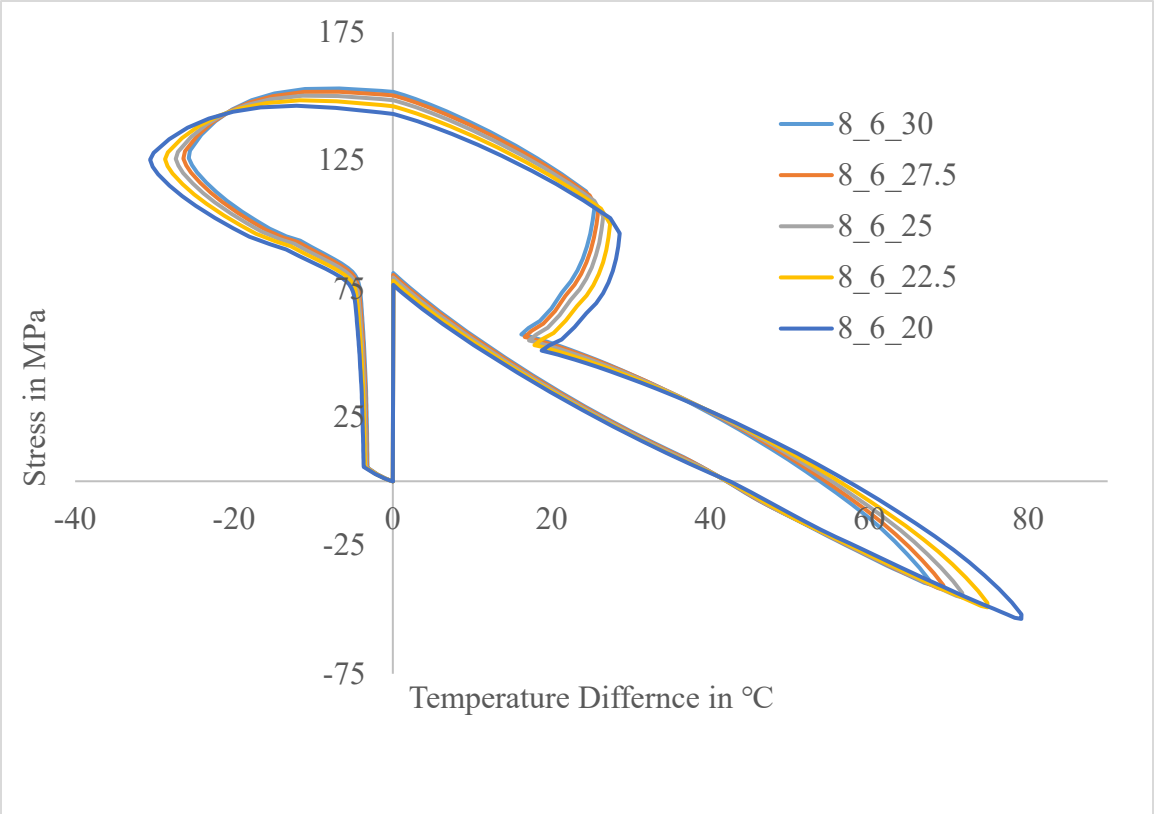

Figure 6.28: Stress (MPa) vs Temperature difference (°C) for the whole cycle for the model with O.D = 8 inches, I.D = 6 inches for all values of θ.

The fig 6.27 is slightly different in such a way that the stresses in tension are marginally higher for θ = 30 and as θ decreases, the value of stress also decreases, but this holds good only for maximum tension. The difference in stress between θ = 30 and θ = 20 is around the order of 10 to 15 MPa. In addition to that, during all other periods of the cycle, the stress values of the models with lower θ values are higher compared to the ones with higher θ values. The presence of more pronounced temperature difference for models with lower values of θ would result in a lower thermal fatigue life, which is not desired. So again, it is recommended to go with the model with the least plot are which would be 8_6_30. From all the results analyzed, it is evident that the side tube angle θ is a significant factor in deciding the overall temperature difference and stress levels in header segment. This could be explained by the complex geometries that arise when the value of θ is reduced. Due to the symmetric nature of the header segment, a lower value of θ would mean two complex geometries in an otherwise perfect cylindrical vessel are placed closed to each other. The stress concentration factor in such structures are higher compared to the structures with complex geometries placed further apart. The pronounced temperature difference and stress maps are direct result of this. Tables 7.1 through 7.6 displays the value of the maximum circumferential stress and the maximum temperature difference for all the simulated models.

Table 6.1: Stress and temperature difference for m model 10_6_θ

θ	Maximum Hoop stress(MPa)	Maximum Temperature difference (℃)
10_6_20	-306.674	153.454
22.5	-300.925	147.457
25	-294.586	142.735
27.5	-290.259	139.192
30	-286.858	136.425

Table 6.2: Stress and temperature difference for m model 9_5_θ

θ	Maximum Hoop stress(MPa)	Maximum Temperature difference (℃)
9_5_20	-307.08	165.237
22.5	-302.115	156.476
25	-296.108	150.049
27.5	-290.868	145.146
30	-286.555	141.283

Table 6.3: Stress and temperature difference for m model 10_8_θ

θ	Maximum Hoop stress(MPa)	Maximum Temperature difference (℃)
10_8_20	180.55	70.292
22.5	183.231	67.797
25	185.211	66.057
27.5	186.556	64.84
30	187.409	63.995

Table 6.4: Stress and temperature difference for m model 9_7_θ

θ	Maximum Hoop stress(MPa)	Maximum Temperature difference (℃)
9_7_20	156.438	73.811
22.5	165.517	70.584
25	167.449	68.258
27.5	169.004	66.561
30	170.1065	65.346

Table 6.5: Stress and temperature difference for m model 8_6_θ

θ	Maximum Hoop stress(MPa)	Maximum Temperature difference (℃)
8_6_20	146.289	79.151
22.5	148.418	74.872
25	150.205	71.724
27.5	151.741	69.369
30	153.0183	67.608

Table 6.6: Stress and temperature difference for m model 10_7_θ

θ	Maximum Hoop stress(MPa)	Maximum Temperature difference (℃)
10_7_20	-185.343	113.877
22.5	-178.855	109.546
25	-173.648	106.373
27.5	-172.183	104.025
30	-171.525	102.287

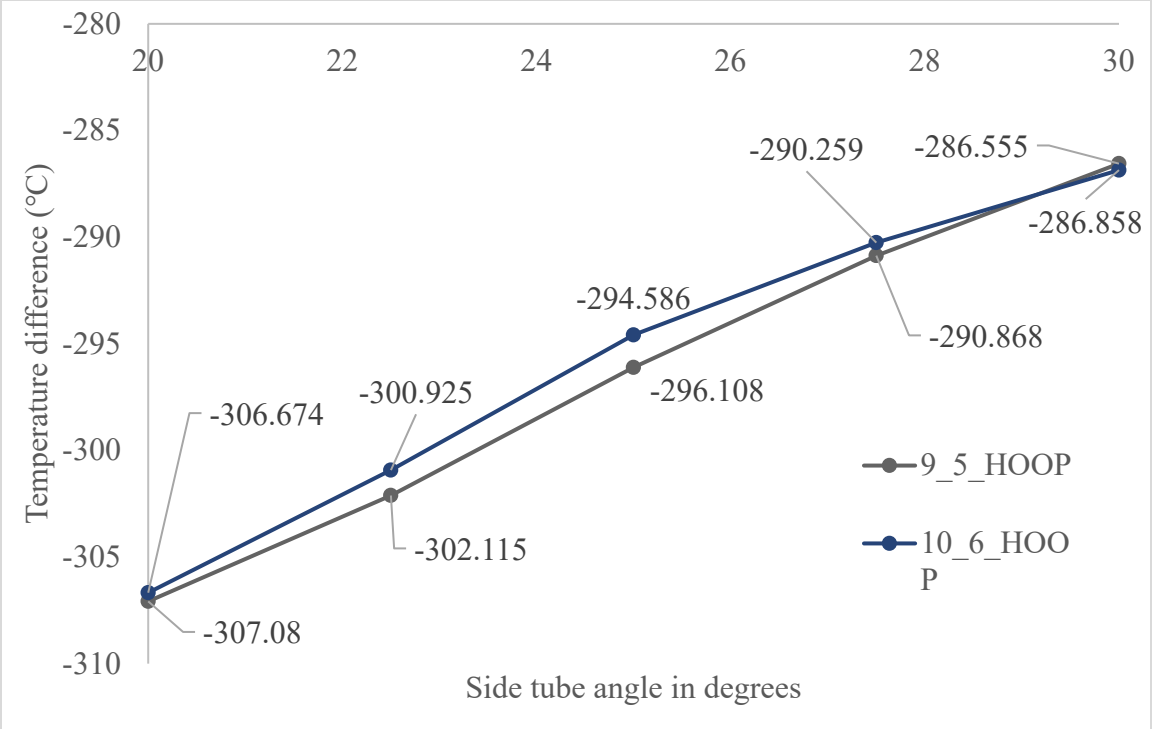

Figure 6.29: Maximum hoop stress vs side tube angle θ for models with cylinder wall thickness t = 2 inches.

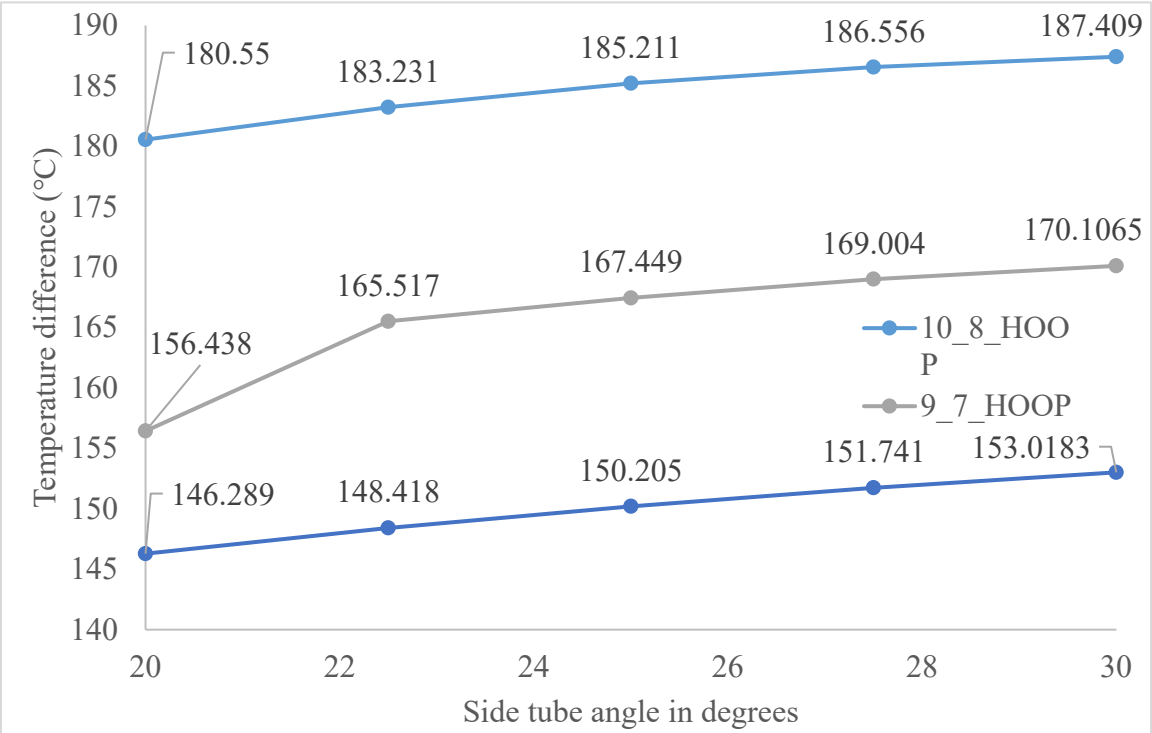

Figure 6.30: Maximum hoop stress vs side tube angle θ for models with cylinder wall thickness t = 1 inch.

The plots in fig 6.28 and fig 6.29 show variation of maximum hoop stress with increasing values of θ. It is once again seen that the maximum hoop stress values are lowest for the model with the smallest cross section area of the annulus for a given value of wall thickness.

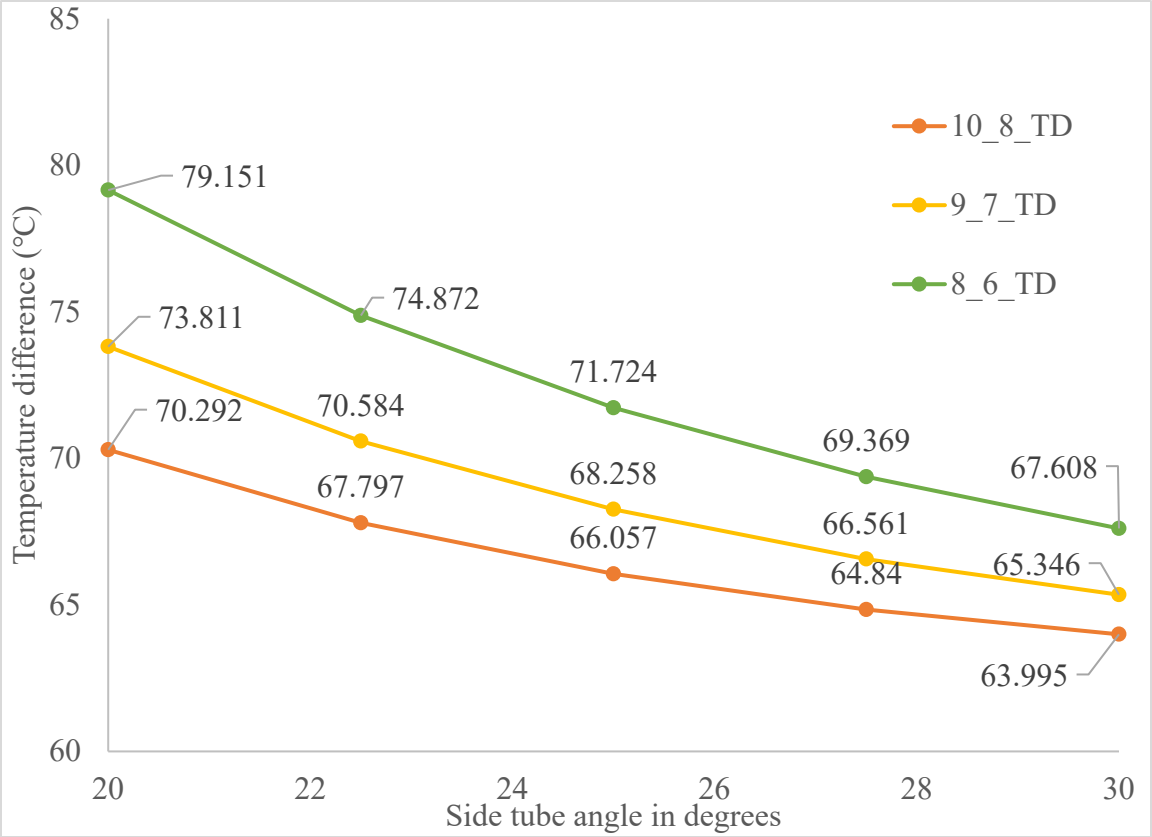

Figure 6.31: Temperature difference vs side tube angle θ for models with cylinder wall thickness t = 1 inch.

Fig 6.30 is a plot of the maximum temperature difference against the side tube angle θ for models of wall thickness t = 1 inch. The plot shows that the models with a smaller area of cross section of the annulus ring have higher values of maximum temperature differences. Based on these plot, the model 10_8_30 would have the least amount of temperature difference among the models with t = 1 inch. From fig 6.31, it is observed that

the same trend is observed in models of wall thickness t= 2 inches where the model with the smallest cross section annulus area has the highest value to temperature difference.

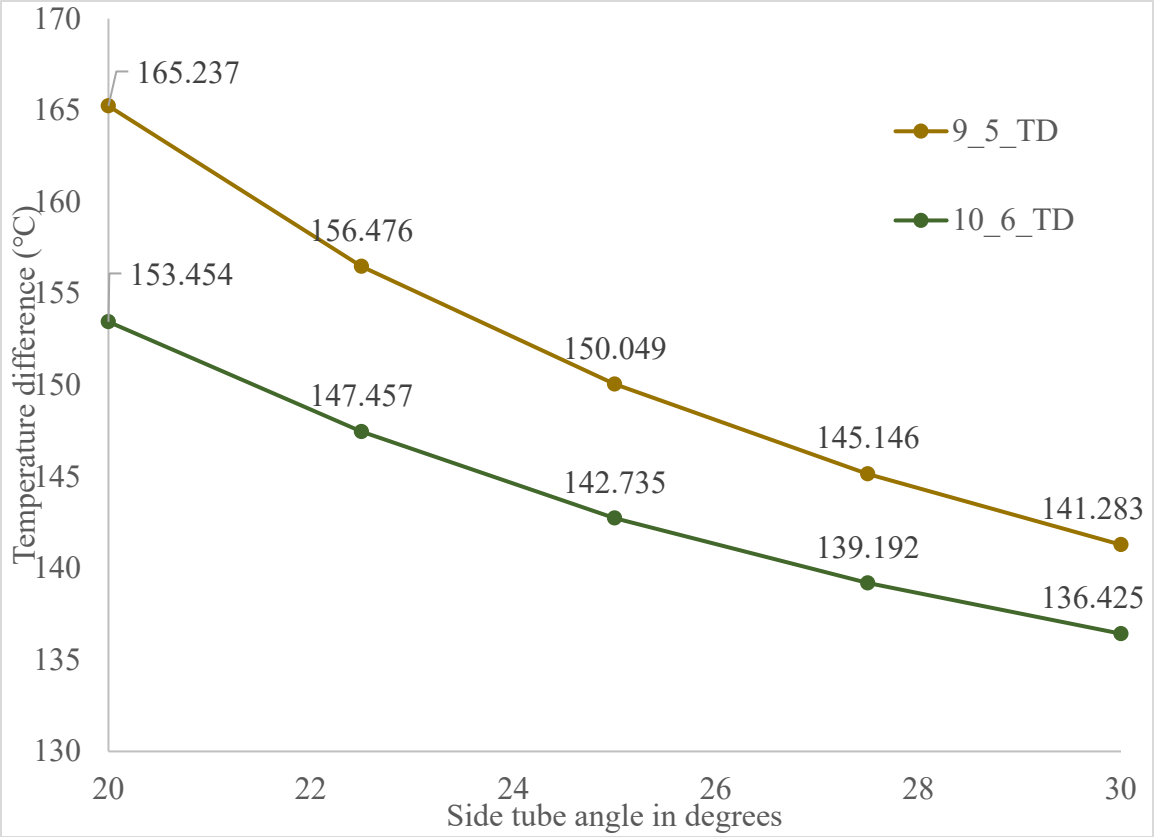

Figure 6.32: Temperature difference vs side tube angle θ for models with cylinder wall thickness t = 2 inches.

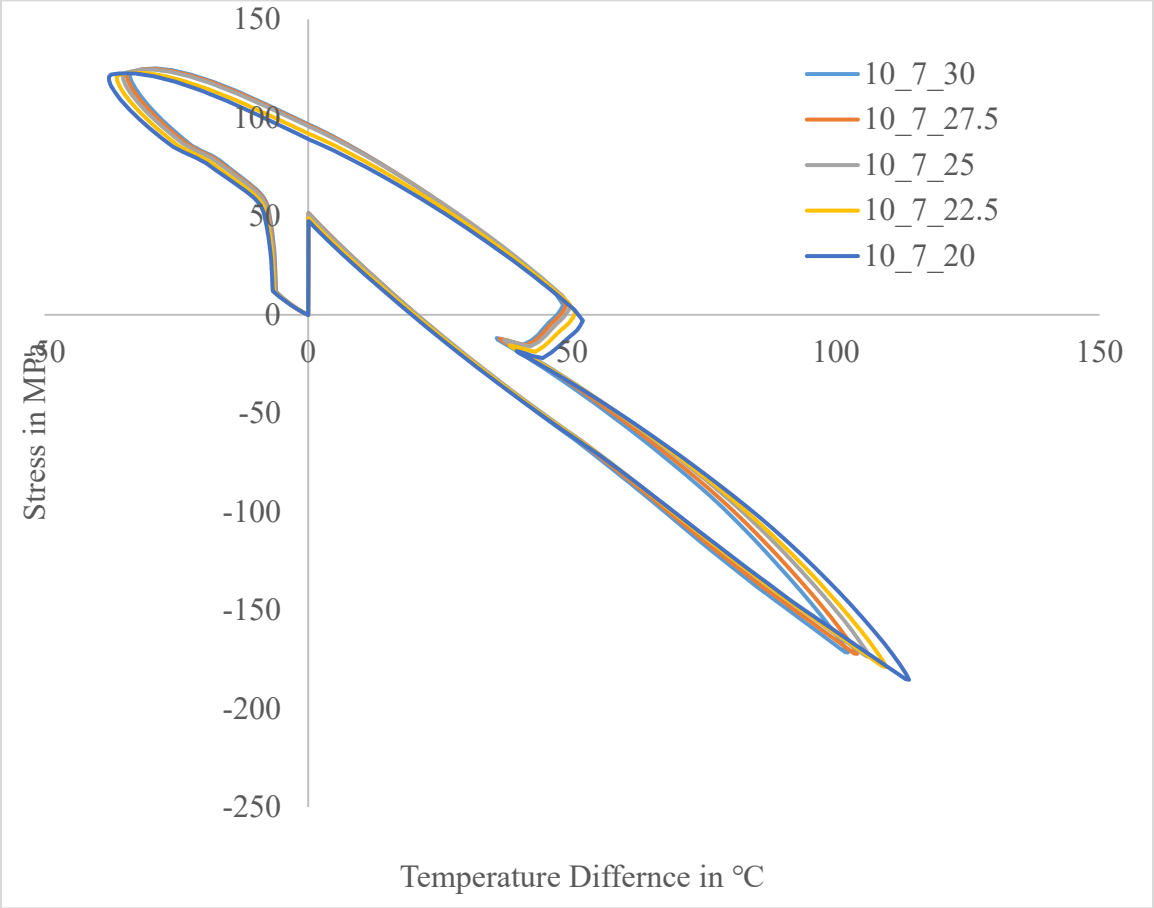

Figure 6.33: Stress (MPa) vs Temperature difference for the model with O.D = 10 inches, I.D = 7 inches for all values of θ

The plots of stress against temperature difference shown in the fig 6.36 is for that of model 10_7. The model has properties that lie in between that of 10_6 and 10_8. As shown in the following plot in fig 6.34, it is clear that they have compression stresses lower than 10_8 models and tensile stresses lower than that of 10_6 models. These properties may make them the ideal option for this given operating cycle, but a closer look at its temperature difference plot is warranted. From the plot in fig 6.35, it is seen that their temperature difference values are lesser than that of 10_6 models but still higher than the 10_8. We have already seen that the temperature difference plays a more pivotal role in

determining the maximum circumferential stress levels developed in the header segment, and hence, the model 10_8 would be the best among the three for the given operational cycle.

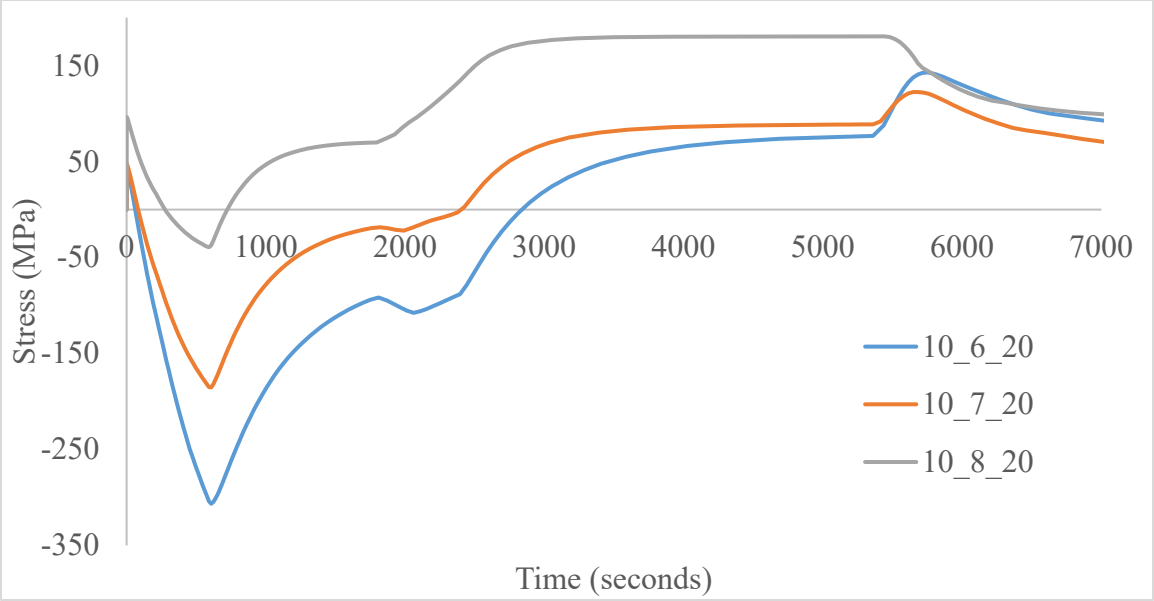

Figure 6.34: Stress (MPa) vs time (seconds) for the model with θ = 20 and O.D = 10 inches with wall thickness t = 1 inch, 2 inches and 1.5 inches.

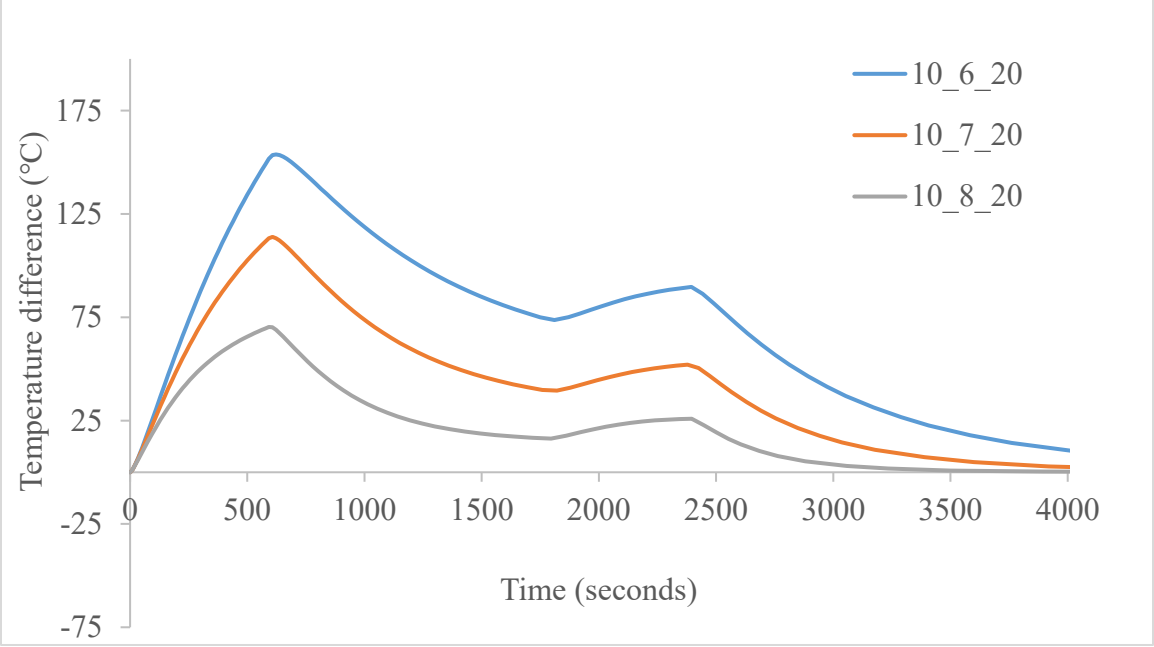

Figure 6.35: Stress (MPa) vs Temperature difference for θ = 20 and O.D = 10 inches with wall thickness t = 1 inch, 2 inches and 1.5 inches.

The verification and validation of the results in this thesis were compared to similar studies done on steam boiler headers for circumferential stress vs overall time plots and they were found to show the same trends. Similar studies were used to validate the thermal behavior for different angles of θ (side tube angles) and were found to show the same trend. The studies also compared the stress intensity factor and thermal fatigue life in relation to angle θ showed that they were inversely related.

6.1 Prediction of results:

The main goal of the secondary objective is to try to map the complete hoop stress history of a single node for a model without simulating it, using only the equation that was proposed earlier and the data obtained from the previous model simulations. The key aspect of the secondary objective is to propose a method in which the entire hoop stress values of any node can be predicted to a certain degree of accuracy without having to model and simulate a full-scale model to include a small change of a variable physical property.

To demonstrate how this is done, the 10_8 models are chosen (external diameter: 10 inches, internal diameter: 8 inches). The node chosen is the same node at which the maximum hoop stress occurs as the history of hoop stress at that node is well documented. The procedure is as follows:

The equation 5.11 is used here. The equation is used without the multiplication factor and the maximum temperature difference is replaced with the temperature difference at the corresponding time step, and the elasticity modulus that was taken as a constant for the previous step is replaced with the corresponding elasticity modulus of the corresponding time step. The equation is then used to obtain the respective values for respective time steps. This operation is implemented easily using MS Excel where the

equation is specified for one cell and the corresponding values are applied at the subsequent cells. The result of this process is a value, which will be used to obtain a factor that sets up the secondary objective. This value is divided by the hoop stress obtained using Abaqus at the corresponding time step and this value obtained is the modified multiplication factor. The modified multiplication factor for all the models starting from 20 degree side tube angle to 30 degree side tube angle is obtained in the exact same way but for the respective models and their respective time steps.

All the obtained modified multiplication factors are now tabulated in a spreadsheet software like Excel. Now the evolution of the multiplication factor is the primary factor that will be used to predict the hoop stress values of subsequent models. To study the evolution of this multiplication factor, the difference between the modified multiplication factors of subsequent models is obtained, i.e., the modified multiplication factor of model 10_8_20 is subtracted from that of 10_8_22.5, and the modified multiplication factor of 10_8-22.5 is subtracted from that of 10_8_25 and so on. At the end of this operation, there are four columns of values, which are the rates at which the multiplication factor varies from model to model. These values show the evolution of the multiplication factor as the angle of the side tube evolves. This is just one among the many behaviors of the models that is studied here to propose a way to predict the hoop stress history of future models. The values in these columns show a linear trend, but a somewhat constant value is needed to effectively model the prediction. For the before mentioned purpose, the difference best between the columns are calculated in the order of increasing angles again. This leaves us with three columns of values, which are not incremental in nature. The average of these values are taken and then they are added to the fourth column of the original differences of

modified multiplication factor. This value is later added to the modified multiplication factor of 10_8_30. The value obtained from this operation is substituted as the modified multiplication factor in the equation from the primary objective. Similarly, the temperature difference values are also tabulated and the above-mentioned calculations are done on them to obtain the extrapolated values of the temperature differences. Substituting both the modified multiplication factor and the new temperature difference, we arrive at the predicted hoop stress history. This process is repeated for all time steps using MS Excel and the values are tabulated. This predicted value is then compared with the experimental simulation that was run on Abaqus. The following figures are the plots comparing the curve from the ABAQUS simulation to the curve form the equation. The fig 6.36 for model 10_8_32.5 shows that there is less error in that plot compared to the plots of 10_8_35. This was expected as this method can produce high degrees of accuracy for models closer to the verified models. Models with higher physical parameter deviation from the original models show a higher error percentage. A suitable solution for this issue would be further examination of data from the simulations and establishing a relationship among them to increase the accuracy of these predictions. Both the multiplication factor and the temperature difference values play a key role in predicting the output of subsequent models. It is to be noted that the internal pressure term is actually omitted but the reaction to the internal pressure is also included using the multiplication factor as it shows how the combined stress from both temperature difference and internal pressure evolve with increase in θ. The fig 6.36 through fig 6.39 are plots of the calculated values against the simulated values of stresses.

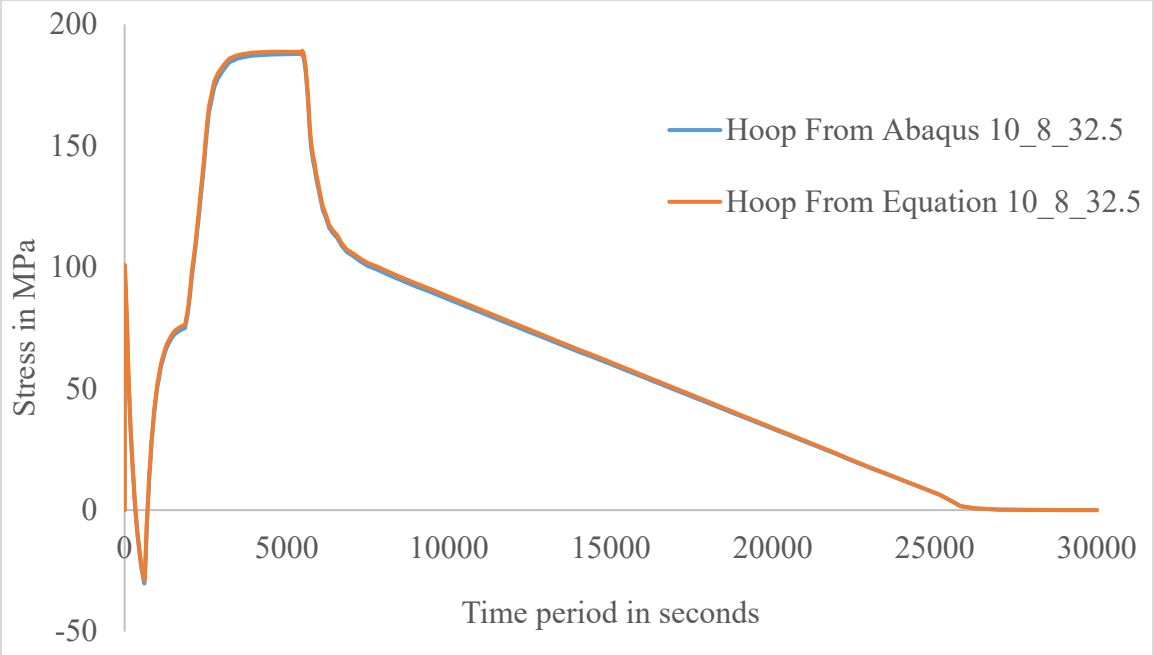

Figure 6.36: Hoop stress vs time period comparison between equation results and ABAQUS results for 10_8_32.5

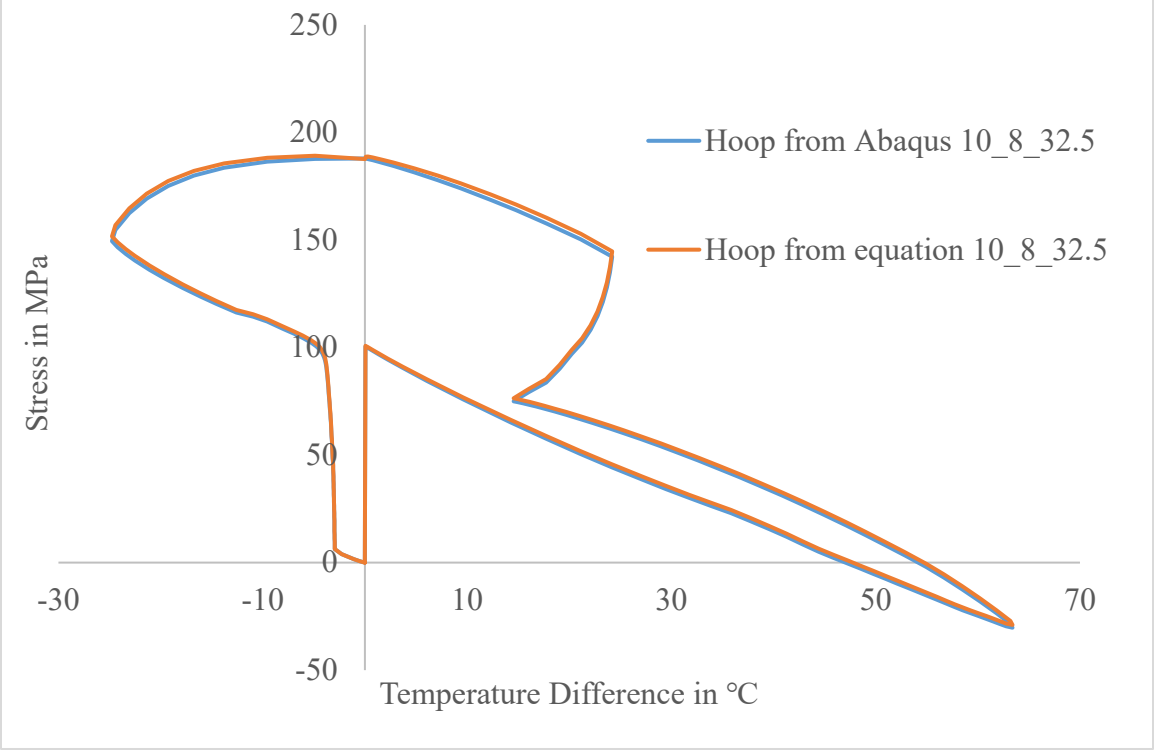

Figure 6.37: Hoop stress vs Temperature difference comparison between equation results and ABAQUS results for 10_8_32.5

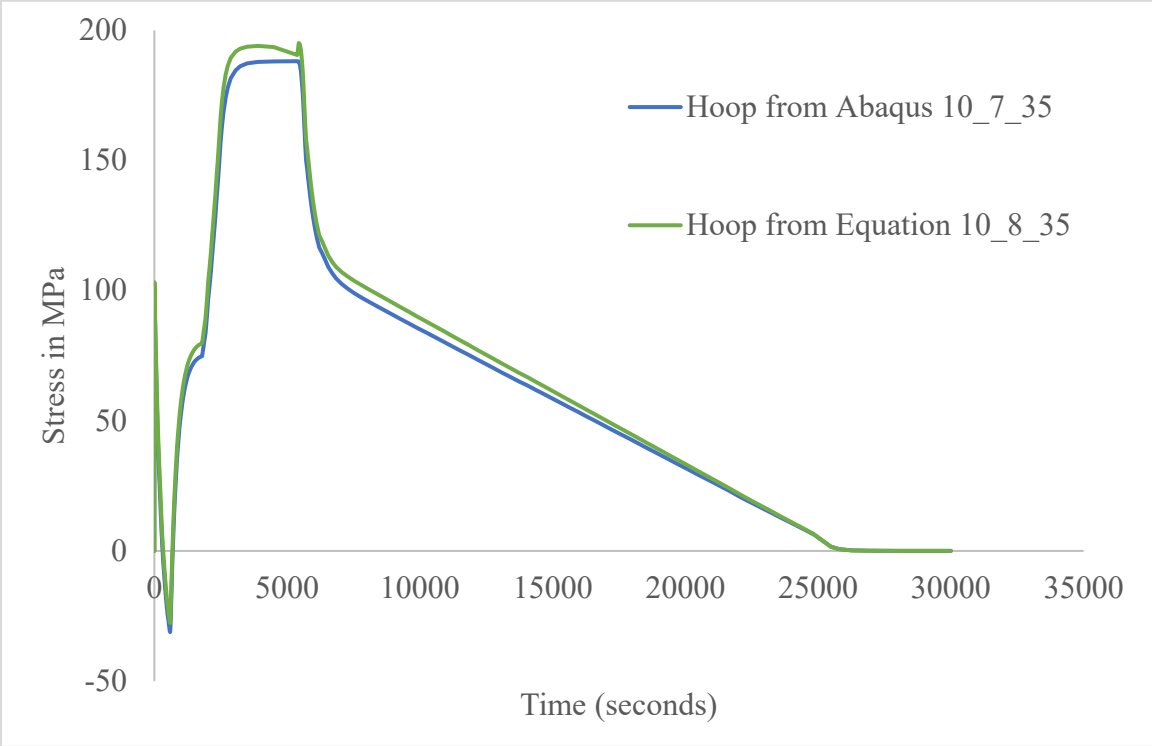

Figure 6.38: Hoop stress vs time period comparison between equation results and ABAQUS results for 10_8_35

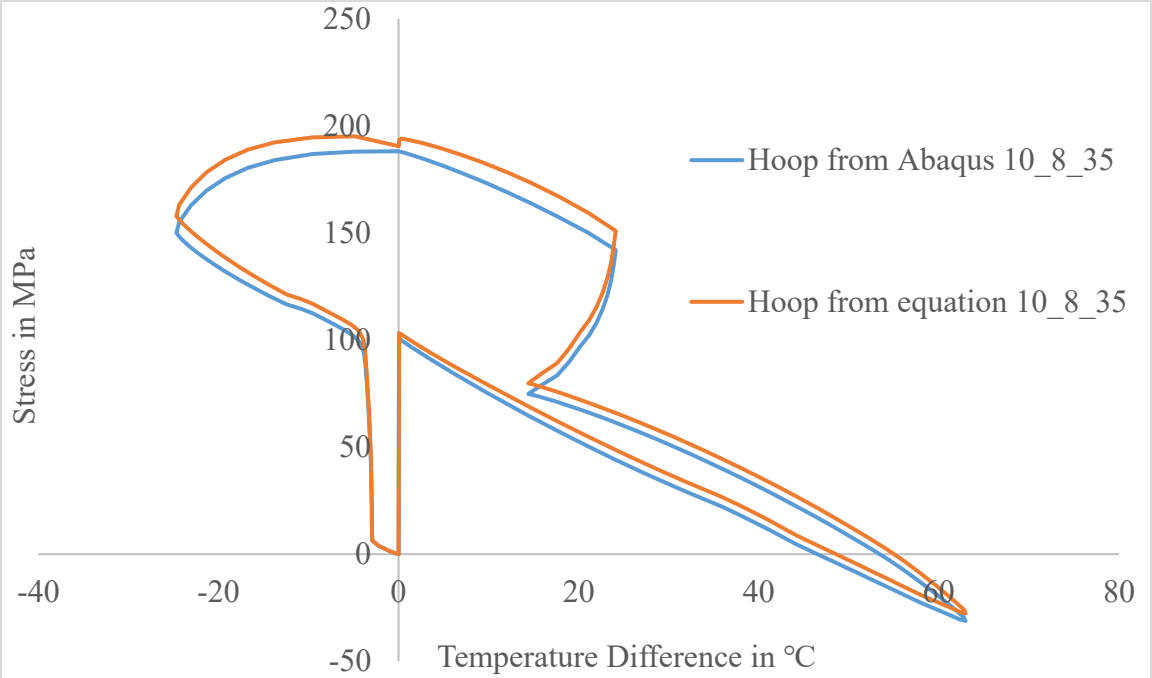

Figure 6.39: Hoop stress vs Temperature difference comparison between equation results and ABAQUS results for 10_8_35

From the fig.6.38 and 6.39, it is clear that this method begins deviating from the simulation output. A much-detailed analysis of the hoop stress values of previous simulations with both larger and smaller side tube angle increments can accurately capture the evolution of the modified multiplication factor, increasing the accuracy of these results in subsequent simulations with increasing increments. The most important observation from these results is that any model that requires extensive modelling and analysis due to some small variations in design can be approached by this proposed method to reduce the computational cost and time.

The following figures from fig 4.40 through fig 4.45 are the plots of both circumferential and radial stresses due to the temperature difference in the model alone. This result was obtained by simulating the models with the internal pressure without the temperature of the steam applied. The circumferential and radial stresses from these models at the point of maximum hoop stress is plotted. These values are then tabulated side by side with the original coupled displacement results. The difference between these two values are tabulated and plotted. The resultant plot gives the values of both circumferential and radial stresses due to the temperature difference alone. These results show a good picture into the amount of stress caused by the temperature variations in the model. The temperature difference alone sets up a significant amount of stress in the absence of the internal pressure forces. This result is in line with the previous finding where it was observed that temperature differences play a greater role in determining the final stress profile in the header.

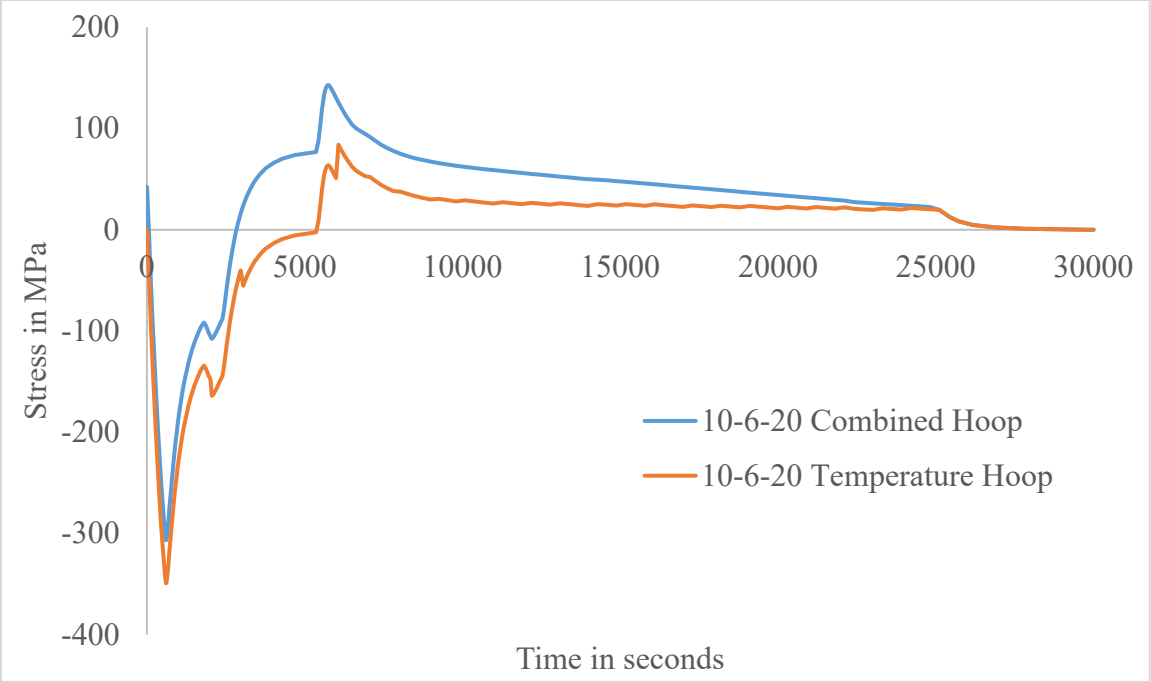

Figure 6.40: Combined hoop stress and the hoop stress due to temperature difference alone against time for model with OD = 10 inches and ID = 6 inches and tube angle 20º

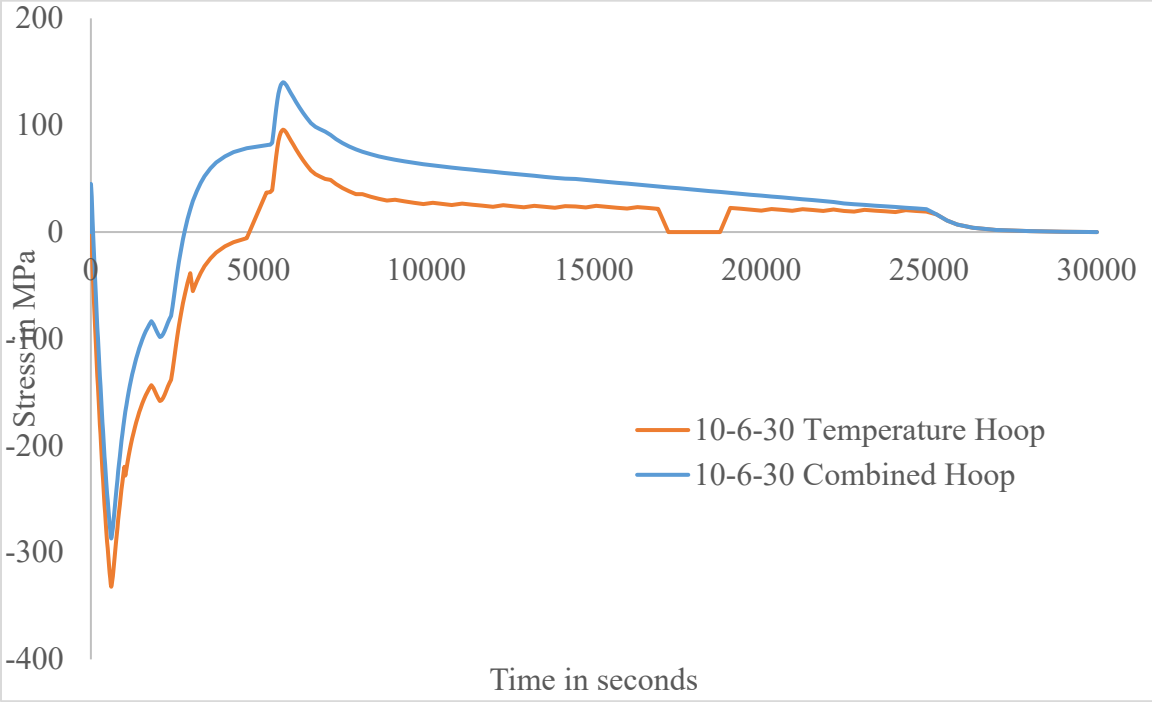

Figure 6.41: Combined hoop stress and the hoop stress due to temperature difference alone against time for model with OD = 10 inches and ID = 6 inches and tube angle 30º

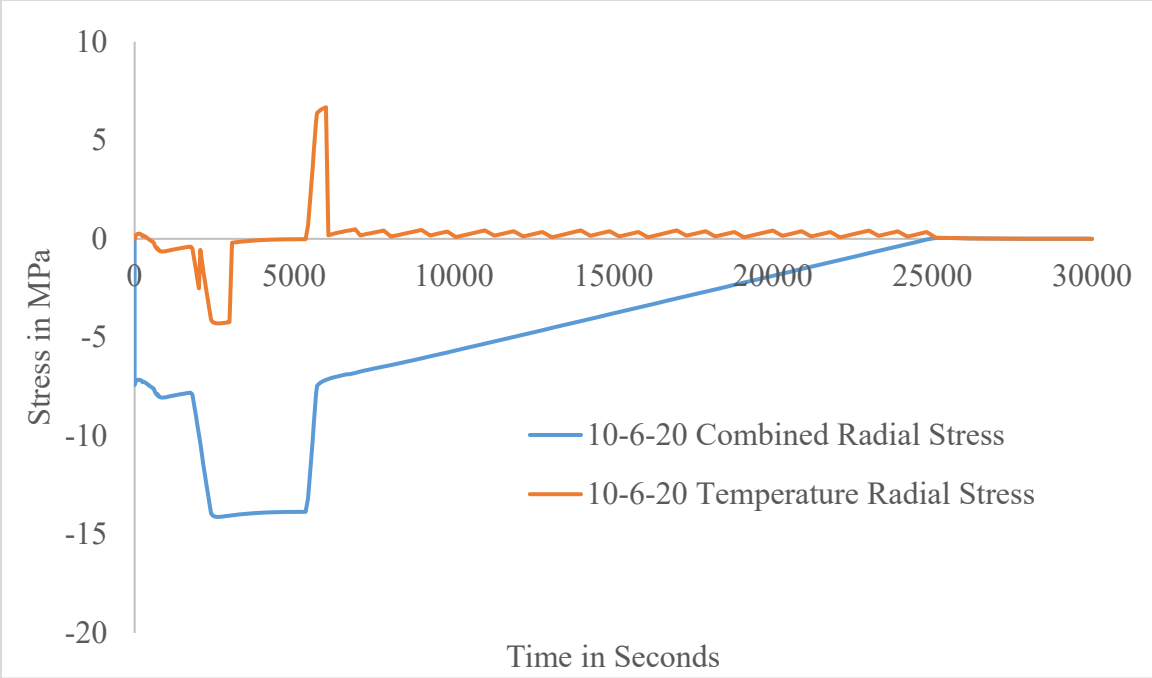

Figure 6.42: Combined radial stress and the radial stress due to temperature difference alone against time for model with OD = 10 inches and ID = 6 inches and tube angle 20º

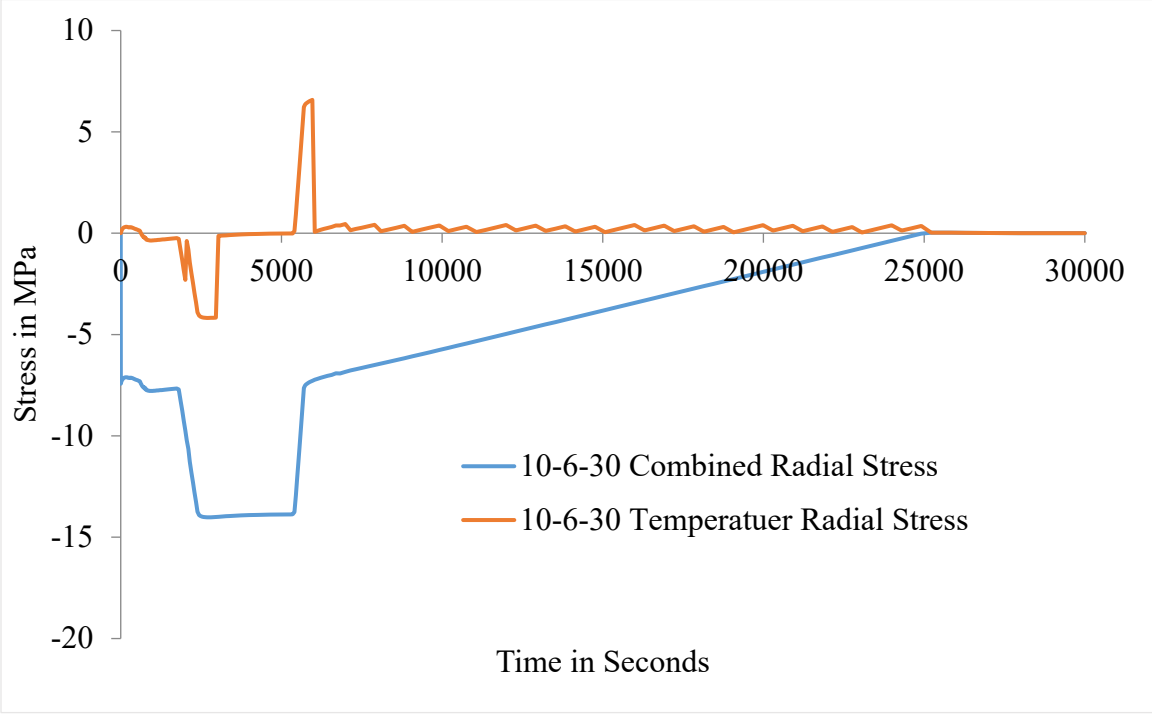

Figure 6.43: Combined radial stress and the radial stress due to temperature difference alone against time for model with OD = 10 inches and ID = 6 inches and tube angle 30º

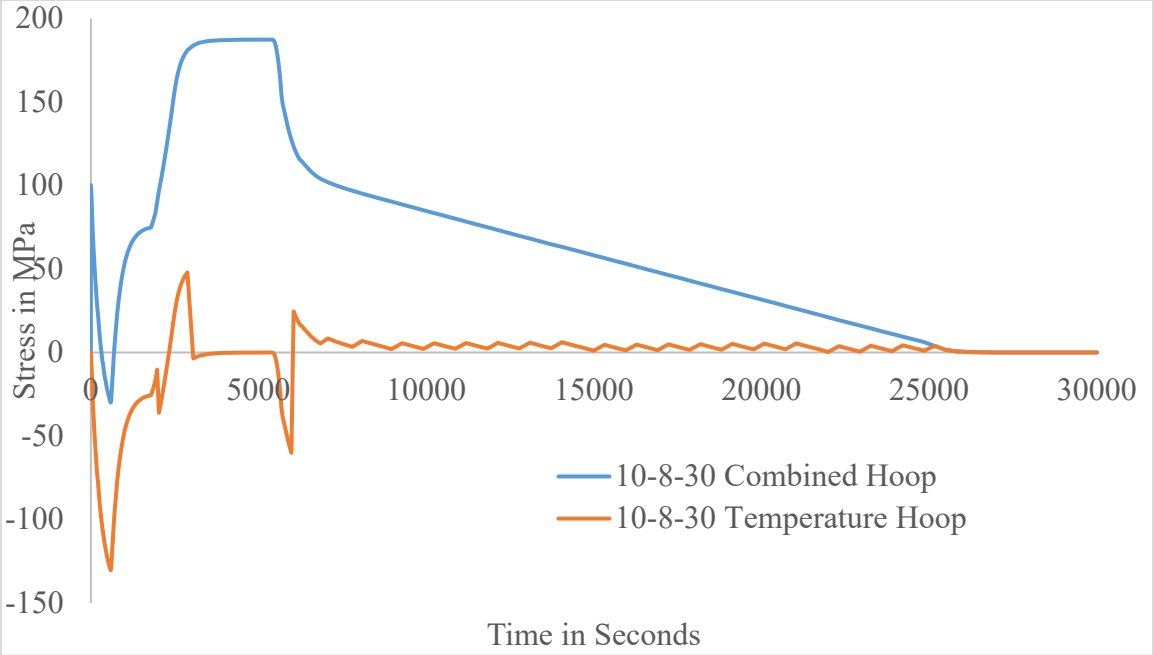

Figure 6.44: Combined hoop stress and the hoop stress due to temperature difference alone against time for model with OD = 10 inches and ID = 8 inches and tube angle 30º

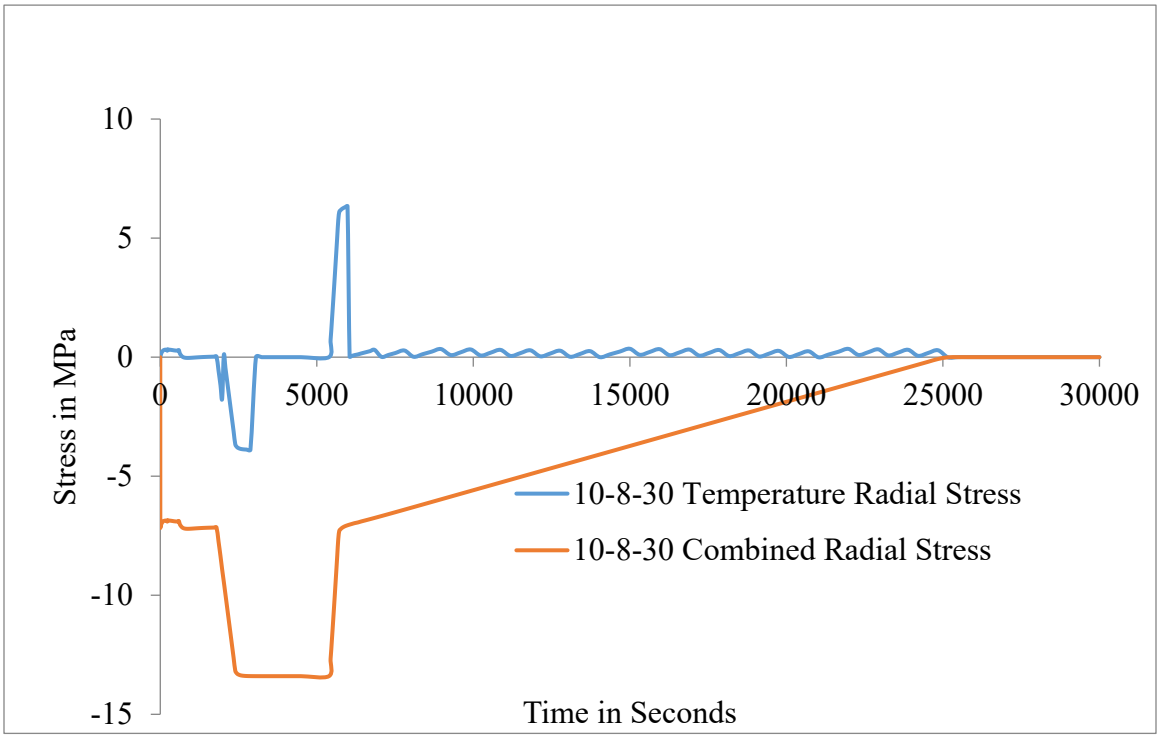

Figure 6.45: Combined radial stress and the radial stress due to temperature difference alone against time for model with OD = 10 inches and ID = 8 inches and tube angle 30º

For the thinner models the trend is slightly different. The radial stress looks to be much lower when the stress due to internal pressure is removed and the was expected as the internal pressure load acts directly on the walls and the main radial stress in the model is a direct result of this. Upon removal of this internal pressure load, the radial stress is significantly reduced. Hoop stresses are also much lower in thicker models because the thermal equilibrium is attained at a much faster rate due to the absence of excess material, and without the internal pressure load, the hoop stresses remain minimal compared to the thicker models. This again shows that the initial inference of thinner models having superior circumferential stress properties for similar operational cycles.

Four models with three side stubs were modeled and analyzed to study the behavior of circumferential stress in a multiple stub model. The model with external diameter 10 inches and internal diameter 8 inches was chosen to perform this analysis. The thicker models were not included in this simulation as the marked difference between the thicker and thinner models have already been established using the results from the previous simulations. The 10_8 model was designed with three side stubs instead of one and the angles between the vertical and the last tube was a multiple of the angle between the vertical and the middle tube. For example, the model with a middle tube angle of 20 degrees was modelled with an angle of 40 degrees for the last tube. This design principle was followed to maintain symmetry and in accordance with current header designs. The respective angles of the middle and the last tube from the vertical for the models are 20-40, 30-60, 35-70 and 40-80. These angles provide an insight as to how the stress and thermal properties vary when multiple side stubs are present.

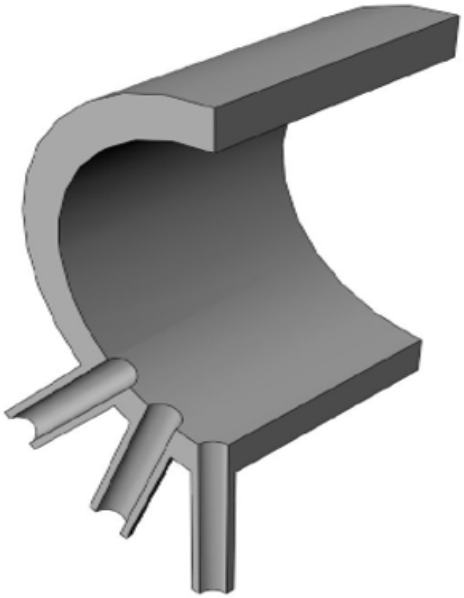

Figure 6.46: Model with middle tube angle 20 degrees and last tube angle 40 degrees

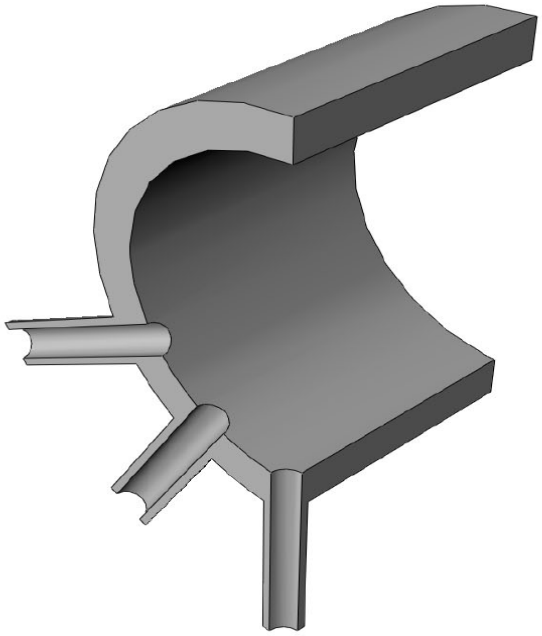

Figure 6.47: Model with middle tube angle 30 degrees and last tube angle 60 degrees

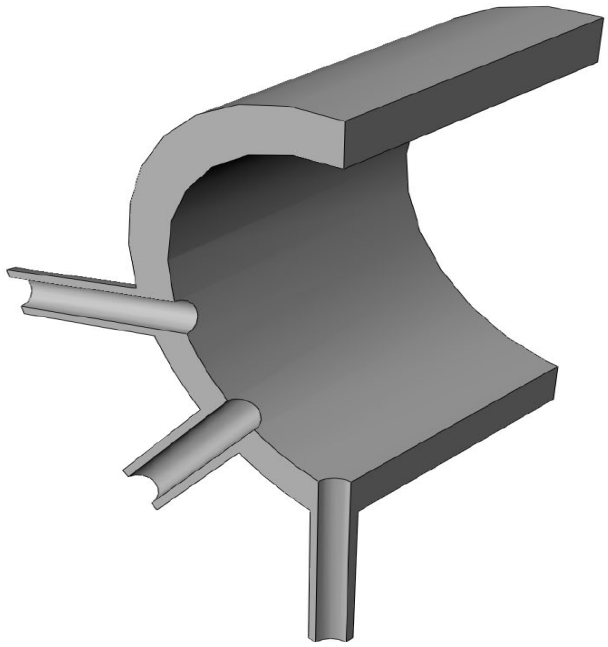

Figure 6.48: Model with middle tube angle 35 degrees and last tube angle 70 degrees

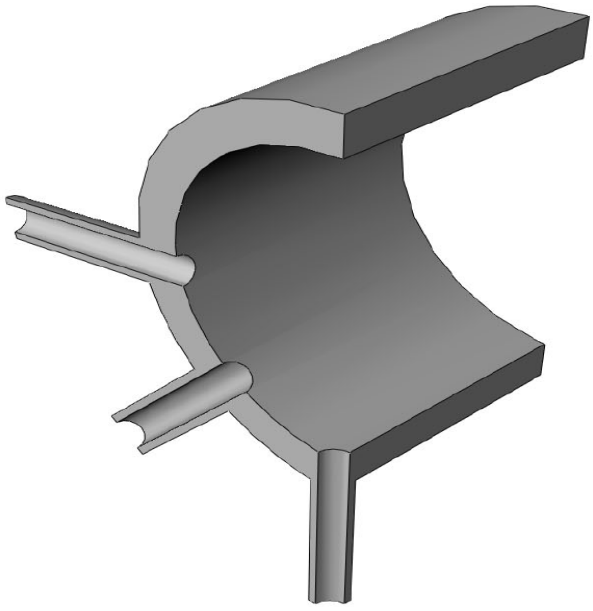

Figure 6.49: Model with middle tube angle 40 degrees and last tube angle 80 degrees

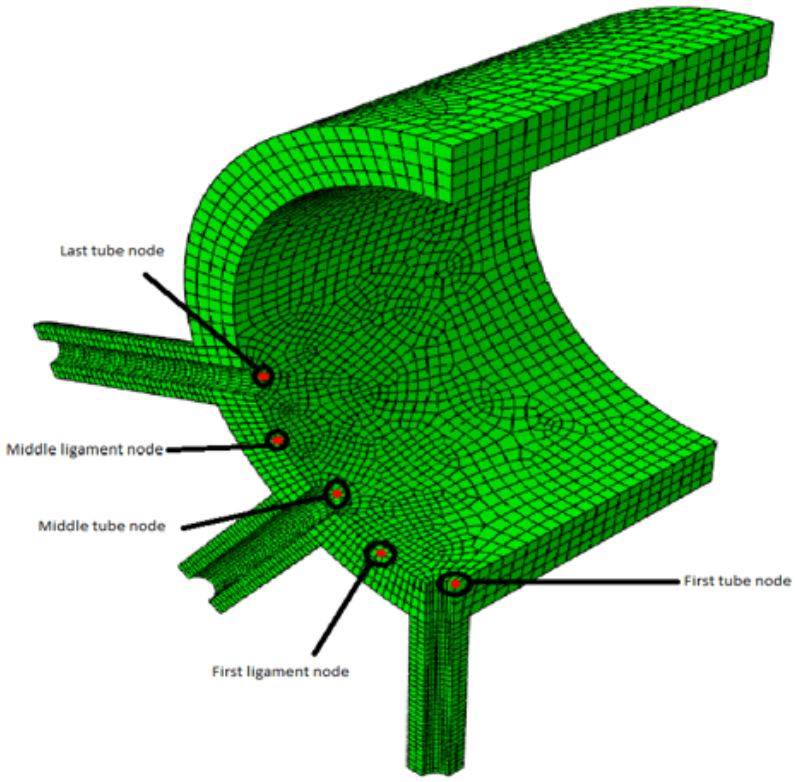

Figure 6.50: Nodes for result processing and plots

Some additional boundary conditions were prescribed to take into the account the presence of the two additional side stubs. Both the middle tube and the last tube were constrained using equations constraints. Both pipes were also subjected to end loads using the same method we used to calculate end loads earlier. Side stub geometrical specifications were altered to accommodate multiple tubes in the main header segment. The inner surface of the additional tubes were included into the main surface set. The meshing was done using partitioning and a slightly finer mesh was applied to the area where higher stress levels were expected. The following result plots were obtained from the simulations. The data was collected from Abaqus and processed using MS Excel to develop these plots.

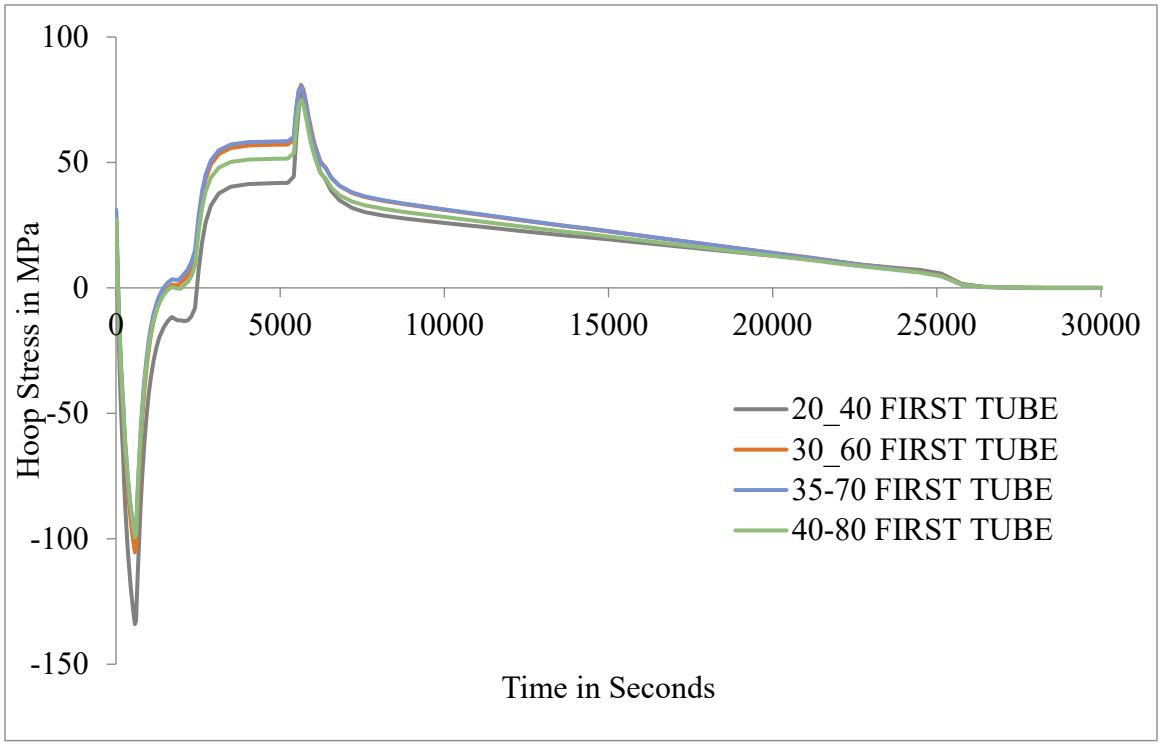

Figure 6.51: Hoop stress vs time period of the first tube for all three side tube stub models

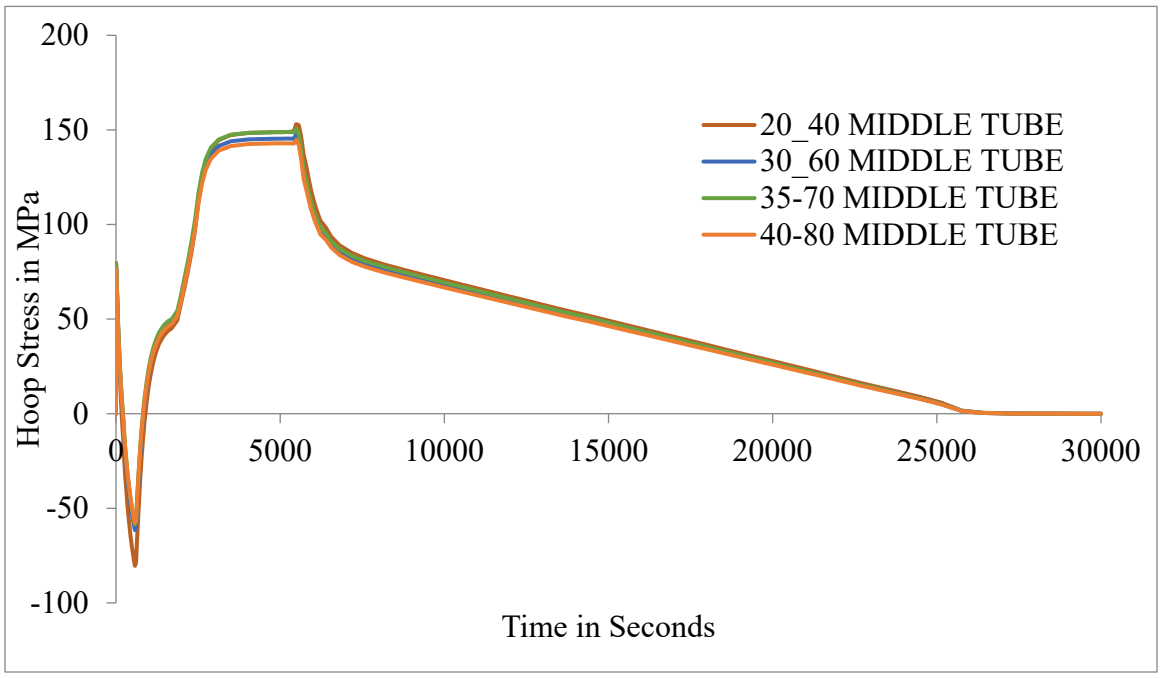

Figure 6.52: Hoop stress vs time period of the second tube for all three side tube stub models

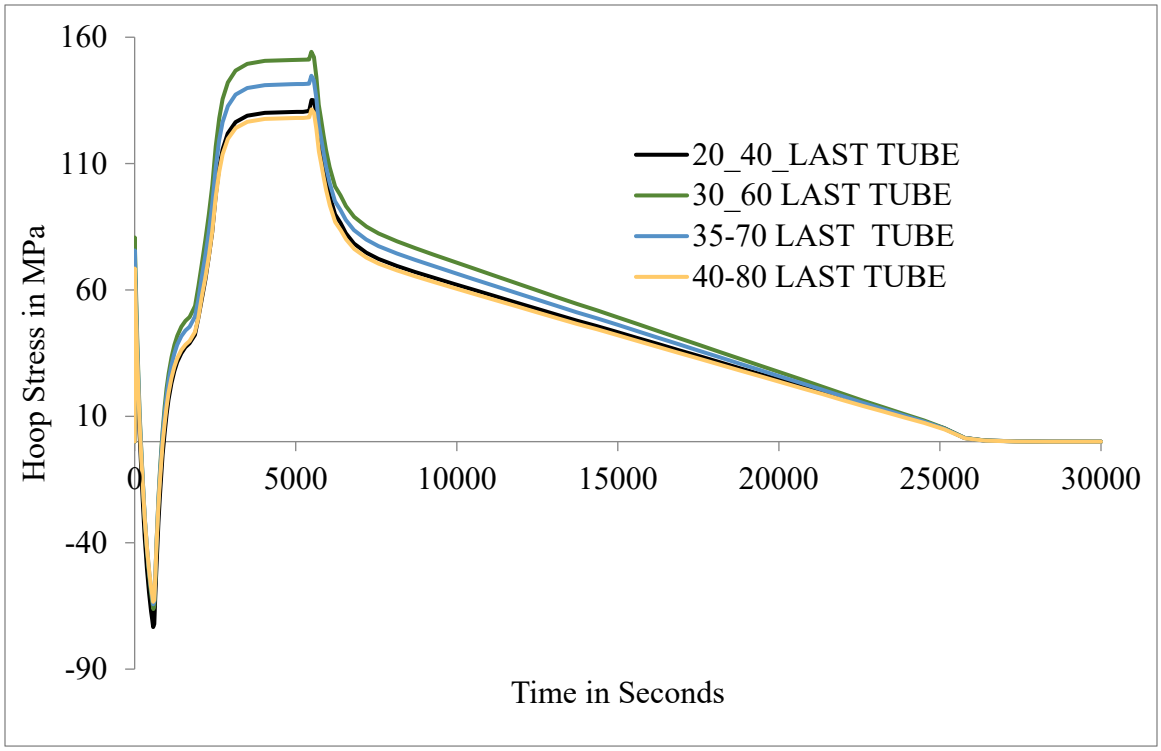

Figure 6.53: Hoop stress vs time period of the third tube for all three side tube stub models

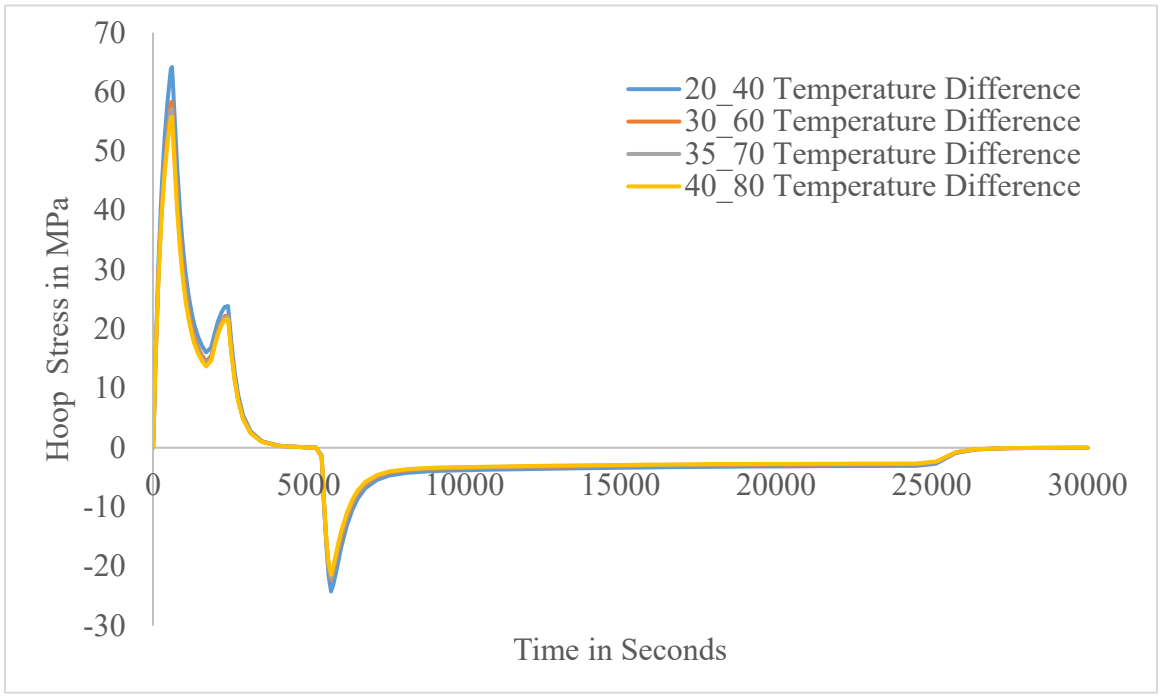

Figure 6.54: Temperature Difference vs time period

The plot from fig 6.52 is of the hoop stress values against time for the node located in the center of the middle tube on the inner surface of the main header. From the fig 6.52 through fig 6.53, it is seen that both the middle tube and the last tube stress values show an interesting pattern. The stress values for the middle and the last tube show similar trends. For the model with the side tube angles 20 and 40, the stress is low, and it keeps increasing until the model with side tube angle 35 and 70 degrees, but the next model with side tube angles 40 and 80 degrees, the stress values actually drop and are the lowest among the four models. This could be considered as the sweet spot for this operation cycle and material. The temperature difference between the same nodes that were chosen for the single tube models is chosen again and the plot is shown in fig 6.54. It is seen that the temperature difference in the models with lesser angles or smaller ligaments are higher than the model with larger angles and larger ligaments. This behavior sets up the initial compressive stress in the models, which is larger in the models with smaller angles and as the temperature, difference reaches a minimum, the tensile stress peaks. The temperature difference properties mirror those of the single tube models. For the plot in FIGURE, the reslut shows that the model with the least angle has a considerably large compression hoop, but the least amount of hoop in tension. This model is followed by the model with side tube angles 40 and 80, the largest angle models.

The fig 6.55 and fig 6.56 show the plot of the hoop streses in the ligaments of the models. The first ligament results show that the 20 and 40 degree model has the lowest overall stress with the highest compreesive stress, the largest angle model with the angles 40 and 80 is at a close second, with the other two models slightly higher. The middle ligament hoop stress plt shows that the lrgest angle model with the side tube angle 40 nd

80 actually has the highest stress value in tension and the values drops with the reduction of side tube angles, but the interesting part is that the highest stress is actually in compression and the 40 and 80 model actually has the lowest value of stress in compression.

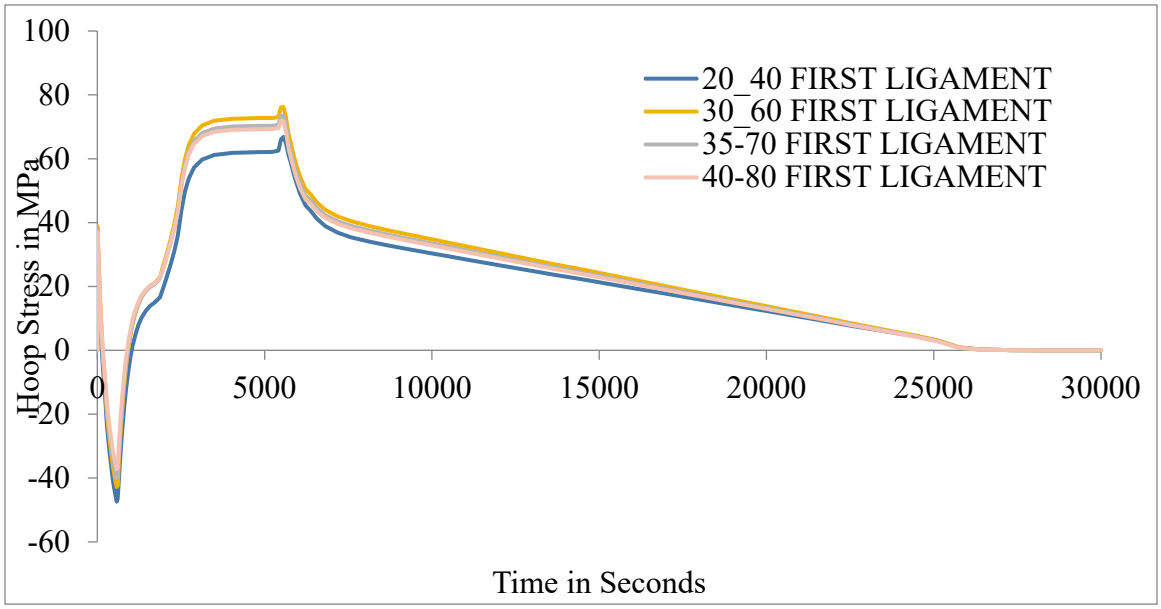

Figure 6.55: Hoop stress vs time period of the first ligament for all three side tube stub models

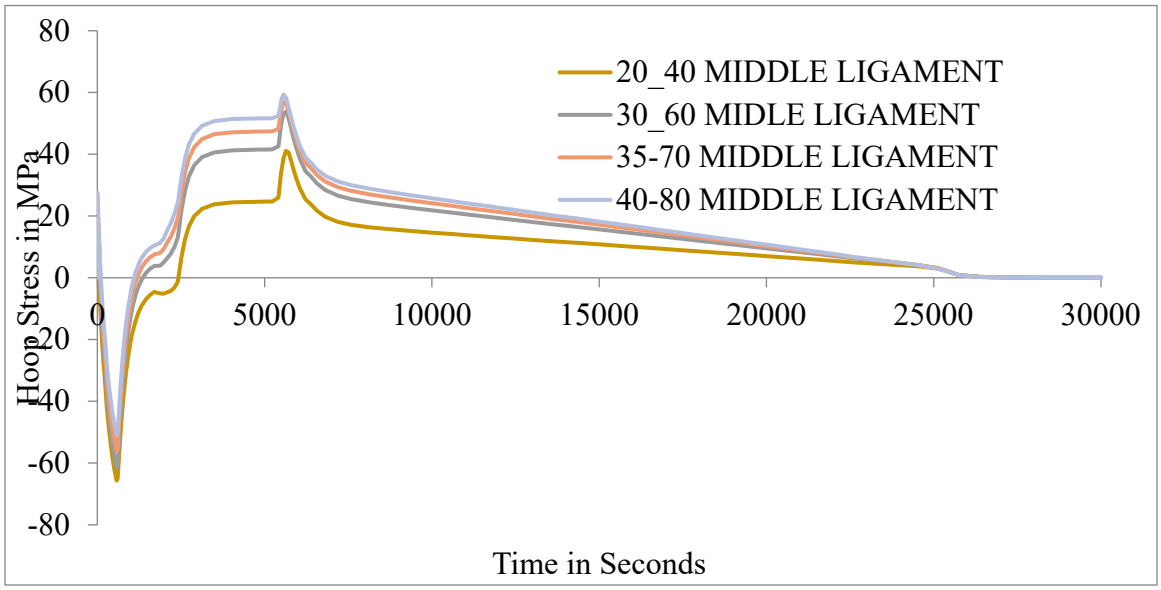

Figure 6.56: Hoop stress vs time period of the middle ligament for all three side tube stub models

The following table shows the yield stress properties of P31 steel at elevated temperatures. It can be seen that the maximum stress, which is around the order of 306 MPa does not occur at the maximum temperature, but rather at the maximum temperature difference. The stress limits are well within the yield stress value of P91 steel for that temperature.

Table 6.7 : P91 Yield strength at elevated temperatures.

Temperature ℃	Yield Strength MPa
37	413.69
65	393.70
93	385.42
121	380.60
149	377.83
204	377.14
260	377.14
315	375.76
343	373.32
371	366.8
399	358.53
426	347.50
454	334.40
482	317.84
510	299.23
537	277.17

CHAPTER 7: INFERENCE AND CONCLUSION

There are multiple things to take away from the analysis of all the results. The primary objective of this thesis was to conduct a detailed study of the circumferential stress behavior of the header section when two primary physical properties of the header are varied. It is found that that the temperature difference plays a major role in determining the maximum circumferential stress developed within the header, both in tension and in compression. The temperature difference profile in turn is dependent on the side tube angle θ. The side tube angle is also responsible for the stress intensity in the model, which is indirectly verified in the results of this simulations. Some external papers have also confirmed that header with a longer ligament size, i.e higher values of θ are less susceptible to creep fatigue damage. It is clear that when if the header is not insulated during a typical operating cycle like the one used for this simulation, it's operation life is will be reduced compared to an insulated one. The initial spike in compressive stresses for the models of thickness t = 2 inches is found to be the direct result of the initial temperature difference. It was also found that these values were the maximum values of stress obtained in the cycle for those models. Lack of insulation may result in reduced life and increase in fuel bills compared to an insulated steam boiler header. The ideal model for the cycle used in this thesis would be the model with the least amount of temperature difference and least amount of stress. From the results, the model 8_6_30 (ED = 8 inches, ID = 6 inches and θ = 30º) show the most favorable properties. It was concluded from the plots that a higher value of θ and a lower area of cross section of the annulus for models of same wall thickness shows the least amount of temperature difference and circumferential stresses.

The entire method used in this thesis can be used as a test bed for different configurations of operating cycles for the same set of models. The physical parameters of the models can also be varied in terms of their outer and inner diameters and also the side tube angle θ can also be varied. The python codes used for the 30 simulations were developed in such a way that changing less than 20 lines of code can introduce a new operating cycle for a model with completely different OD, ID and θ with insulation in ABAQUS. This opens up new possibilities to model and simulate multiple models with different parameters to determine the best dimensions for a given cycle. The overall steam boiler header design remains unchanged from the cylindrical vessel design currently employed all over the world and most models can be simulated with minimal modifications to the code. This can result in significant reduction in time when simulation large number of models. The accuracy and validity of the results were verified by similar papers dealing with steam header stress analysis.

Thus, a detailed analysis of circumferential stresses for a given nominal operating cycle for a steam boiler header has been conducted. Using the results from around 30 different models with varying side tube angles and inner and outer diameters, the most efficient header in terms of circumferential stress and temperature difference has been identified. In addition to that, the relationship between the circumferential stresses and the physical properties have also been studied. A method to simulate additional models with varying physical parameters and additional operating cycles has also been proposed by the means of the provided python script for use with ABAQUS.

REFERENCES

[1] Shrestha, T., Basirat, M., Alsagabi, S., Sittiho, A., Charit, I., & Potirniche, G. P. (2016). Creep rupture behavior of welded Grade 91 steel. *Materials Science and Engineering: A, 669*, 75-86. doi:10.1016/j.msea.2016.05.065

[2] Wanke, T. S. (2015, February 02). Pressure Rating Hydraulic Components. Retrieved from https://www.hydraulicspneumatics.com/technologies/pressure-rating-hydraulic-components

[3] Dixon, R. D., Peters, D. T., & Keltjens, J. G. (2002). Stress Concentration Factors of Cross-Bores in Thick Walled Cylinders and Square Blocks. *High Pressure Technology*. doi:10.1115/pvp2002-1162

[4] Adenya, C. A., & Kihiu, J. M. (2017, June 22). STRESS CONCENTRATION FACTORS IN THICK WALLED CYLINDERS WITH ELLIPTICAL CROSS-BORES. Retrieved from http://journals.jkuat.ac.ke/index.php/jscp/article/view/697

[5] Sinclair, G., & Helms, J. (2015). A review of simple formulae for elastic hoop stresses in cylindrical and spherical pressure vessels: What can be used when. *International Journal of Pressure Vessels and Piping,128*, 1-7. doi:10.1016/j.ijpvp.2015.01.006

[6] Gerdeen, J. C., & Smith, R. E. (n.d.). Experimental determination of stress-concentration factors in thick-walled cylinders with crossholes and sideholes. Retrieved from https://link.springer.com/article/10.1007/BF02320753

[7] Faupel, J. H., & Harris, D. B. (1957). Stress Concentration in Heavy-Walled Cylindrical Pressure Vessels -Effect of Elliptic and Circular Side Holes. *Industrial & Engineering Chemistry,49*(12), 1979-1986. doi:10.1021/ie50576a029

[8] Dzierwa, P., Taler, D., Taler, J., & Trojan, M. (2014). Optimum Heating of Thick Wall Pressure Components of Steam Boilers. *Volume 1: Fuels and Combustion, Material Handling, Emissions; Steam Generators; Heat Exchangers and Cooling Systems; Turbines, Generators and Auxiliaries; Plant Operations and Maintenance; Reliability, Availability and Maintainability (RAM); Plant Systems, Structures, Components and Materials Issues*. doi:10.1115/power2014-32080

[9] Somadder, S., & Islam, M. S. (2018). Stress Analysis of a Cylinder Subjected to Thermo-mechanical Loads by Using FEM. *IOP Conference Series: Materials Science and Engineering,438*, 012036. doi:10.1088/1757-899x/438/1/012036

[10] *Abaqus Analysis User's Guide.*

[11] Kandil, A. (1996). Analysis of thick-walled cylindrical pressure vessels under the effect of cyclic internal pressure and cyclic temperature. *International Journal of Mechanical Sciences,38*(12), 1319-1332. doi:10.1016/0020-7403(96)00001-x

[12] Naga, S. A. (1986). Optimum Working Conditions in Thick Walled Cylinders. *Journal of Engineering Materials and Technology,108*(4), 374. doi:10.1115/1.3225897

[13] Blumer, U., & Stumpf, M. (1988). Mechanical design of the hot steam headers of the THTR-300 steam generators (IWGGCR--15). International Atomic Energy Agency (IAEA)

[14] Tomkins, B. (1973). Fatigue failure criteria for thick-walled cylindrical pressure vessels. *International Journal of Pressure Vessels and Piping,1*(1), 37-59. doi:10.1016/0308-0161(73)90006-9

[15] N, P. B. (2017). Stress and Failure Analysis of Thick Walled Cylinder with Oblique Hole. *International Journal of Engineering Research and,V6*(08). doi:10.17577/ijertv6is080017

[16] Camilleri, D., Mackenzie, D., & Hamilton, R. (2006). Shakedown of a Thick Cylinder With a Radial Crosshole. *Volume 3: Design and Analysis*. doi:10.1115/pvp2006-icpvt-11-93302

[17] "ASTM A335/ASME SA335 P12 High Pressure Steel Pipe Specification." (August 2, 2018) Retrieved from https://www.piyushsteel.com/alloysteel-standard-products/astm-A335-asme-sa335-pipetube/pipetube-type-astma335-asmesa335-p12-alloysteelpipes.html

[18] Perrin, Ian., et al. Design Guidelines for the Effects of Creep, Fatigue & Creep-Fatigue Interaction with Design-By-Analysis and Nondestructive Inspection Acceptance Criteria, 2014.

[19] Element Library: overview, (August 10. 2018) Retrieved from https://www.sharcnet.ca/Software/Abaqus/6.14.2/v6.14/books/usb/default.htm?startat=pt06ch28s01ael03.html

APPENDIX : PYTHON SCRIPT USED FOR THE SIMULATION OF MODEL 10_8_20

```
# -*- coding: mbcs -*-
from part import *
from material import *
from section import *
from assembly import *
from step import *
from interaction import *
from load import *
from mesh import *
from optimization import *
from job import *
from sketch import *
from visualization import *
from connectorBehavior import *

    #HEADER OUTER DIA
mdb.models['Model-1'].ConstrainedSketch(name='__profile__',
sheetSize=1000.0)
mdb.models['Model-
1'].sketches['__profile__'].CircleByCenterPerimeter(center=(
    0.0, 0.0), point1=(-40.0, -80.0))
mdb.models['Model-1'].sketches['__profile__'].geometry.findAt((40.0,
80.0))
mdb.models['Model-1'].sketches['__profile__'].RadialDimension(curve=
    mdb.models['Model-
1'].sketches['__profile__'].geometry.findAt((40.0, 80.0),
    ), radius=127, textPoint=(-142.092498779297, -5.26472473144531))

    #HEADER INNER DIA
mdb.models['Model-
1'].sketches['__profile__'].CircleByCenterPerimeter(center=(
    0.0, 0.0), point1=(-5.0, -75.0))
mdb.models['Model-1'].sketches['__profile__'].geometry.findAt((5.0,
75.0))
mdb.models['Model-1'].sketches['__profile__'].RadialDimension(curve=
    mdb.models['Model-1'].sketches['__profile__'].geometry.findAt((5.0,
75.0),
    ), radius=101.6, textPoint=(-129.864944458008, -51.5944595336914))

    #INITIAL EXTRUDE
mdb.models['Model-1'].Part(dimensionality=THREE_D, name='Part-1', type=
    DEFORMABLE_BODY)
mdb.models['Model-1'].parts['Part-1'].BaseSolidExtrude(depth=200.0,
sketch=
    mdb.models['Model-1'].sketches['__profile__'])
del mdb.models['Model-1'].sketches['__profile__']

    #DATUM CSYS AND PLANE
mdb.models['Model-1'].parts['Part-
1'].DatumCsysByThreePoints(coordSysType=
    CARTESIAN, line1=(1.0, 0.0, 0.0), line2=(0.0, 1.0, 0.0), name=
    'Datum csys-1', origin=(0.0, 0.0, 0.0))
```

```
mdb.models['Model-1'].parts['Part-
1'].DatumPlaneByPrincipalPlane(offset=152.4,
    principalPlane=XYPLANE)

    #SIDE TUBE SWEEP SKETCH...DO NOT CHANGE
mdb.models['Model-1'].ConstrainedSketch(gridSpacing=20.4,
name='__sweep__',
    sheetSize=816.0, transform=
    mdb.models['Model-1'].parts['Part-1'].MakeSketchTransform(
    sketchPlane=mdb.models['Model-1'].parts['Part-1'].datums[3],
    sketchPlaneSide=SIDE1,
    sketchUpEdge=mdb.models['Model-1'].parts['Part-1'].datums[2].axis2,
    sketchOrientation=RIGHT, origin=(0.0, 0.0, 152.4)))
mdb.models['Model-1'].parts['Part-
1'].projectReferencesOntoSketch(filter=
    COPLANAR_EDGES, sketch=mdb.models['Model-1'].sketches['__sweep__'])
mdb.models['Model-
1'].sketches['__sweep__'].ConstructionLine(point1=(0.0, 0.0),
    point2=(0.0, -15.3))
mdb.models['Model-
1'].sketches['__sweep__'].VerticalConstraint(addUndoState=
    False, entity=mdb.models['Model-
1'].sketches['__sweep__'].geometry[2])
mdb.models['Model-1'].sketches['__sweep__'].Spot(point=(0.0, 0.0))
mdb.models['Model-
1'].sketches['__sweep__'].CoincidentConstraint(addUndoState=
    False, entity1=mdb.models['Model-
1'].sketches['__sweep__'].vertices[0],
    entity2=mdb.models['Model-1'].sketches['__sweep__'].geometry[2])
mdb.models['Model-1'].sketches['__sweep__'].FixedConstraint(entity=
    mdb.models['Model-1'].sketches['__sweep__'].vertices[0])
mdb.models['Model-
1'].sketches['__sweep__'].ConstructionLine(point1=(0.0, 0.0),
    point2=(-25.5, -35.7))
mdb.models['Model-
1'].sketches['__sweep__'].CoincidentConstraint(addUndoState=
    False, entity1=mdb.models['Model-
1'].sketches['__sweep__'].vertices[0],
    entity2=mdb.models['Model-1'].sketches['__sweep__'].geometry[3])

    #SIDE TUBE ANGLE
mdb.models['Model-1'].sketches['__sweep__'].AngularDimension(line1=
    mdb.models['Model-1'].sketches['__sweep__'].geometry[3], line2=
    mdb.models['Model-1'].sketches['__sweep__'].geometry[2],
textPoint=(
    -11.4507751464844, -45.9118728637695), value=20)

    #DO NOT CHANGE
mdb.models['Model-1'].sketches['__sweep__'].Spot(point=(0.0, -81.6))
mdb.models['Model-
1'].sketches['__sweep__'].CoincidentConstraint(addUndoState=
    False, entity1=mdb.models['Model-
1'].sketches['__sweep__'].vertices[1],
    entity2=mdb.models['Model-1'].sketches['__sweep__'].geometry[2])
mdb.models['Model-
1'].sketches['__sweep__'].ObliqueDimension(textPoint=(
    25.764253616333, -85.9457855224609), value=230.2, vertex1=
```

```
    mdb.models['Model-1'].sketches['__sweep__'].vertices[0], vertex2=
    mdb.models['Model-1'].sketches['__sweep__'].vertices[1])
mdb.models['Model-
1'].sketches['__sweep__'].ConstructionLine(point1=(0.0,
    -230.2), point2=(-122.4, -230.2))
mdb.models['Model-
1'].sketches['__sweep__'].HorizontalConstraint(addUndoState=
    False, entity=mdb.models['Model-
1'].sketches['__sweep__'].geometry[4])
mdb.models['Model-
1'].sketches['__sweep__'].CoincidentConstraint(addUndoState=
    False, entity1=mdb.models['Model-
1'].sketches['__sweep__'].vertices[1],
    entity2=mdb.models['Model-1'].sketches['__sweep__'].geometry[4])
mdb.models['Model-1'].sketches['__sweep__'].Line(point1=(-
35.2687157010159,
    -96.9), point2=(-83.7859479282051, -230.2))
mdb.models['Model-
1'].sketches['__sweep__'].ParallelConstraint(addUndoState=
    False, entity1=mdb.models['Model-
1'].sketches['__sweep__'].geometry[3],
    entity2=mdb.models['Model-1'].sketches['__sweep__'].geometry[5])
mdb.models['Model-
1'].sketches['__sweep__'].CoincidentConstraint(addUndoState=
    False, entity1=mdb.models['Model-
1'].sketches['__sweep__'].vertices[2],
    entity2=mdb.models['Model-1'].sketches['__sweep__'].geometry[3])
mdb.models['Model-
1'].sketches['__sweep__'].CoincidentConstraint(addUndoState=
    False, entity1=mdb.models['Model-
1'].sketches['__sweep__'].vertices[3],
    entity2=mdb.models['Model-1'].sketches['__sweep__'].geometry[3])

    #DO NOT CHANGE
mdb.models['Model-1'].sketches['__sweep__'].undo()
mdb.models['Model-1'].sketches['__sweep__'].Line(point1=(-
83.7859479282051,
    -230.2), point2=(-34.9236609213986, -95.9519697846845))
mdb.models['Model-
1'].sketches['__sweep__'].ParallelConstraint(addUndoState=
    False, entity1=mdb.models['Model-
1'].sketches['__sweep__'].geometry[3],
    entity2=mdb.models['Model-1'].sketches['__sweep__'].geometry[5])
mdb.models['Model-
1'].sketches['__sweep__'].CoincidentConstraint(addUndoState=
    False, entity1=mdb.models['Model-
1'].sketches['__sweep__'].vertices[2],
    entity2=mdb.models['Model-1'].sketches['__sweep__'].geometry[3])

    #SIDE TUBE LENGTH
mdb.models['Model-
1'].sketches['__sweep__'].ObliqueDimension(textPoint=(
    -80.5535049438477, -134.217987060547), value=140.0, vertex1=
    mdb.models['Model-1'].sketches['__sweep__'].vertices[2], vertex2=
    mdb.models['Model-1'].sketches['__sweep__'].vertices[3])

    #DO NOT CHANGE
```

```
mdb.models['Model-1'].ConstrainedSketch(name='__profile__',
sheetSize=816.0,
    transform=(0.0, 0.0, -1.0, 0.939692620785629, -0.342020143326437,
0.0,
    -0.342020143326437, -0.939692620785629, -0.0, -83.7859479282051, -
230.2,
    152.4))
mdb.models['Model-
1'].sketches['__profile__'].ConstructionLine(point1=(-408.0,
    0.0), point2=(408.0, 0.0))
mdb.models['Model-
1'].sketches['__profile__'].ConstructionLine(point1=(0.0,
    -408.0), point2=(0.0, 408.0))
mdb.models['Model-1'].parts['Part-
1'].projectReferencesOntoSketch(filter=
    COPLANAR_EDGES, sketch=mdb.models['Model-
1'].sketches['__profile__'])
mdb.models['Model-
1'].sketches['__profile__'].CircleByCenterPerimeter(center=(
    0.0, 0.0), point1=(0.0, -30.0))
mdb.models['Model-1'].sketches['__profile__'].CoincidentConstraint(
    addUndoState=False, entity1=
    mdb.models['Model-1'].sketches['__profile__'].vertices[1], entity2=
    mdb.models['Model-1'].sketches['__profile__'].geometry[3])
mdb.models['Model-1'].sketches['__profile__'].CoincidentConstraint(
    addUndoState=False, entity1=
    mdb.models['Model-1'].sketches['__profile__'].vertices[0], entity2=
    mdb.models['Model-1'].sketches['__profile__'].geometry[2])

    #SIDE TUBE OUTER DIA
mdb.models['Model-1'].sketches['__profile__'].RadialDimension(curve=
    mdb.models['Model-1'].sketches['__profile__'].geometry[4],
radius=25.4,
    textPoint=(38.5387939453125, -51.92283550419))

    #SIDE SWEEP
mdb.models['Model-1'].parts['Part-1'].SolidSweep(path=
    mdb.models['Model-1'].sketches['__sweep__'], pathOrientation=RIGHT,
    pathPlane=mdb.models['Model-1'].parts['Part-1'].datums[3],
pathUpEdge=
    mdb.models['Model-1'].parts['Part-1'].datums[2].axis2, profile=
    mdb.models['Model-1'].sketches['__profile__'],
sketchOrientation=RIGHT,
    sketchUpEdge=mdb.models['Model-1'].parts['Part-1'].datums[2].axis1)

    #DO NOT CHANGE
mdb.models['Model-1'].sketches.changeKey(fromName='__profile__',
toName=
    '__save__')

#*--CHANGE X AND Y VALUE HERE--* *--X=SIN(THETA)*230.2 ,Y=C0S
(THETHA)*230.2--*
mdb.models['Model-1'].ConstrainedSketch(gridSpacing=3.59,
name='__profile__',
    sheetSize=143.68, transform=
    mdb.models['Model-1'].parts['Part-1'].MakeSketchTransform(
    sketchPlane=mdb.models['Model-1'].parts['Part-1'].faces[1],
```

```
    sketchPlaneSide=SIDE1,
    sketchUpEdge=mdb.models['Model-1'].parts['Part-1'].datums[2].axis1,
    sketchOrientation=LEFT, origin=(-78.733, -216.317, 152.4)))
mdb.models['Model-1'].parts['Part-
1'].projectReferencesOntoSketch(filter=
    COPLANAR_EDGES, sketch=mdb.models['Model-
1'].sketches['__profile__'])
mdb.models['Model-1'].sketches['__profile__'].retrieveSketch(sketch=
    mdb.models['Model-1'].sketches['__save__'])
del mdb.models['Model-1'].sketches['__save__']
mdb.models['Model-1'].sketches['__profile__'].delete(objectList=(
    mdb.models['Model-1'].sketches['__profile__'].geometry[2], ))
mdb.models['Model-1'].sketches['__profile__'].delete(objectList=(
    mdb.models['Model-1'].sketches['__profile__'].geometry[7], ))
mdb.models['Model-
1'].sketches['__profile__'].CircleByCenterPerimeter(center=(
    0.0, 0.0), point1=(0.0, -13.6213825643063))
mdb.models['Model-1'].sketches['__profile__'].CoincidentConstraint(
    addUndoState=False, entity1=
    mdb.models['Model-1'].sketches['__profile__'].vertices[5], entity2=
    mdb.models['Model-1'].sketches['__profile__'].geometry[6])
mdb.models['Model-1'].sketches['__profile__'].CoincidentConstraint(
    addUndoState=False, entity1=
    mdb.models['Model-1'].sketches['__profile__'].vertices[4], entity2=
    mdb.models['Model-1'].sketches['__profile__'].geometry[5])
    #SIDE TUBE INNER DIA
mdb.models['Model-1'].sketches['__profile__'].RadialDimension(curve=
    mdb.models['Model-1'].sketches['__profile__'].geometry[8],
radius=17.78,
    textPoint=(-33.0677856445313, -16.1681496354006))
    #EXTRUDE CUT
mdb.models['Model-1'].parts['Part-
1'].CutExtrude(flipExtrudeDirection=OFF,
    sketch=mdb.models['Model-1'].sketches['__profile__'],
sketchOrientation=
    LEFT, sketchPlane=mdb.models['Model-1'].parts['Part-1'].faces[1],
    sketchPlaneSide=SIDE1, sketchUpEdge=
    mdb.models['Model-1'].parts['Part-1'].datums[2].axis1, upToFace=
    mdb.models['Model-1'].parts['Part-1'].faces[3])

    #DATUM PLANE PARTITION AND REMOVE EXTRA FACES
mdb.models['Model-1'].parts['Part-
1'].DatumPlaneByPrincipalPlane(offset=0.0,
    principalPlane=YZPLANE)
mdb.models['Model-1'].parts['Part-1'].PartitionCellByDatumPlane(cells=
    mdb.models['Model-1'].parts['Part-1'].cells.findAt(((-117.322624,
    10.786931, 200.0), )), datumPlane=
    mdb.models['Model-1'].parts['Part-1'].datums[3])
mdb.models['Model-1'].parts['Part-1'].RemoveFaces(deleteCells=False,
faceList=(
    mdb.models['Model-1'].parts['Part-1'].faces.findAt((-58.493177, -
83.07291,
    153.541372), ), mdb.models['Model-1'].parts['Part-
1'].faces.findAt((
    -67.41703, -133.34951, 153.546149), ),
    mdb.models['Model-1'].parts['Part-1'].faces.findAt((-80.13076, -
146.047435,
```

```
    154.038151), ), mdb.models['Model-1'].parts['Part-
1'].faces.findAt((
    -102.456599, -223.404439, 154.668035), ),
    mdb.models['Model-1'].parts['Part-1'].faces.findAt((-8.565473, -
126.710823,
    154.031316), ), mdb.models['Model-1'].parts['Part-
1'].faces.findAt((
    -117.322624, 10.786931, 200.0), )))
mdb.models['Model-1'].parts['Part-1'].PartitionCellByDatumPlane(cells=
    mdb.models['Model-1'].parts['Part-1'].cells.findAt(((58.004584,
    -102.592468, 0.0), )), datumPlane=
    mdb.models['Model-1'].parts['Part-1'].datums[6])
mdb.models['Model-1'].parts['Part-1'].RemoveFaces(deleteCells=False,
faceList=(
    mdb.models['Model-1'].parts['Part-1'].faces.findAt((10.13103, -
117.303202,
    0.0), ), mdb.models['Model-1'].parts['Part-
1'].faces.findAt((8.832473,
    -101.215352, 101.599996), ),
    mdb.models['Model-1'].parts['Part-1'].faces.findAt((10.13103, -
117.303202,
    152.4), ), mdb.models['Model-1'].parts['Part-
1'].faces.findAt((10.19709,
    -126.589965, 50.799998), )))

    #CREATE INSTANCE AND MAKE INDEPENDENT
mdb.models['Model-1'].rootAssembly.DatumCsysByDefault(CARTESIAN)
mdb.models['Model-1'].rootAssembly.Instance(dependent=ON, name='Part-1-
1',
    part=mdb.models['Model-1'].parts['Part-1'])
mdb.models['Model-1'].rootAssembly.makeIndependent(instances=(
    mdb.models['Model-1'].rootAssembly.instances['Part-1-1'], ))

    #PARTITION BY EDGE
mdb.models['Model-1'].rootAssembly.PartitionCellByExtrudeEdge(cells=
    mdb.models['Model-1'].rootAssembly.instances['Part-1-
1'].cells.getSequenceFromMask(
    ('[#1 ]', ), ), edges=(
    mdb.models['Model-1'].rootAssembly.instances['Part-1-1'].edges[11],
    mdb.models['Model-1'].rootAssembly.instances['Part-1-
1'].edges[12]), line=
    mdb.models['Model-1'].rootAssembly.datums[1].axis3, sense=FORWARD)

    #SET AND SURFACE CREATION
    #MAIN SURFACE
mdb.models['Model-1'].rootAssembly.Surface(name='MAIN_SURFACE',
side1Faces=
    mdb.models['Model-1'].rootAssembly.instances['Part-1-
1'].faces.findAt(((
    -39.933495, -161.593477, 151.254492), ), ((-53.824638, -96.00472,
    151.253843), ), ((-0.75146, -101.597221, 50.799998), ), ))
    #END LOAD SURFACE
mdb.models['Model-1'].rootAssembly.Surface(name='END_LOAD', side1Faces=
    mdb.models['Model-1'].rootAssembly.instances['Part-1-
1'].faces.findAt(((
    -0.751419, -110.058329, 0.0), )))
    #BACK_BC SET
```

```
mdb.models['Model-1'].rootAssembly.Set(faces=
    mdb.models['Model-1'].rootAssembly.instances['Part-1-
1'].faces.findAt(((
    -22.526723, -116.360774, 152.4), ), ((-89.288141, -185.905352,
152.4), ), (
    (-60.52146, -101.90976, 152.4), ), ((-33.281721, -163.238749,
152.4), ), ),
    name='BACK_BC', xEdges=
    mdb.models['Model-1'].rootAssembly.instances['Part-1-
1'].edges.findAt(((
    -90.299433, -196.110272, 152.4), ), ((-36.495379, -152.255332,
152.4), ), (
    (-76.733901, -136.560028, 152.4), ), ((-105.864037, -222.164233,
152.4), ),
    ((-65.288132, -236.932654, 152.4), ), ((-49.611009, -210.569758,
152.4), ),
    ))
    #FRONT_BC SET
mdb.models['Model-1'].rootAssembly.Set(faces=
    mdb.models['Model-1'].rootAssembly.instances['Part-1-
1'].faces.findAt(((
    0.0, -118.533333, 101.599996), ), ((0.0, 110.066666, 101.599996),
), ),
    name='FRONT_BC')
    #SIDE TUBE BOTTOM SET
mdb.models['Model-1'].rootAssembly.Set(faces=
    mdb.models['Model-1'].rootAssembly.instances['Part-1-
1'].faces.findAt(((
    -102.456599, -223.404439, 150.131958), )), name='SIDE_TUBE_BTTM')

    #DATUM PLANES AND PARTITION FOR MESHING
mdb.models['Model-1'].rootAssembly.DatumPlaneByPointNormal(normal=
    mdb.models['Model-1'].rootAssembly.instances['Part-1-1'].edges[6],
point=
    mdb.models['Model-1'].rootAssembly.instances['Part-1-
1'].InterestingPoint(
    mdb.models['Model-1'].rootAssembly.instances['Part-1-1'].edges[6],
MIDDLE))
mdb.models['Model-
1'].rootAssembly.DatumPlaneByPrincipalPlane(offset=35.0,
    principalPlane=XYPLANE)
mdb.models['Model-
1'].rootAssembly.DatumPlaneByPrincipalPlane(offset=75.0,
    principalPlane=XYPLANE)
mdb.models['Model-1'].rootAssembly.DatumPlaneByRotation(angle=125.0,
axis=
    mdb.models['Model-1'].rootAssembly.datums[1].axis3, plane=
    mdb.models['Model-1'].rootAssembly.instances['Part-1-1'].datums[6])
mdb.models['Model-1'].rootAssembly.PartitionCellByDatumPlane(cells=
    mdb.models['Model-1'].rootAssembly.instances['Part-1-
1'].cells.getSequenceFromMask(
    ('[#1 ]', ), ), datumPlane=mdb.models['Model-
1'].rootAssembly.datums[10])
mdb.models['Model-1'].rootAssembly.PartitionCellByDatumPlane(cells=
    mdb.models['Model-1'].rootAssembly.instances['Part-1-
1'].cells.getSequenceFromMask(
```

```
    ('[#4 ]', ), ), datumPlane=mdb.models['Model-
1'].rootAssembly.datums[11])
mdb.models['Model-1'].rootAssembly.PartitionCellByDatumPlane(cells=
    mdb.models['Model-1'].rootAssembly.instances['Part-1-
1'].cells.getSequenceFromMask(
    ('[#1 ]', ), ), datumPlane=mdb.models['Model-
1'].rootAssembly.datums[12])
mdb.models['Model-1'].rootAssembly.PartitionCellByDatumPlane(cells=
    mdb.models['Model-1'].rootAssembly.instances['Part-1-
1'].cells.getSequenceFromMask(
    ('[#1 ]', ), ), datumPlane=mdb.models['Model-
1'].rootAssembly.datums[13])
mdb.models['Model-1'].rootAssembly.seedEdgeBySize(constraint=FINER,
    deviationFactor=0.1, edges=
    mdb.models['Model-1'].rootAssembly.instances['Part-1-
1'].edges.getSequenceFromMask(
    ('[#1f8ff #791f9e ]', ), ), size=2.0)
mdb.models['Model-1'].rootAssembly.seedEdgeBySize(constraint=FINER,
    deviationFactor=0.1, edges=
    mdb.models['Model-1'].rootAssembly.instances['Part-1-
1'].edges.getSequenceFromMask(
    ('[#0 #1186e780 ]', ), ), size=8.0)
mdb.models['Model-1'].rootAssembly.seedEdgeBySize(constraint=FINER,
    deviationFactor=0.1, edges=
    mdb.models['Model-1'].rootAssembly.instances['Part-1-
1'].edges.getSequenceFromMask(
    ('[#1fff8f0f #8000000 ]', ), ), size=6.0)
mdb.models['Model-1'].rootAssembly.seedEdgeBySize(constraint=FINER,
    deviationFactor=0.1, edges=
    mdb.models['Model-1'].rootAssembly.instances['Part-1-
1'].edges.getSequenceFromMask(
    ('[#fc400000 #66000061 ]', ), ), size=11.0)
mdb.models['Model-1'].rootAssembly.generateMesh(regions=(
    mdb.models['Model-1'].rootAssembly.instances['Part-1-1'], ))

    #SECTION CREATION AND SECTION ASSIGNMENT
mdb.models['Model-1'].HomogeneousSolidSection(material='Project Pipe
Steel',
    name='Section-1', thickness=None)
mdb.models['Model-1'].parts['Part-1'].SectionAssignment(offset=0.0,
    offsetField='', offsetType=MIDDLE_SURFACE, region=Region(
    cells=mdb.models['Model-1'].parts['Part-
1'].cells.getSequenceFromMask(
    mask=('[#1 ]', ), )), sectionName='Section-1', thicknessAssignment=
    FROM_SECTION)

    #MATERIAL
mdb.models['Model-1'].Material(name='Project Pipe Steel')
    #ELASTIC PROPERTIES
mdb.models['Model-1'].materials['Project Pipe
Steel'].Elastic(dependencies=0,
    moduli=LONG_TERM, noCompression=OFF, noTension=OFF,
table=((213000.0, 0.29,
    20.0), (208000.0, 0.29, 100.0), (205000.0, 0.29, 200.0), (195000.0,
0.29,
    300.0), (187000.0, 0.29, 400.0), (179000.0, 0.29, 500.0),
(174000.0, 0.29,
```

```
    550.0), (168000.0, 0.29, 600.0)), temperatureDependency=ON,
type=ISOTROPIC)
    #DENSITY
mdb.models['Model-1'].materials['Project Pipe
Steel'].Density(dependencies=0,
    distributionType=UNIFORM, fieldName='', table=((7.75e-09, ), ),
    temperatureDependency=OFF)
    #COEFFICIENT OF THERMAL EXPANSION
mdb.models['Model-1'].materials['Project Pipe
Steel'].Expansion(dependencies=0,
    table=((1.09e-05, 100), (1.13e-05, 200), (1.17e-05, 300), (
    1.2e-05, 400), (1.23e-05, 500), (1.23e-05, 600), (1.23e-05, 700)),
    temperatureDependency=ON, type=ISOTROPIC, userSubroutine=OFF,
zero=0.0)
mdb.models['Model-1'].materials['Project Pipe Steel'].setValues(
    materialIdentifier='')
    #THERMAL CONDUCTIVITY
mdb.models['Model-1'].materials['Project Pipe Steel'].Conductivity(
    dependencies=0, table=((22.3, 20.0), (24.4, 100.0), (26.3, 200.0),
(
    27.4, 300.0), (27.9, 400.0), (27.9, 500.0), (27.8, 550.0), (27.6,
    600.0)), temperatureDependency=ON, type=ISOTROPIC)
    #SPECIFIC HEAT CAPACITY
mdb.models['Model-1'].materials['Project Pipe
Steel'].SpecificHeat(table=((
    435000000.0, 20.0), (447000000.0, 50.0), (458000000.0, 75.0),
(467000000.0, 100.0), (
    477000000.0, 125.0), (487000000.0, 150.0), (495000000.0, 175.0),
(506000000.0, 200.0),
    (515000000.0, 225.0), (528000000.0, 250.0), (541000000.0, 275.0),
(553000000.0, 300.0),
    (566000000.0, 325.0), (581000000.0, 350.0), (597000000.0, 375.0),
(613000000.0, 400.0),
    (629000000.0, 425.0), (647000000.0, 450.0), (667000000.0, 475.0),
(690000000.0, 500.0),
    (714000000.0, 525.0), (740000000.0, 550.0), (770000000.0, 575.0),
(806000000.0, 600.0),
    (849000000.0, 625.0), (901000000.0, 650.0), (970000000.0, 675.0),
(1060000000.0,
    700.0), (1160000000.0, 725.0), (971000000.0, 750.0)),
temperatureDependency=ON)
mdb.models['Model-1'].materials['Project Pipe
Steel'].setValues(description='')

    #LOAD AMPLITUDES
    #FILM COEFFICIENT
mdb.models['Model-1'].TabularAmplitude(data=((600.0, 0.5), (1800.0,
0.5),
    (2400.0, 1), (5400.0, 1), (5700.0, 0.5), (25020.0, 0.5), (
    30000.0, 0)), name=
    'Film Coefficient', smooth=SOLVER_DEFAULT, timeSpan=TOTAL)
    #INTERNAL PRESSURE
mdb.models['Model-1'].TabularAmplitude(data=((600.0, 7.5), (1800.0,
7.5), (
    2400.0, 14.0), (5400.0, 14.0), (5700.0, 7.5), (25020.0, 0.0),
(30000.0,
    0.0)), name='Internal Pressure Load', smooth=SOLVER_DEFAULT,
```

```
    timeSpan=TOTAL)
    #STEAM TEMPERATURE
mdb.models['Model-1'].TabularAmplitude(data=((0.0, 20.0), (600.0,
400.0), (
    1800.0, 500.0), (2400.0, 600.0), (5400.0, 600.0), (5700.0, 500.0),
(
    25020.0, 20.0), (30000.0, 20.0)), name=
    'Temperature', smooth=SOLVER_DEFAULT, timeSpan=TOTAL)

    #NODE SET CREATION FOR CONSTRAINT BY EQUATION
mdb.models['Model-1'].rootAssembly.Set(name='Constraint Set', nodes=
    mdb.models['Model-1'].rootAssembly.instances['Part-1-
1'].nodes.getSequenceFromMask(
    mask=('[#f4000000 #0:26 #ffffffe0 #ffffffff:3 #7ff #0:186
#ffff0000',
    ' #ffffffff:5 #7ffff #0:1583 #38380f00 #318c3838 #e18c61c
#31870c63',
    ' #c318c386 #30e18c61 #631870c6 #1c318c38 #630e18c6 #8631870c
#61c318c3',
    ' #c630e18c #38631870 #c61c318c #c630e18 #c3863187 #8c61c318
#70c630e1',
    ' #8c386318 #18c61c31 #870c630e #18c38631 #e18c61c3 #1870c630
#318c3863',
    ' #e18c61c #31870c63 #c318c386 #30e18c61 #631870c6 #1c318c38
#630e18c6',
    ' #8631870c #61c318c3 #c630e18c #38631870 #c61c318c #c630e18
#c3863187',
    ' #8c61c318 #70c630e1 #8c386318 #18c61c31 #870c630e #18c38631
#e18c61c3',
    ' #1870c630 #318c3863 ]', ), ))
mdb.models['Model-1'].rootAssembly.Set(name='reference node', nodes=
    mdb.models['Model-1'].rootAssembly.instances['Part-1-
1'].nodes.getSequenceFromMask(
    mask=('[#8000000 ]', ), ))

    #CREATE INTERNAL PRESSURE LOAD STEP--*
mdb.models['Model-1'].CoupledTempDisplacementStep(deltmx=10.0,
initialInc=1.0,
    matrixStorage=SOLVER_DEFAULT, maxInc=1000.0, maxNumInc=2000,
minInc=1e-05,
    name='INTERNAL_PRESSURE_LOAD', previous='Initial',
solutionTechnique=
    SEPARATED, timePeriod=30000.0)

    #INTERACTION PROPERTIES --MASS FLUX--*
mdb.models['Model-1'].FluidExchangeProperty(dataTable=((21.0, ), ),
definition=
    MASS_FLUX, name='IntProp-1')

    #CONSTRAINT BY EQUATION
mdb.models['Model-1'].Equation(name='Constraint-1', terms=((1.0,
    'Constraint Set', 3), (-1.0, 'reference node', 3)))

    #PREDEFINED FIELD SET CREATION
mdb.models['Model-1'].rootAssembly.Set(cells=
    mdb.models['Model-1'].rootAssembly.instances['Part-1-
1'].cells.findAt(((
```

```
    0.0, -110.066666, 100.799998), ), ((0.0, 118.533333, 100.799998),
), ((0.0,
    110.066666, 61.666667), ), ((-93.859907, -184.241369, 149.103704),
), ((
    -66.487005, -130.780742, 151.327965), ), ((-0.751419, -110.058329,
0.0), ),
    ), name='Predefined Field')

    #PREDEFINED FIELDS
mdb.models['Model-1'].Temperature(createStepName='Initial',
    crossSectionDistribution=CONSTANT_THROUGH_THICKNESS,
distributionType=
    UNIFORM, magnitudes=(20.0, ), name='Predefined Field-1', region=
    mdb.models['Model-1'].rootAssembly.sets['Predefined Field'])

    #LOADS
    #1.END LOAD (END LOAD=INTERNAL RADIUS/(2*HEADER THICKNESS)
mdb.models['Model-1'].Pressure(amplitude='Internal Pressure Load',
    createStepName='INTERNAL_PRESSURE_LOAD', distributionType=UNIFORM,
field=''
    , magnitude=-1.778, name='END LOAD', region=
    mdb.models['Model-1'].rootAssembly.surfaces['END_LOAD'])

    #2.INTERNAL PRESSURE LOAD
mdb.models['Model-1'].Pressure(amplitude='Internal Pressure Load',
    createStepName='INTERNAL_PRESSURE_LOAD', distributionType=UNIFORM,
field=''
    , magnitude=1.0, name='INTERNAL PRESSURE', region=
    mdb.models['Model-1'].rootAssembly.surfaces['MAIN_SURFACE'])

    #SURFACE FILM CONDITION--*
mdb.models['Model-
1'].FilmCondition(createStepName='INTERNAL_PRESSURE_LOAD',
    definition=EMBEDDED_COEFF, filmCoeff=1.0, filmCoeffAmplitude=
    'Film Coefficient', name='SURFACE_FILM_CONDITION', sinkAmplitude=
    'Temperature', sinkDistributionType=UNIFORM, sinkFieldName='',
    sinkTemperature=1.0, surface=
mdb.models['Model-1'].rootAssembly.surfaces['MAIN_SURFACE'])

    #CREATE LOCAL DATUM CSYS
mdb.models['Model-1'].rootAssembly.DatumCsysByTwoLines(CARTESIAN,
line1=
    mdb.models['Model-1'].rootAssembly.instances['Part-1-1'].edges[46],
line2=
    mdb.models['Model-1'].rootAssembly.instances['Part-1-1'].edges[45],
name=
    'Datum csys-2')

    #DISPLACEMENT BOUNDARY CONDITIONS--*
    #BACK BC
mdb.models['Model-1'].DisplacementBC(amplitude=UNSET,
createStepName='Initial',
    distributionType=UNIFORM, fieldName='', localCsys=None,
name='BACK',
    region=mdb.models['Model-1'].rootAssembly.sets['BACK_BC'],
u1=UNSET, u2=UNSET
    , u3=SET, ur1=UNSET, ur2=UNSET, ur3=UNSET)
```

```
    #FRONT BC
mdb.models['Model-1'].DisplacementBC(amplitude=UNSET,
createStepName='Initial',
    distributionType=UNIFORM, fieldName='', localCsys=None,
name='FRONT',
    region=mdb.models['Model-1'].rootAssembly.sets['FRONT_BC'], u1=SET,
u2=UNSET,
    u3=UNSET, ur1=UNSET, ur2=UNSET, ur3=UNSET)
    #SIDE TUBE BOTTOM BC
mdb.models['Model-1'].DisplacementBC(amplitude=UNSET,
createStepName='Initial',
    distributionType=UNIFORM, fieldName='',
localCsys=mdb.models['Model-1'].rootAssembly.datums[25], name=
    'SIDE TUBE BOTTOM', region=mdb.models['Model-
1'].rootAssembly.sets['SIDE_TUBE_BTTM']
    , u1=UNSET, u2=SET, u3=UNSET, ur1=UNSET, ur2=UNSET, ur3=UNSET)

    #ELEMENT SET CREATION FOR RESULT EXTRACTION
mdb.models['Model-1'].rootAssembly.Set(elements=
    mdb.models['Model-1'].rootAssembly.instances['Part-1-
1'].elements.getSequenceFromMask(
    mask=('[#0:60 #80 #cc000000 #88ccc #eeeee000 #8cccccc #eeeffffff',
    ' #fffceeee #ffffffff #fffffee #ffffffff:5 #ffffff #0:31
#10000000',
    ' #33333111 #7f777773 #ffffffff:23 #ffff #0:34 #ffff0000
#ffffffff:153',
    ' #cf #0:3 #ff000000 #ffffffff:3 #ceff #0:4 #ffffffff:3',
    ' #8effff #0:4 #ffffff00 #ffffffff:156 #f ]', ), ), name='Result
Element')



    #HISTORY OUTPUT REQUEST/INCREMENT VALUE
mdb.models['Model-1'].historyOutputRequests['H-Output-
1'].setValues(frequency=
    20)

mdb.models['Model-1'].rootAssembly.setElementType(elemTypes=(ElemType(
    elemCode=C3D20RT, elemLibrary=STANDARD),
ElemType(elemCode=UNKNOWN_WEDGE,
    elemLibrary=STANDARD), ElemType(elemCode=C3D10MT,
elemLibrary=STANDARD)),
    regions=(
    mdb.models['Model-1'].rootAssembly.instances['Part-1-
1'].cells.findAt(((
    0.0, -110.066666, 100.799998), ), ((0.0, 118.533333, 100.799998),
), ((0.0,
    110.066666, 61.666667), ), ((-93.859907, -184.241369, 149.103704),
), ((
    -66.487005, -130.780742, 151.327965), ), ((-0.751419, -110.058329,
0.0), ),
    ), ))

mdb.models['Model-1'].rootAssembly.regenerate()

    #JOB CREATION
mdb.Job(atTime=None, contactPrint=OFF, description='', echoPrint=OFF,
```

```
    explicitPrecision=SINGLE, getMemoryFromAnalysis=True,
historyPrint=OFF,
    memory=90, memoryUnits=PERCENTAGE, model='Model-1', modelPrint=OFF,
    multiprocessingMode=DEFAULT, name='HEADER_10_8_1',
nodalOutputPrecision=SINGLE,
    numCpus=1, numDomains=16, numGPUs=1, queue=None, scratch=
    '', type=ANALYSIS, userSubroutine='', waitHours=0, waitMinutes=0)

    #SUBMIT
#mdb.jobs['HEADER_10_8_1'].submit(consistencyChecking=OFF)
```